

# Oil & Natural Gas Technology

DOE Award No.: DE-FC26-06NT42961

## Final Report

**Part 1: Phase I (CATTs Theory), Phase II (Milne Point)  
Part 2: Phase III (Hydrate Ridge)**

Submitted by:  
Rock Solid Images  
2600 S. Gessner, Suite 650  
Houston, TX 77063

Prepared for:  
United States Department of Energy  
National Energy Technology Laboratory

June 30, 2010



Office of Fossil Energy



## **DISCLAIMER**

This report was prepared as an account of work sponsored by an agency of the United States Government. Neither the United States Government nor any agency thereof, nor any of their employees, makes any warranty, express or implied, or assumes any legal liability or responsibility for the accuracy, completeness, or usefulness of any information, apparatus, product, or process disclosed, or represents that its use would not infringe privately owned rights. Reference herein to any specific commercial product, process, or service by trade name, trademark, manufacturer, or otherwise does not necessarily constitute or imply its endorsement, recommendation, or favoring by the United States Government or any agency thereof. The views and opinions of authors expressed herein do not necessarily state or reflect those of the United States Government or any agency thereof.

# Table of Contents – Part 1

<b>1. Executive Summary .....</b>	<b>3</b>
<b>2. CATTs Theory .....</b>	<b>5</b>
B. Introduction.....	5
C. Solutions To The Challenge Of Scale In Mapping Of Hydrate .....	5
i. Effect of Scale in Synthetic Earth.....	7
ii. Accumulated Hydrate Volume .....	9
iii. Cumulative Seismic Attribute .....	10
iv. Amplitude-Based CATT .....	12
D. Discussion.....	14
E. Conclusion .....	17
<b>3. Cumulative Attributes (CATTs) on Milne Point Seismic Data. ....</b>	<b>17</b>
A. Gas Hydrate Volume at Well A .....	21
B. Post-Stack Inversion Of Milne Point Seismic Data.....	22
<b>4. Geological Controls On Methane Gas Hydrate Occurrence.....</b>	<b>27</b>
A. Introduction.....	27
B. Geological Models.....	28
C. Tectonics.....	29
D. Paleoenvironment.....	30
E. Resource Estimates .....	36

## 1. Executive Summary

This study introduces a new type of “cumulative seismic attribute” (CATT) which quantifies gas hydrates resources in Hydrate Ridge offshore Oregon. CATT is based on case-specific transforms that portray hydrated reservoir properties.

The soft-sand model links reservoir properties such as porosity, fluid compressibility, mineralogy, and effective pressure for unconsolidated sediments. In the model, gas hydrates are incorporated as part of the matrix, reducing porosity and increasing P- and S-wave velocities. Thus, in this study we used a theoretical rock physics model to correct measured velocity log data.

Rock physics analysis suggested that P-wave impedance may provide a good discrimination between gas hydrate bearing intervals at Hydrate Ridge. This is because the hydrate zone has higher velocity and lower density than surrounding sediments, and as a result the acoustic impedance of hydrate-bearing sediments is generally higher than surrounding water-bearing sediments. However, our analysis also shows that the ability to discriminate only exists if the gas hydrate saturation is higher than about 20%. Sediments containing gas hydrate accumulations less than 20% can sometimes be mapped but the discrimination is non-unique and may give false positives. With this proviso, we proceeded to map gas hydrate accumulations using a P-wave impedance volume derived from impedance inversion of seismic data.

An inverted acoustic impedance volume is created by applying a transform to seismic data and then combining it with well data. In this process the well data provides the low frequency component of the inversion and the seismic data provides the high frequency component. A significant shortcoming of this project was the absence of seismic velocities to help guide the extrapolation of well log impedances throughout the project area. The result is a lowered confidence in the estimation of hydrate concentrations away from well control.

Seismic data quality was acceptable for performing an inversion; however, data conditioning was nonetheless performed in order to achieve the highest possible data fidelity. The two data conditioning processes we applied were spectral balancing and edge-preserving signal-to-noise (S/N) enhancement.

After data conditioning was completed, a seismic wavelet was estimated through seismic well tie, a low frequency background model was generated from well data using horizon control, and

the seismic data was inverted. The final product of the inversion, a P-wave impedance volume, was the input for calculating CATTs.

CATTs were obtained by integrating the inverse squared seismic impedance with respect to depth. The integration is performed only where this impedance has a positive anomaly relative to the background. Two seismic cumulative attributes (CATTs), saturation and cumulative volume, were computed. Saturation is a cumulative property that relates the fraction of hydrate concentration to acoustic impedance. Cumulative volume is a correlation between impedance and hydrate percentages across a hydrate-bearing interval.

The method shows measurable responses within all gas hydrate intervals exceeding saturations of 20% but fails to detect lower concentration hydrate accumulations that lack a seismic signature. However, overall this method shows promise for quantifying significant accumulations of gas hydrate.

Analysis of the resulting hydrate saturation and cumulative hydrate volumes show that in a gross sense gas hydrate formation depends on structural elevation, because for the entire survey area, regions above a closing contour of 1700 ms show that gas hydrates are limited to a narrow window, 30 to 50 ms wide (~26 to 43 m) immediately above the bottom simulating reflector (BSR), with the highest hydrate levels reached on the crest of the dome. Seismic and well log data support the hypothesis that gas hydrate formation in these unconsolidated sediments reduces permeability, ultimately causing self-sealing of the gas hydrate stability zone (GHSZ), as evidenced by “free” gas trapped against the BSR from below and reduced gas hydrate formation upward in the GHSZ. Gas hydrate formation in the GHSZ is generally independent of lithology, although higher compressional velocities in low  $V_{CLAY}$  layers suggest that siltier layers become preferentially hydrated. For individual sands located above the closing contour, higher-than-background hydrate saturations may occur low on structure, in close proximity to normal faults. Because this method (1) is potentially affected by false positives from high impedances generated by high acoustic contrasts from causes other than gas hydrates (for instance, heavy minerals), (2) does not reliably detect hydrate saturations below 20%, and (3) because well kriging alone cannot possibly provide a stable low-frequency model, the resource estimates of 720 Bcf for a 45 km<sup>2</sup> wide area obtained in this study should be viewed with caution.

## **2. CATTs Theory**

### ***B. Introduction***

Gas hydrate reservoir characterization is, in principle, no different from the traditional hydrocarbon reservoir characterization. Similar and well-developed remote sensing techniques can be used, seismic reflection profiling being the dominant among them.

Seismic response of the subsurface is determined by the spatial distribution of the elastic properties. By mapping the elastic contrast, the geophysicist can illuminate tectonic features and geobodies, hydrocarbon reservoirs included. To accurately translate elastic-property images into images of lithology, porosity, and the pore-filling phase, quantitative knowledge is needed that relates rock's elastic properties to its bulk properties and conditions. Specifically, to quantitatively characterize a natural gas hydrate reservoir, we must be able to relate the elastic properties of the sediment to the volume of gas hydrate present and the host-rock properties and conditions, such as mineralogy, porosity, pressure, and temperature. One way of achieving this goal is through rock physics effective-medium modeling and utilizing this modeling to account for the effects of scale and geometry, reservoir properties and conditions, and the properties and conditions of the background for quantitative seismic interpretation.

### ***C. Solutions To The Challenge Of Scale In Mapping Of Hydrate***

Rock physics transforms are based on data generated in the laboratory at the scale of inches or in the well at the scale of feet. We aspire to use them at the seismic scale in tens or hundreds of feet. The vast disparity between these scales may lead to erroneous results during direct application of rock physics to seismic data. Indeed, small hydrate saturation in a relatively thick reservoir may produce exactly the same seismic reflection in the near and far offset as large hydrate saturation in a thinner sand layer (see the synthetic example illustrated in Figure 3), One of such transforms discussed and utilized in the previous sections connects the gas hydrate saturation in sediment to the elastic-wave velocity (Dvorkin et al., 2003). It is based on the Dvorkin and Nur (1996) effective-medium model, which relates the elastic moduli of soft unconsolidated clastic sediment to the porosity, pore fluid compressibility, mineralogy, and

effective pressure. The model assumes that at the critical porosity of 40%, the effective elastic moduli of the dry mineral framework come from the Hertz-Mindlin contact theory for elastic spheres. This end point is connected with the zero-porosity, solid mineral, end point by the modified lower Hashin-Shtrikman bound appropriate for unconsolidated rock. Once the dry-frame elastic moduli are known, those of the saturated sediment are calculated using Gassmann's fluid substitution equation.

This model accounts for the presence of gas hydrate in sediment by treating the hydrate as part of the load-bearing frame. It assumes that the hydrate acts to reduce the porosity and, at the same time, alters the elastic properties of the composite solid matrix phase. The net effect is an increase in the P- and S-wave velocity and impedance and small reduction in Poisson's ratio in water-saturated rock where part of the pore space is filled with gas hydrate (Figure 1).

This model accurately matches methane hydrate well data offshore (the Outer Blake Ridge and Nankai Trough) as well as onshore (a Mallik well, Figure 2). It constitutes a fairly universal *log-scale* rock physics transform between methane hydrate saturation, porosity and mineralogy of the host sediment frame, and P- and S-wave velocity and impedance. Can it be directly applied to the *seismic-scale* velocity and impedance to estimate in-situ hydrate saturation?

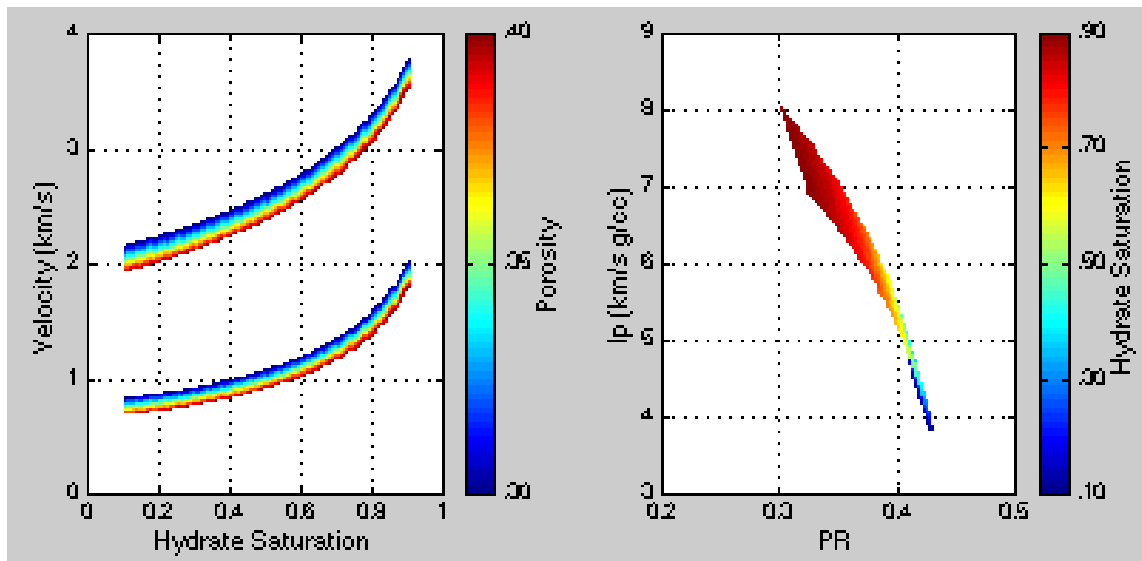


**Figure 1. Rock physics model for sediment with methane hydrate. P- and S-wave velocity versus hydrate saturation color-coded by the sediment's porosity (left, in decimal %) and P-wave impedance versus Poisson's ratio color-coded by hydrate saturation (right, in decimal %). This modeling is for clean sand with porosity between 0.3 and 0.4.**

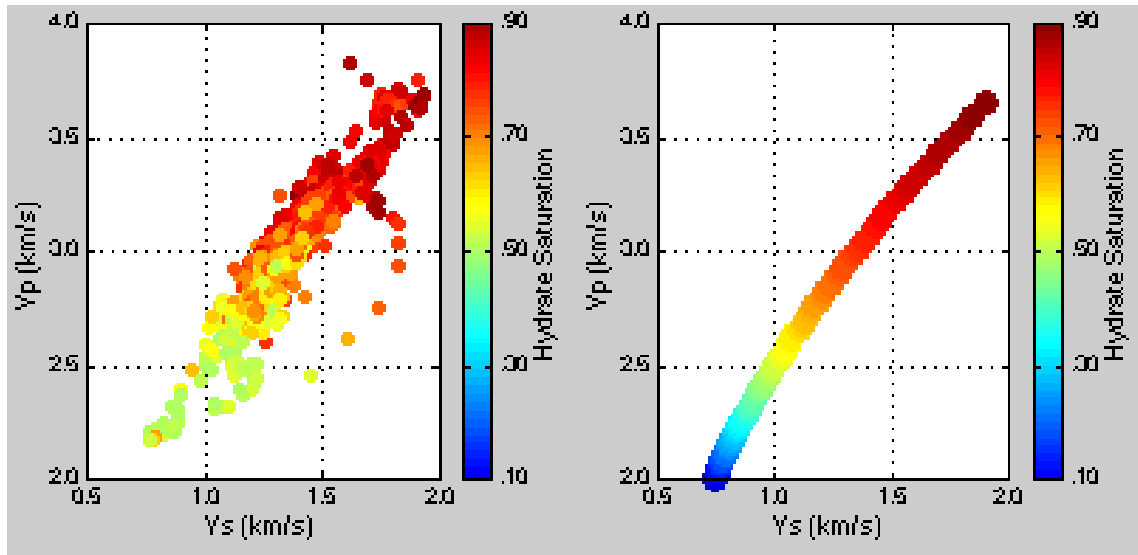


**Figure 2.** *P- versus S-wave velocity in the Mallik well, color-coded by hydrate saturation (left, in decimal %), and corresponding modeling results (right). The model accurately mimics the data.*

### i. Effect of Scale in Synthetic Earth.

To address this question, consider a one-dimensional earth model with three sand layers of progressively increasing thickness containing methane hydrate (Figure 3). The porosity, clay content, and hydrate saturation in the sand are constant, 0.4, 0.05, and 0.7, respectively. The shale background also has constant porosity 0.35 and clay content 0.5, and is fully water saturated. The *log-scale* impedance in the section is calculated from porosity, mineralogy, and hydrate saturation according to the above-described model. (Note: Throughout this document porosity and saturation units are in decimal percent, as is standard in the industry. There is no nomenclature that signifies this, such as % which is used for whole-number percent, so they are left without unit designation when used).

A simple way of calculating the *seismic-scale* impedance is via the Backus upscaling which uses a running harmonic average of the elastic modulus. This upscaled (seismic) impedance profile is shown in Figure 3 in red. The seismic impedance is the same as the log-scale impedance in the thick hydrate-sand layer located at the bottom while it is noticeably different in the thinner layers located above.

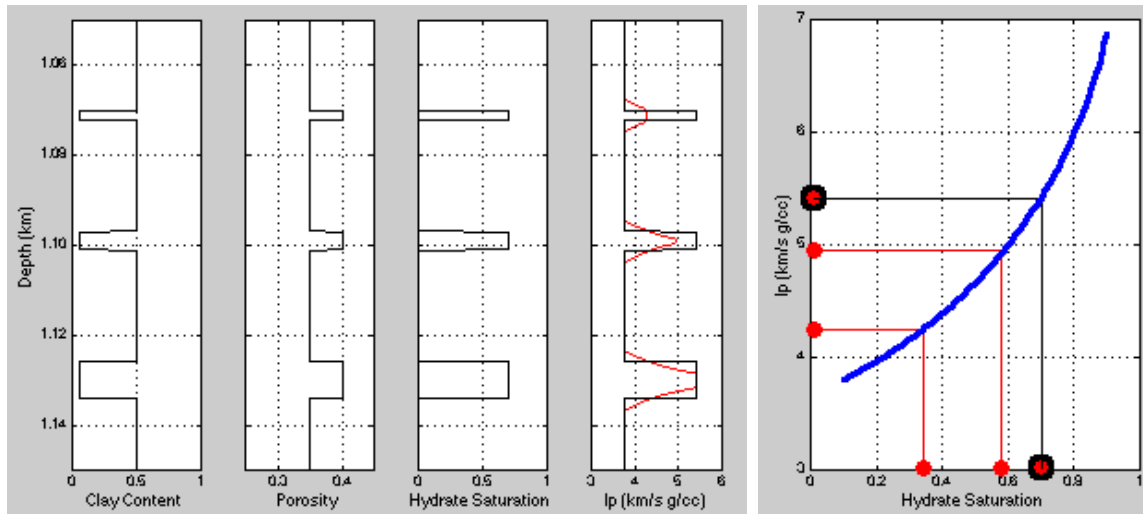


**Figure 3. Earth model with three methane hydrate layers. From left to right: clay content; porosity; hydrate saturation; and acoustic impedance. Clay content, saturation, and porosity are in units of decimal percent. The red curve is the Backus average of the log-scale impedance using a running 5-meter window. The plot on the right shows a model impedance versus hydrate saturation curve (blue) and the seismic-scale impedance and inferred hydrate saturation (red symbols). The black symbols represent the log-scale impedance.**

If this seismic impedance is used with the log-scale impedance-hydrate saturation transform, the predicted hydrate saturation in the sand will be about 0.6 instead of 0.7 in the second layer and about 0.35 instead of 0.7 in the upper layer (Figure 3, right-hand frame). This example illustrates the dichotomy due to scale in geophysical interpretation: a log-scale relation should not be unconditionally applied to seismic-scale data and the hydrate saturation at a point cannot be always correctly mapped from seismic impedance. The reason is that an elastic property at a point cannot be accurately recovered from an experiment that employs large wavelengths. *Downscaling* of seismic-scale measurements is essentially impossible without additional assumptions about the structure of the subsurface. Such assumptions could be quite groundless without direct well control.

Therefore, let us pose the problem of hydrate reservoir characterization differently by seeking a *scale-independent volumetric reservoir property* and a *scale-independent seismic attribute* to quantify this property.

## ii. Accumulated Hydrate Volume

One such reservoir property is the cumulative volume of hydrate ( $V_{MH}$ ) which is the integral of hydrate saturation ( $S_{MH}$ ) with respect to depth  $z$ :

$$V_{MH} = \int \phi(z)S_{MH}(z)dz = \int C_{MH}(z)dz, \quad (1)$$

where  $\phi$  is the porosity of the host sediment in decimal percent and  $C_{MH} = \phi S_{MH}$  is hydrate concentration in decimal percent.  $V_{MH}$  is measured in hydrate volume per horizontal area ( $\text{m}^3/\text{m}^2$ ).

By introducing this property, we depart from the traditional goal of inferring hydrate concentration at a point in space. Instead we aim at determining the total hydrate reserve in a reservoir.

By following the Backus-average formulation for finely-layered media, we can also find a scale-independent elastic property. It is the integral of the anomaly of the inverse compressional modulus, where the anomaly is the difference between the values in the background ( $M_B^{-1}$ ) and hydrate reservoir ( $M^{-1}$ ):

$$C_M = \int [M_B^{-1}(z) - M^{-1}(z)]dz. \quad (2)$$

This cumulative property calculated at different scales for the earth model shown in Figure 3 is plotted versus depth in Figure 4. It is scale-independent indeed and can be related to  $V_{MH}$  by a universal scale-independent transform as shown in the  $V_{MH}$  versus  $C_M$  cross-plot in Figure 4.

An elastic property commonly used in seismic reservoir characterization is the acoustic impedance  $I_p$ . It is related to the compressional modulus  $M$  as  $I_p^2 = \rho_b M$ , where  $\rho_b$  is the bulk density. The density of methane hydrate is close to that of water and the total porosity of shale and sand are close to each other in the shallow subsurface where hydrates occur. As a result,  $\rho_b$  is almost constant and  $I_p^2$  is *approximately* scale-independent because averaging  $I_p^{-2}$  is analogous to harmonically averaging the compressional modulus.

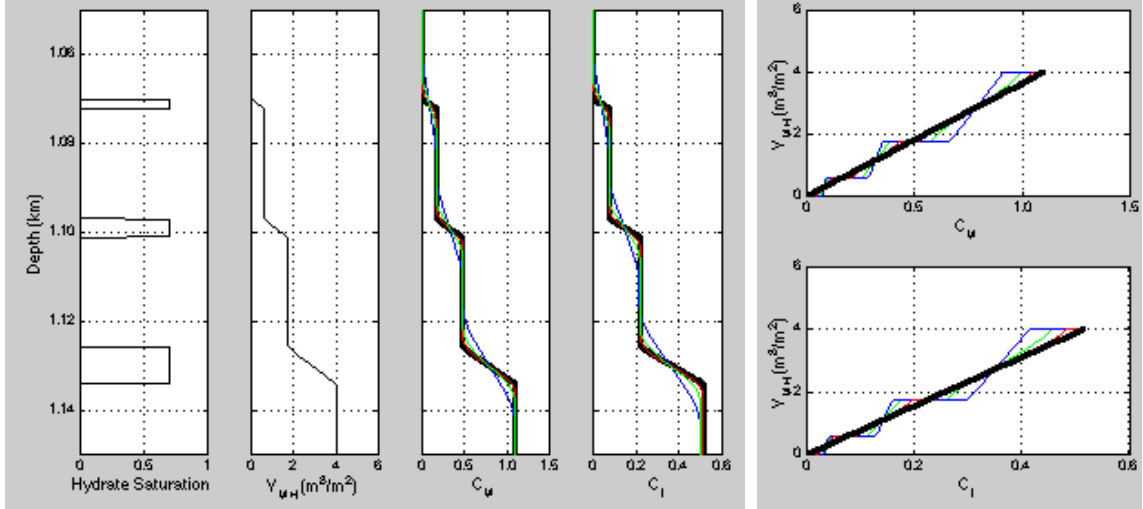


**Figure 4. Earth model with three methane hydrate layers. From left to right: hydrate saturation in decimal %; accumulated hydrate volume ( $V_{MH}$ ) in  $m^3/m^2$ ; the integral of the anomaly of the inverse compressional modulus ( $C_u$ , scale-independent); and the integral of the anomaly of the inverse squared acoustic impedance ( $C_I$ , scale-independent). The black curves are for the log-scale elastic properties and the colored curves are for upscaled elastic properties using a 5-meter (red), 10-meter (green), and 20-meter (blue) running window. The plots on the right relate the accumulated hydrate volume to the two scale-independent elastic properties derived from the modulus (top) and impedance (bottom).**

Therefore, the integral of the anomaly of the inverse squared acoustic impedance

$$C_I = \int [I_{pB}^{-2}(z) - I_p^{-2}(z)] dz, \quad (3)$$

where  $I_{pB}$  is the background impedance in km/s g/cc, can be considered as a scale-independent seismic attribute to be universally related to the cumulative volume of hydrate. The  $C_I$  versus depth plot in Figure 4 as well as the  $V_{MH}$  versus  $C_I$  cross-plot confirm this supposition.

### iii. Cumulative Seismic Attribute

$C_I$  is a cumulative attribute (or CATT) that appears almost scale-independent. It belongs to a new class of seismic attributes: while the seismic impedance (acoustic and elastic alike) can be, simply speaking, estimated by integrating the trace, a CATT is estimated by integrating the trace *repeatedly*. CATTs potentially can be used in various geological environments to map cumulative (rather than point) rock properties from seismic. These attributes have to be designed based on concrete rock physics transforms relevant to the problem under

examination. For example, in a low impedance contrast environment CATTs may have to be based on offset-driven elastic impedance.

For a hydrate reservoir in the above synthetic example, the relation between  $I_p^{-2}$  and hydrate concentration is approximately linear (Figure 5):

$$C_{MH} = 0.51 - 6.74I_p^{-2}, \quad (8)$$

where the impedance is in km/s g/cc. By integrating this equation within methane hydrate layers, we can obtain a scale-independent estimate for the accumulated hydrate volume from the acoustic impedance.

Perhaps the main caveat of this method is that the above linear equation is valid for specific hydrate reservoir properties (porosity 0.4 and clay content 0.05). Fortunately, this transform only weakly depends on the clay content in the host sand: the bold yellow line in Figure 5 is plotted for porosity 0.4 and clay content between zero and 0.2 and is practically the same as the red line drawn for this porosity and 0.05 clay content.

In contrast, the porosity of the host sand strongly affects the impedance. The cyan curve in Figure 5 is plotted for porosity 0.35 and clay content between zero and 0.2. Its linear fit is  $C_{MH} = 0.45 - 7.13I_p^{-2}$ . For  $I_p^{-2} = 0.04$  this transform gives  $C_{MH} = 0.17$  while the original transform (for porosity 0.4) gives  $C_{MH} = 0.24$ . The error of this estimate is about 30%. Fortunately, the slopes of the two transforms are very close to each other, and so the estimate will be correct at least in a relative sense.

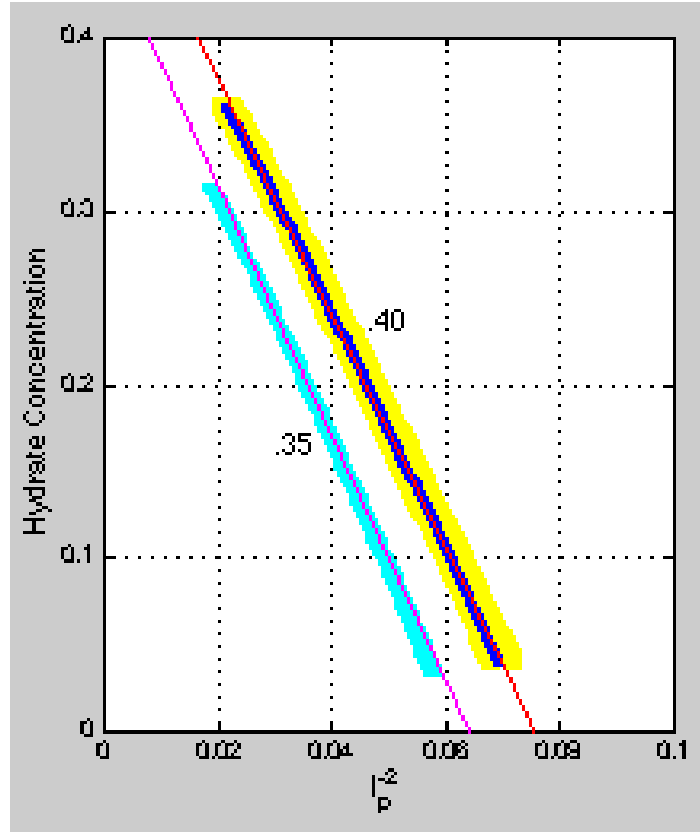


**Figure 5.** Hydrate concentration versus inverse squared impedance for sand with porosity 0.40 and 0.35 (as marked in the plot) in decimal %. The bold yellow and cyan lines are for clay content between zero and 0.2 in decimal %. The blue line on the yellow background is for clay content 0.05. The thin lines are the linear fits.

#### iv. Amplitude-Based CATT

We generate a normal-incidence trace by convolving a 60 Hz Ricker wavelet with the reflectivity series in the above synthetic earth model. The acoustic impedance is calculated from this amplitude as the exponent of twice its integral with respect to TWT. Then we calibrate this relative impedance to the physical P-wave impedance by matching it with that in the thick hydrate layer at the bottom of the interval (Figure 6). As expected, the seismic impedance is much smaller than the log-scale impedance in the upper two thin hydrate layers.

Next we calculate a seismic CATT by integrating the anomaly of the inverse squared seismic impedance with respect to depth according to Equation (7). The integration is carried only where this impedance has a positive anomaly relative to the background. Time is converted to

depth using the velocity in the earth model. This seismic  $I_p^{-2}$  is converted to hydrate concentration  $C_{MH}$  using Equation (8). This estimate of hydrate concentration strongly underestimates the actual values in the thin hydrate layers. However, the integral of  $C_{MH}$  with respect to depth is close to the actual accumulated hydrate volume  $V_{MH}$  (Figure 6). The utility of the proposed CATT for estimating the accumulated hydrate volume is further confirmed by Figure 7 where the latter is plotted versus the former and compared to these transforms from the log-scale and Backus-averaged impedance.

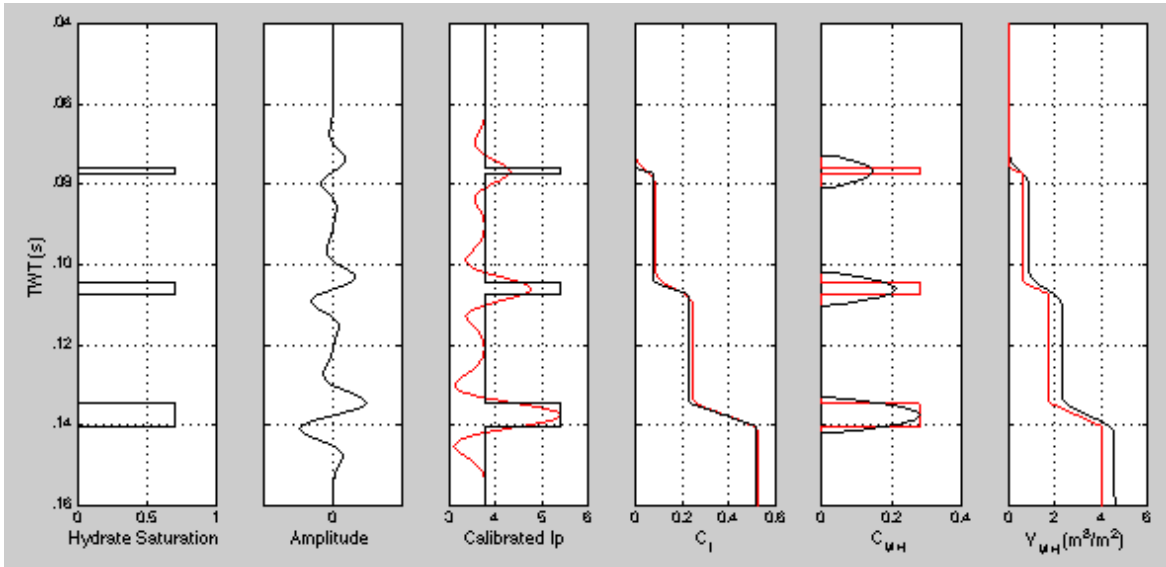


**Figure 6. Synthetic earth model. From left to right: hydrate saturation in decimal %; normal-incidence trace; log-scale impedance (black) and calibrated seismic impedance (red) in km/s g/cc; CATT from log-scale impedance (black) and from calibrated seismic impedance (red); the actual hydrate concentration (black) and that from the seismic CATT (red); and the actual accumulated hydrate volume (black) and that from the seismic CATT (red) in  $m^3/m^2$ .**

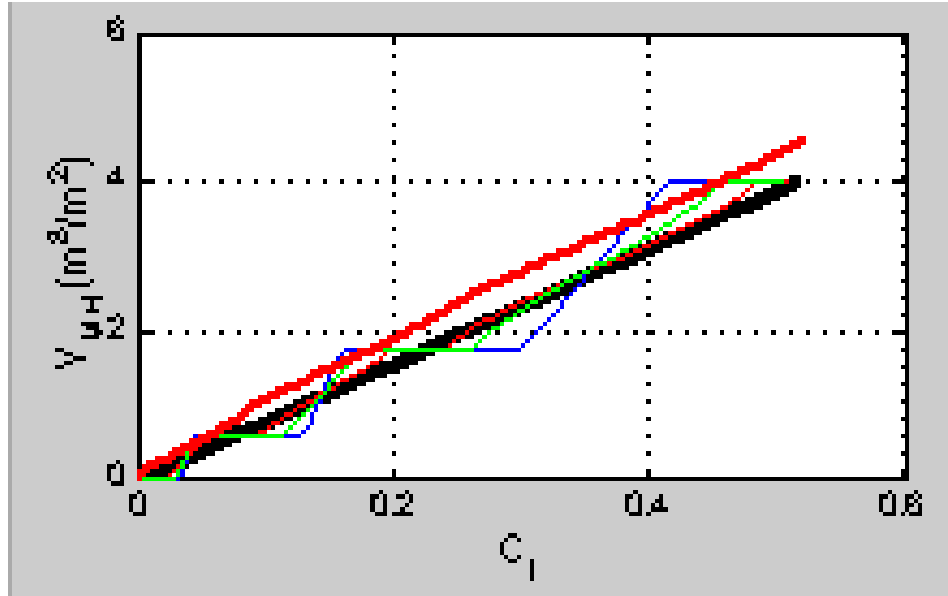


**Figure 7.** Same as the cross-plot in the right-bottom frame in Figure 4 with synthetic-seismic CATT curve (bold red) added.

### ***D. Discussion***

The assumption about the validity of a rock physics relation across a large span of the spatial scale is implicitly present in direct applications of rock physics to seismic data. This assumption may be violated where the “true” small-scale elastic properties are not resolved. Our approach is to admit that we cannot quantify reservoir property at a subresolution scale. Instead, we propose to quantify the volume integral of this property (or the cumulative property) and introduce a new class of seismic attributes, the cumulative attributes, that can be related by means of rock physics to the cumulative reservoir property, which in this specific example is the accumulated volume of methane hydrate.

We show that CATTs can be used with synthetic seismic amplitude to quantify a hydrate reservoir. This means that this class of attributes can also succeed with real seismic data, specifically with accurate seismic impedance volumes.

It is important to stress that the rock physics transforms between a CATT and hydrate volume used in this example are site- and case-specific (designed for the Mallik gas hydrate reservoir). Although this rock physics model is fairly universal, it may have to be adjusted and calibrated to be used at another location. Relevant and correct rock physics treatment is a key in designing a

CATT optimally suitable for reservoir characterization whether the deposit is unconventional or conventional.

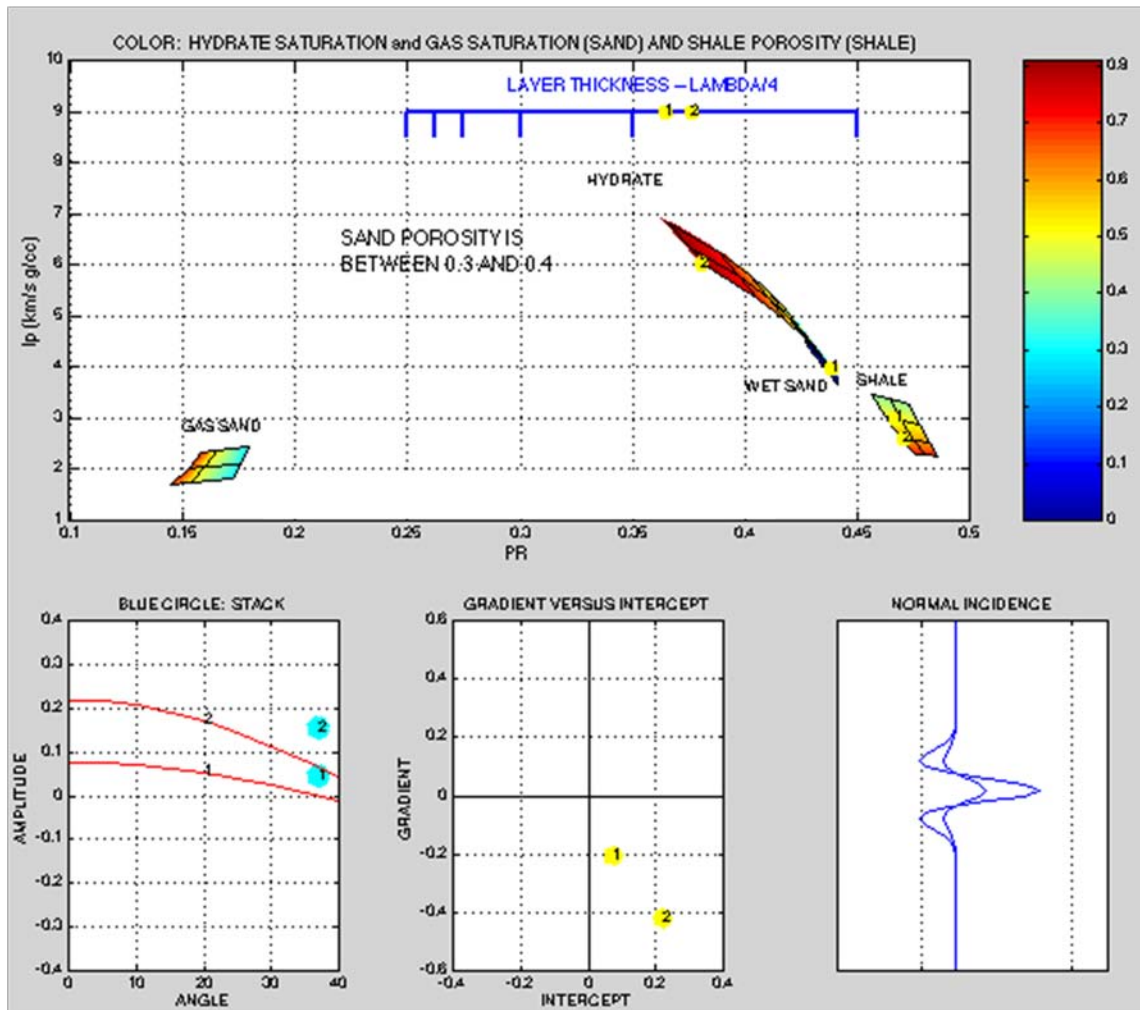


**Figure 8. Half-space AVO modeling for a methane hydrate reservoir. The upper panel is an impedance versus Poisson's ratio cross-plot where we map the domains occupied by soft shale, sand with hydrate, and gas sand according to the rock physics model described in the text. The shale domain is color-coded by the total porosity; the hydrate sand domain is color-coded by methane hydrate saturation; and the gas sand domain is color-coded by gas saturation. The AVO curve is computed at the interface between shale and hydrate sand with parameters marked by yellow symbols and numbers. The hydrate layer thickness is expressed in fraction of the wavelength. The numbers in the AVO and gradient-intercept frames correspond to the triplets in the upper frame. The waveforms in the bottom-right frame are from the convolution of a Ricker wavelet with the normal-incidence reflectivity at the interface. The thickness of the layer is accounted for by assuming that the stratum beneath it has the same elastic properties as the overburden and then Backus-averaging them with those of the layer.**

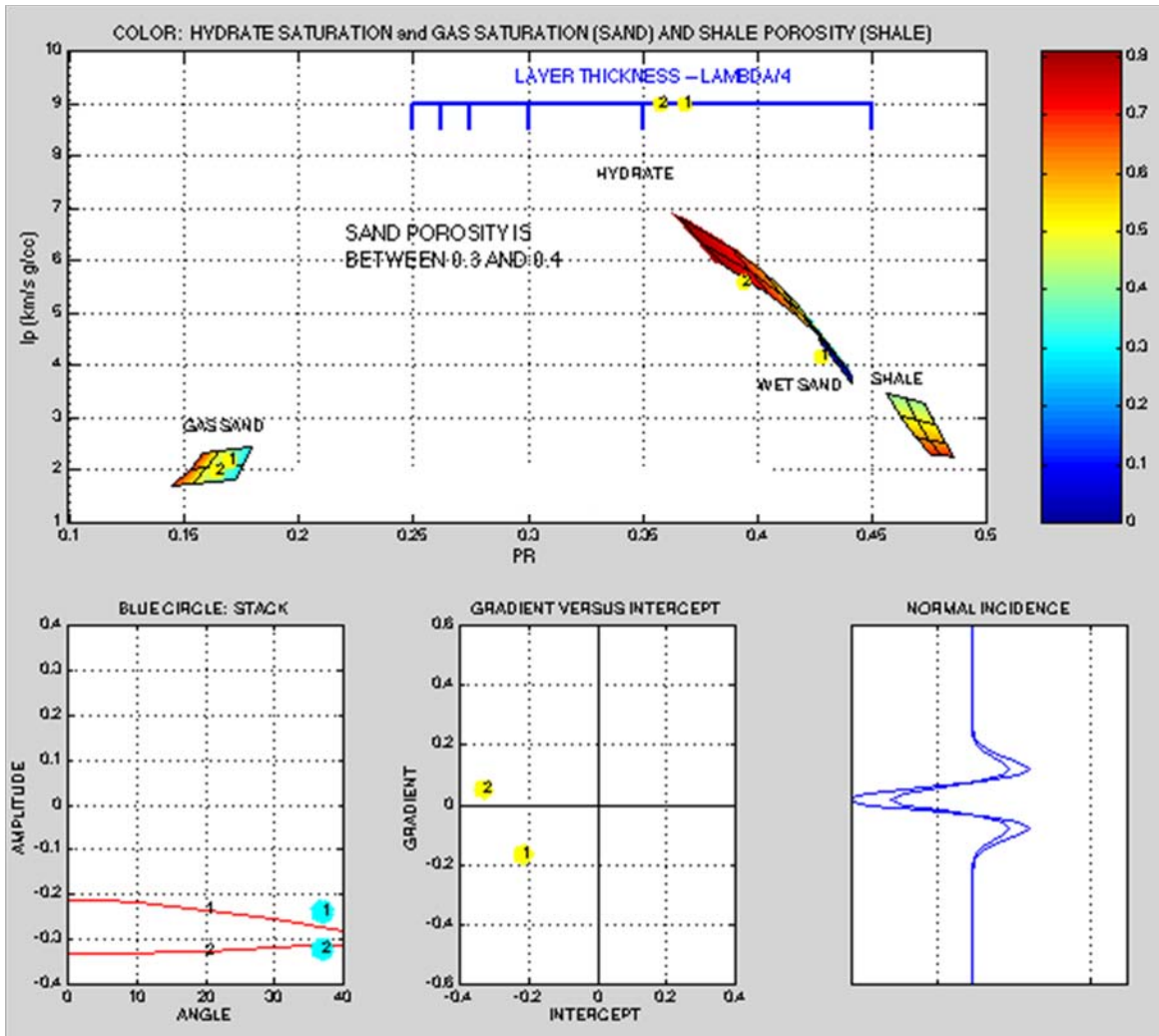


**Figure 9. Same as Figure 8 but for reflections between hydrate and free-gas sand.**

By systematically perturbing the volumetric properties and conditions as well as the thickness in the subsurface, one can generate a catalogue of the corresponding seismic signatures (Figures 8 and 9) to match a real case. The supposition is that if the seismic response is similar the underlying earth properties are similar as well. Of course, this solution is non-unique simply because more than one set of properties and conditions can produce the same response.

Once again, using an appropriate rock physics model calibrated at the site of investigation is a key in such forward modeling.

The solution proposed here is appropriate for direct quantification of a hydrate reservoir from seismic data, specifically from the seismic impedance. Another and very powerful solution

partly discussed in previous sections is physics-based perturbational forward modeling of the seismic amplitude.

### ***E. Conclusion***

The use of a first-principle-based rock physics model is crucial for gas hydrate reservoir characterization because only within a physics-based framework can one systematically perturb reservoir properties to estimate the elastic response with the ultimate goal of characterizing the reservoir from field elastic data. Intrinsic and scattering attenuation due to the presence of gas hydrate may noticeably affect the seismic amplitude and, therefore, has to be taken into account during modeling and interpretation of seismic data. It can also serve as an indicator of a gas hydrate reservoir. Reservoir geometry and thickness affect the seismic amplitude. Therefore, rock physics based approach has to be upscaled to become applicable to seismic reservoir characterization where seismically derived acoustic and elastic impedances are used. One way of upscaling – using cumulative seismic attributes to map accumulated reservoir properties is introduced and discussed in the previous section. The challenge and road ahead is to rigorously apply it to a carefully selected data set that contains both well and seismic data for the purpose of method calibration and blind testing at selected wells.

### **3. Cumulative Attributes (CATTs) on Milne Point Seismic Data.**

CATTs are obtained by cumulative integration and reflect a summation of petrophysical properties. Thus, they represent bulk properties rather than a single point response. These attributes are designed based on specific rock physics transforms that relate gas hydrate saturation to P-wave velocity.

Two seismic cumulative attributes, saturation and accumulative volume, have been computed. Saturation is a cumulative property that relates the fraction of hydrate concentration to acoustic impedance. Cumulative volume is a correlation between impedance and hydrate percentages across a hydrate bearing interval.

In order to calculate CATTs on seismic data it is necessary to use rock physics transforms that are case specific. Thus, the transforms employed in this study are valid for this specific area, Milne Point.

The first step is to extract a trace at the well location the relative seismic impedance and calibrate it to log impedance. The calibration is performed by matching the peak log and seismic impedance at 513 msec at WELL A location. The following transform matched and converted the relative seismic impedance to the impedance at the well:

$$I_p = Z_p(\tau) / 2000 + 4.5 \quad (5)$$

where  $I_p$  is the calibrated impedance in km/s gr/cc and  $Z_p$  is the relative seismic impedance.

Figures 10 to 12 display the relative and calibrated impedances at the three well locations. The top frame displays the relative seismic impedance ( $Z_p$ ). The lower frame displays the smoothed log impedance (dashed light blue), the calibrated synthetic impedance (dark blue) as well as the calibrated seismic impedance (magenta).

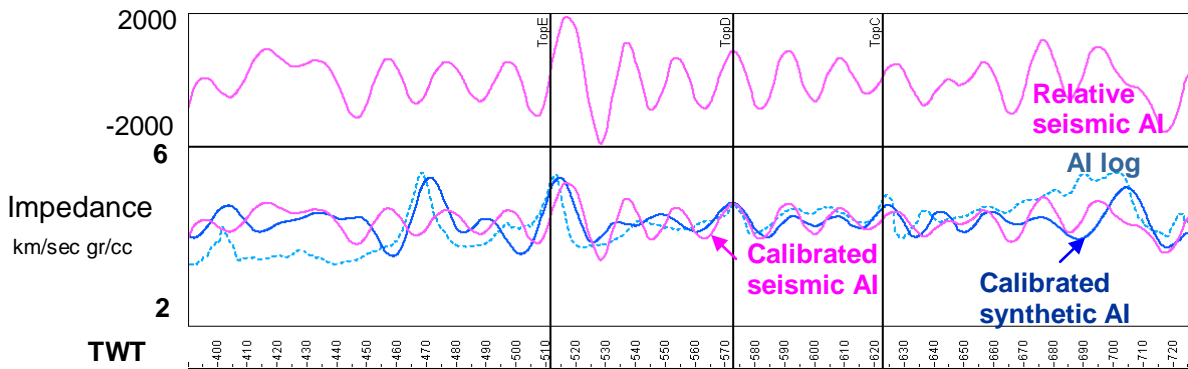


**Figure 10. Top frame: relative seismic impedance at WELL A location. Bottom frame: log impedance (light blue), calibrated synthetic impedance (dark blue), and calibrated seismic impedance (magenta)**

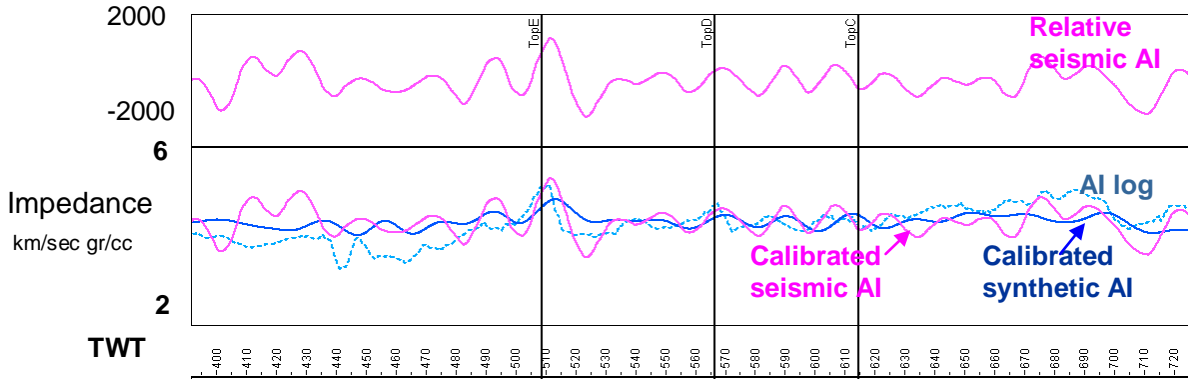


**Figure 11. Top frame: relative seismic impedance at WELL B location. Bottom frame: log impedance (light blue), calibrated synthetic impedance (dark blue), and calibrated seismic impedance (magenta).**

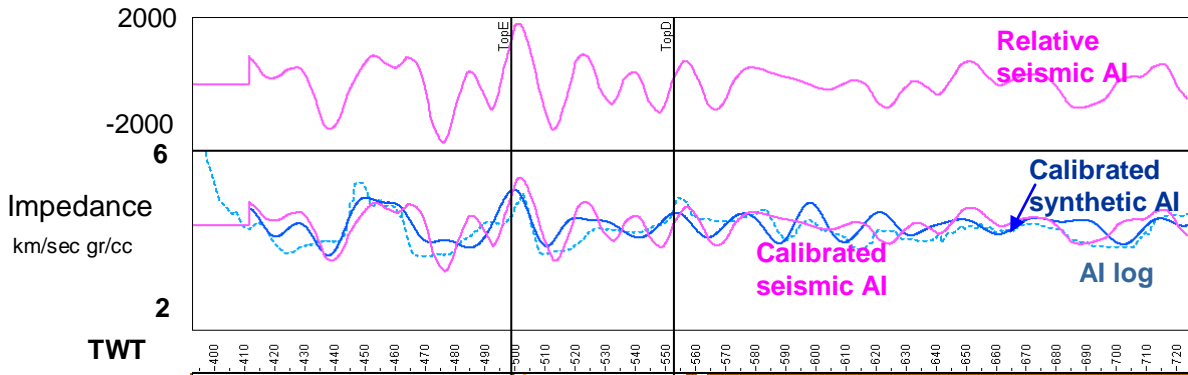


**Figure 12. Top frame: relative seismic impedance at WELL C location. Bottom frame: log impedance (light blue), calibrated synthetic impedance (dark blue), and calibrated seismic impedance (magenta).**

The match between the calibrated seismic impedance and the smoothed log impedance is satisfactory in WELL A but is less accurate in WELL B and WELL C. Nevertheless, the transform given in Equation (5) can be applied to the Milne Point relative seismic impedance volume.

The second step in calculating CATTs on the Milne Point seismic data is to estimate the gas hydrate saturation. The relationship between  $I_p^{-2}$  and hydrate saturation is an empirical relationship from well log data. It appears to be linear and the best fit can be expressed by:

$$Sgh = -28.207 / I_p^2 + 1.305 \quad (6)$$

where  $I_p$  is in km/sec gr/cc.

Figure 13 shows a crossplot between the inverse of the P-wave impedance squared ( $I_p^{-2}$ ) versus gas hydrate saturation ( $S_{gh}$ ). The data plotted come from all the three wells employed in this study.

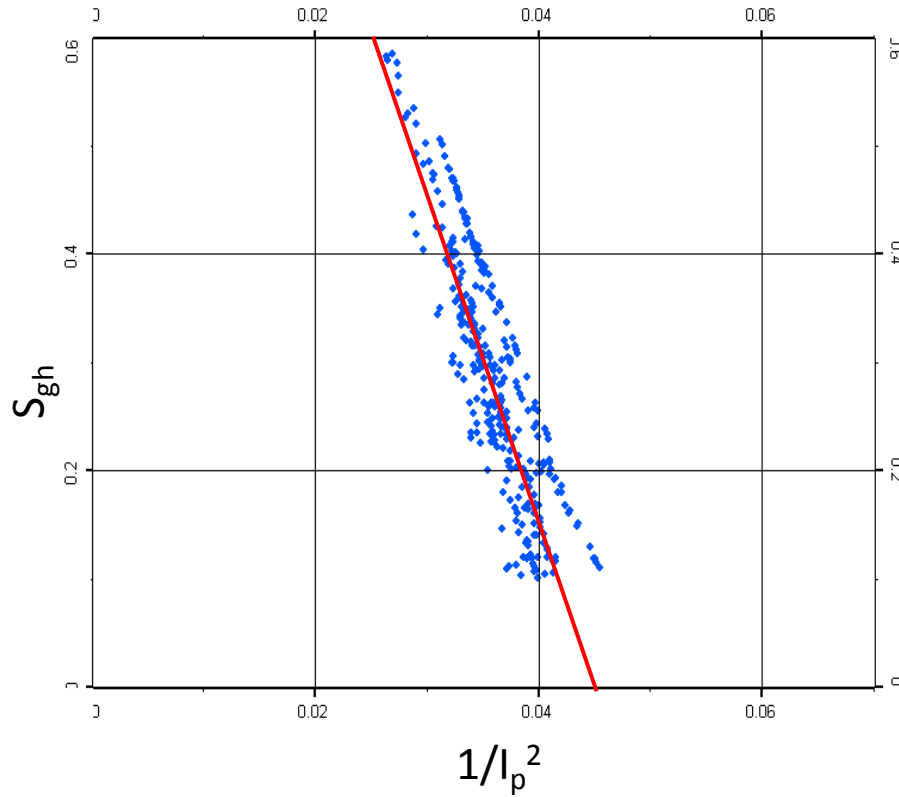


**Figure 13. Gas hydrate saturation versus inverse squared impedance. The red line is the best linear fit and is expressed by Equation (6).**

The third step in calculating CATTs on Milne Point seismic data is to estimate the accumulated gas hydrate volume. The accumulated volume of gas hydrates found between two vertical stations is:

$$V_{gh} = \int [-2.82I_p^{-1} - 0.13I_p] d\tau, \quad (7)$$

where  $I_p = Zp(\tau) / 2000 + 4.5$ .

The limits of integration for a hydrate volume in Equation (7) were set to 4.8 km/sec gr/cc. Accumulated gas hydrate volume is measure in hydrate volume per horizontal area ( $m^3/m^2$ ).

## ***A. Gas Hydrate Volume at Well A***

Once the seismic saturation and the cumulative volume of gas hydrates have been obtained, traces at the well locations from these two outputs are extracted. Figure 14, tracks 2 to 4, display the seismic data, the synthetic, and the seismic relative impedances at well A. Track 6 displays the smoothed log impedance (light blue), the calibrated synthetic impedance (dark blue), the calibrated seismic impedance (magenta), and the impedance cutoff (dashed black). It is important to stress that the integration for calculating accumulated hydrate volume is performed at impedances higher than the cutoff, in this case 4.8 km/sec gr/cc.

Track 7 shows the estimated seismic hydrate saturation and the log hydrate saturation. Track 8 displays the accumulated gas hydrate volume calculate from well log data (light blue), from synthetic (dark blue), and from seismic data (magenta). This cumulative property calculated using well data differs from the one calculated with seismic data. The seismic computation is missing or is calculating gas hydrate in places that do not have gas hydrates according to well log data. For example well log data indicates a gas hydrate interval at 470 msec but seismic data does not have any reflector at that time. In addition, seismic data show anomalies that would indicate gas hydrates at 535 and 590 msec but well log data do not show them.

One of the assumptions about unconsolidated sediments with gas hydrates is that these sediments present P-wave impedances much larger than the surrounding unconsolidated sediments without gas hydrates. This is true in some places, but clearly this is not the case everywhere. Reflectivities in some of the small hydrates accumulations are not large enough to bring them above the background. As a result, the method successfully detects some hydrates intervals but misses hydrate intervals that do not have seismic expression and also detects some false positives.

However, note that the accumulated hydrate volume in track 8 does match the well log-derived CATTs volume. This is obviously the result of hits, misses, and false positives, but does demonstrate that this method might show promise for approximated quantifying gas hydrate volume.

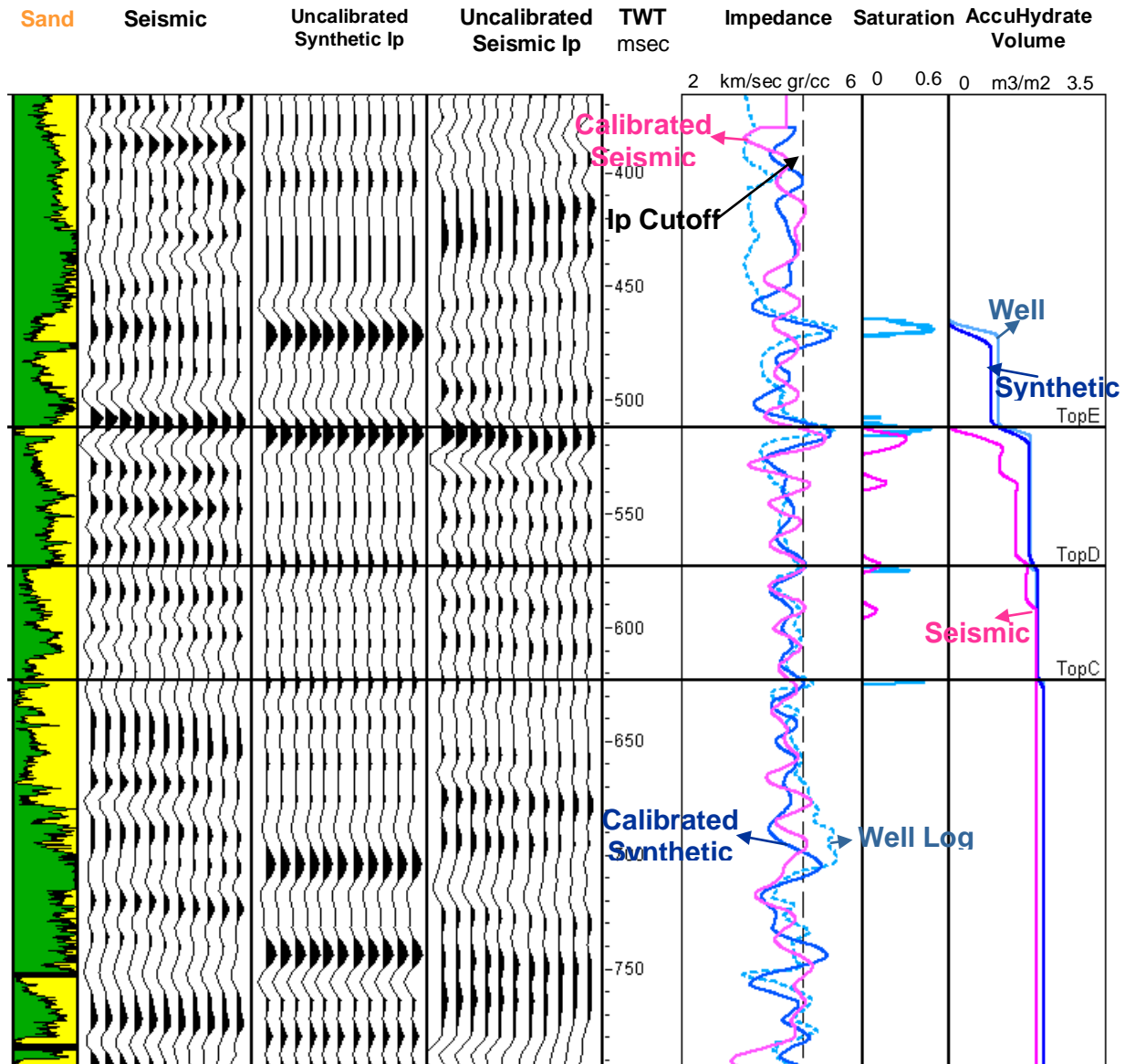


Figure 14. Comparison between CATTs from seismic data and CATTs from well log data.

### B. Post-Stack Inversion Of Milne Point Seismic Data.

Since seismic data are frequency-limited then the derived impedances also will be band-limited. To transform the band-limited impedances to absolute impedances, a low frequency background model must be generated (Figure 15). To create the low frequency background model, smoothed seismic horizons, smoothed well log data, and RMS velocities are used as inputs to the geostatistical volume.

Mapping seismic horizons rely on extracting amplitude values at peaks, troughs, or zero crossings on a specific reflector throughout the volume. For this study two horizons were mapped, one at around 350 msec and the other one at around 810 msec. Mapping those seismic horizons was challenging due to the complex structural geology in the area.

Seismic velocities along with well data were inputs to the low frequency model. The seismic velocities were calibrated to well control data through seismic to synthetic well ties. WELL A, WELL B, and WELL C wells were used as well control in this study. Through geostatistics, the smoothed well log information was interpolated following an internal structural style which should honor the geology. For this study the style that best described the geology was the proportional topology, in which the sub-layers conform parallel to the mapped seismic horizons.

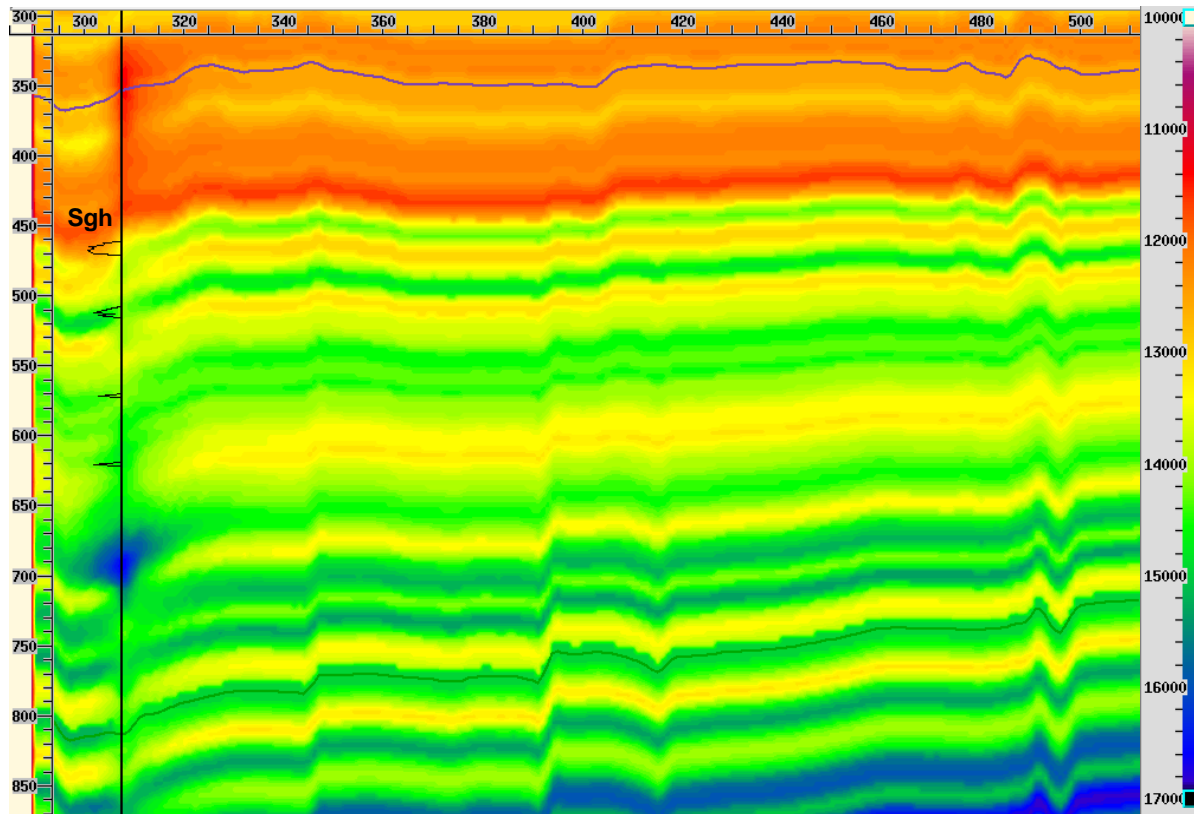


**Figure 15. Background P-impedance model, IL 449, with unnamed well location and calculated hydrate saturation curve (Sgh).**

In addition to the background model a composited wavelet is computed using a module developed at RSI. The composited wavelet is the combination of different wavelets. Figure 16

shows the main analysis window of the tool. Three wavelets were loaded which were estimated at WELL A, WELL B, and WELL C locations. The top row of the display shows the individual wavelets, their amplitude, their frequency, and phase spectra. The bottom row shows the composite wavelet, its amplitude, frequency, and phase.

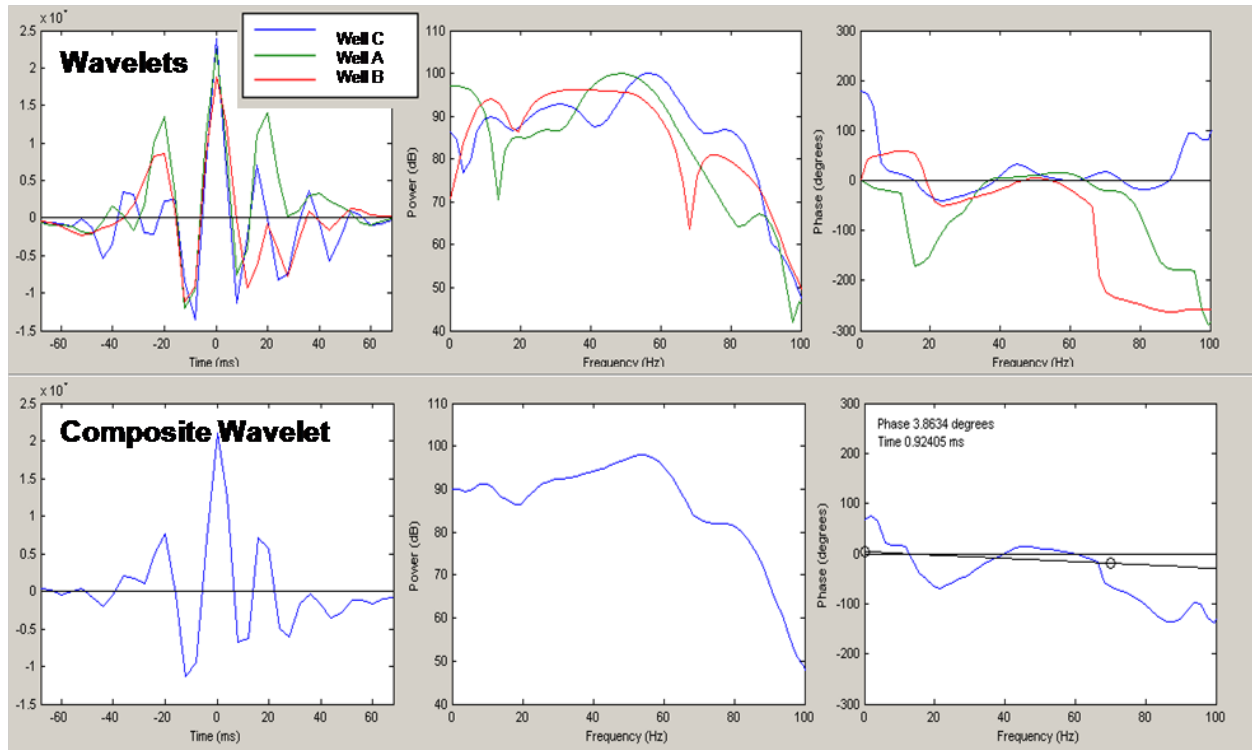


**Figure 16. Compositd wavelet from WELL A, WELL B, and WELL C. The top shows the amplitude, frequency, and phase of the wavelets extracted for each well. The bottom shows the compositd wavelet formed from the three wavelets, its amplitude, frequency, and phase.**

With the compositd wavelet, background model, and seismic stack, the inversion is performed. Inversion is an iterative process, so parameters are adjusted through error minimization. Thus, many inversions were performed with different parameters. Figure 17 shows the best case impedance estimate for Milne Point.

The most common inversion parameters tested for optimization are noise factor and standard deviation. Noise factor indicates how much seismic information is used in the inversion and varies from 0 to 100. A value of 10 indicates a high confidence in the fidelity and accuracy of the seismic data. Standard deviation is the maximum allowable variation from the background model. In this case, a standard deviation of 1000 means that inverted impedances are allowed

to deviate from the model impedances by 1000 AI units. This provides constraints to make sure the inversion does not generated unrealistic results.

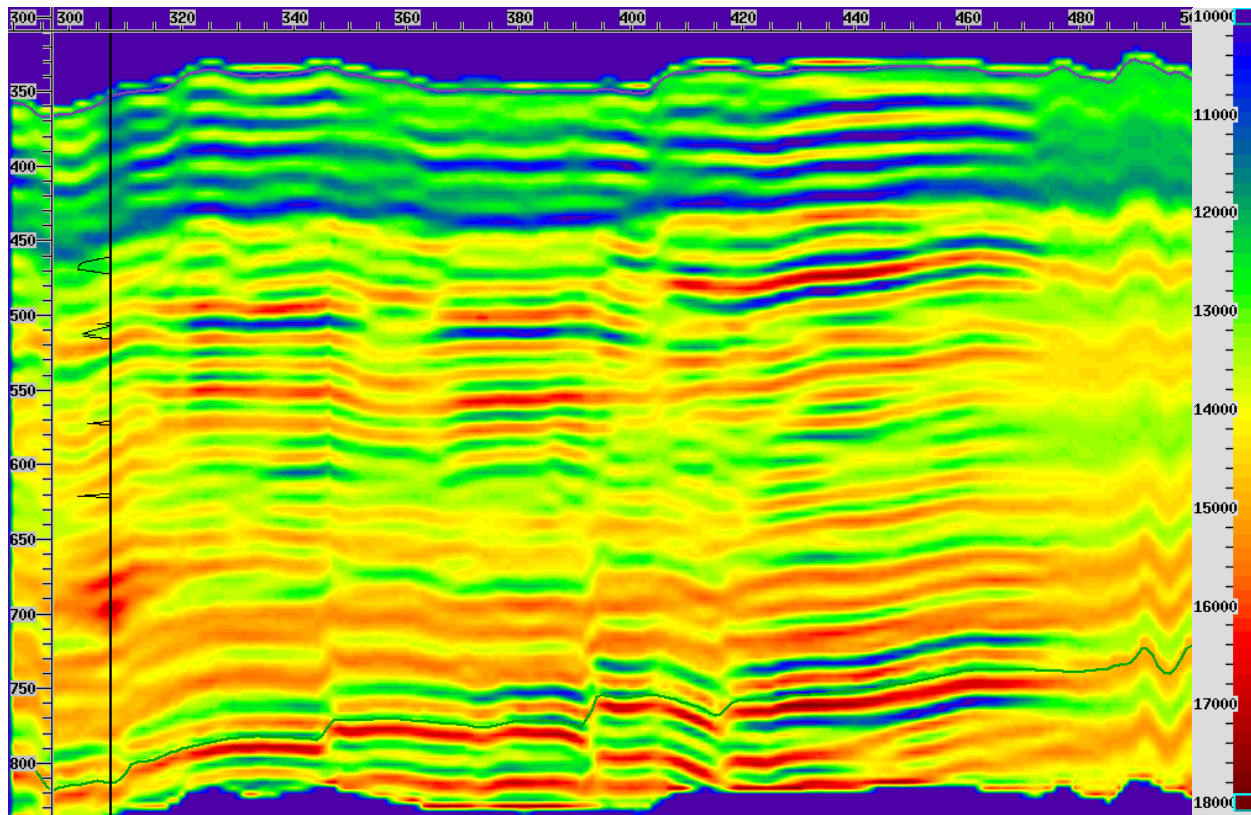


**Figure 17. P-wave impedance from the post stack seismic data, IL 449, with unnamed well location and calculated hydrate saturation curve (Sgh).**

Figure 18 displays an inversion quality control. It is the comparison of the extracted impedance curve from the inverted volume and the upscaled impedance well log curve. The two curves overlay each other closely meaning that the inversion is matching the well log data very well.

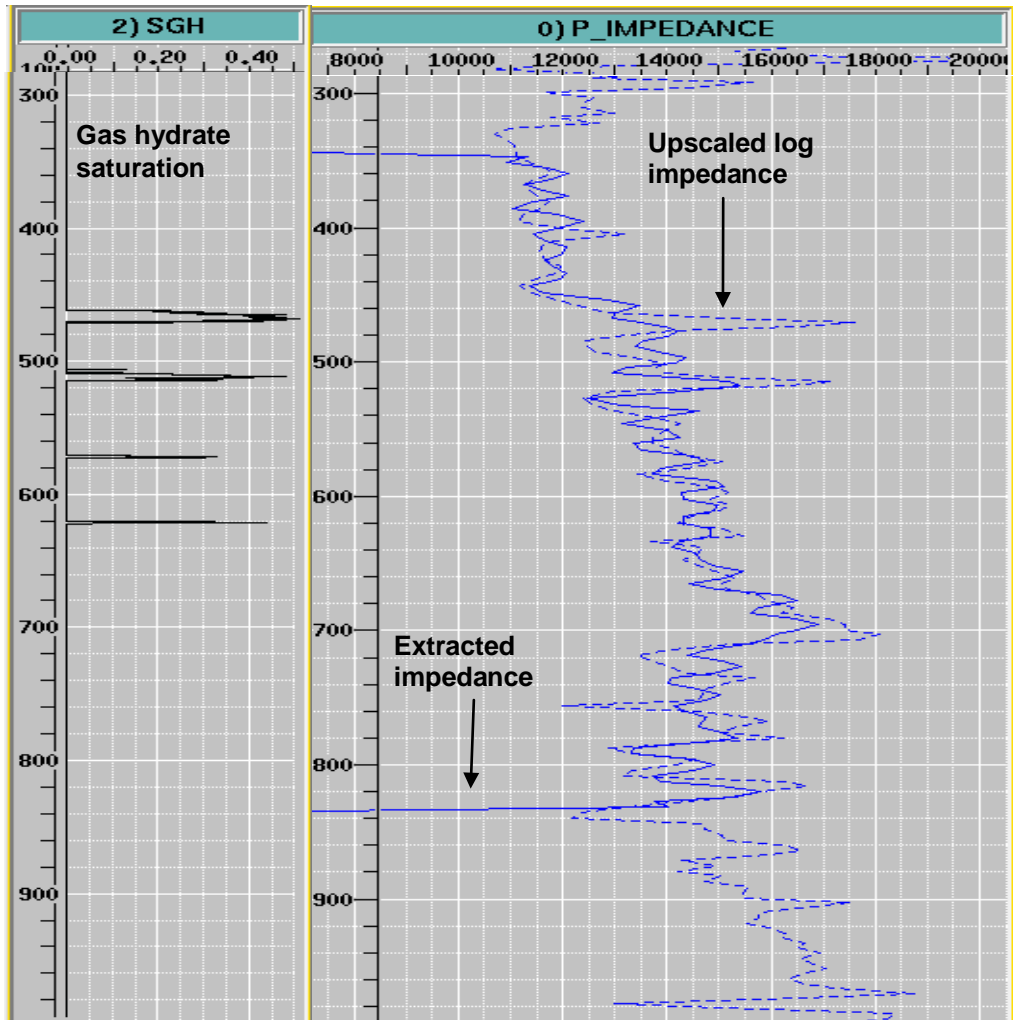


Figure 18. Overlay of upscaled P-impedance log (dashed line) and extracted P-impedance trace from the inversion (solid blue line). Left panel is the hydrate saturation log in decimal %.

## 4. Geological Controls On Methane Gas Hydrate Occurrence

### ***A. Introduction***

Channel & levee sands deposited by Paleocene rivers running through graben fault blocks contain the highest saturations of methane gas hydrate. Although gas hydrate formation is confined to discrete, experimentally determined temperature and pressure stability fields, all conditions regarding the classic components of a hydrocarbon trap (source, timing & pathway of migration, reservoir, seal, etc.) still had to have been met for the actual gas hydrate to materialize afterwards. Aforementioned constraints on trap formation in conjunction with the following subsurface aspects govern much of methane gas hydrate resource occurrence beneath Milne Point, Alaska:

#### **Vertical gas hydrate formation**

1. Regional accumulation of gas hydrate is closely linked to the presence of a sealing unconformity at the base of the Eocene that currently “doubles” as the permafrost base
2. In a general sense, hydrate saturation steadily decreases from sand to sand found below this boundary.
3. Although hydrates are encountered in both, interpreted fluvial and deltaic/ shallow marine (?) sands, fluvial deposits boast methane gas hydrate saturations that are higher by about 15% than those found in marine sands, for a maximum of about 50%. Fluvial reservoirs comprise cleaner sands, possess greater connectivity, and, as a consequence, may have provided faster and extended regional reach for gas entrapment?
4. In contrast, clastic progradation is often accompanied by clinoform deposition which in turn tends to compartmentalize potential reservoirs by intercalation of small flooding surfaces (high  $V_{CLAY}$ ). These parasequence boundaries effectively inhibit higher gas hydrate saturations observed in fluvial sands (channel, levee, pointbar).
5. A change in paleoenvironment from regressive shoreface to a more channel-dominated fluvial facies mid-way through the hydrated section is evidence for a

basinward translation of coastal facies. Although the overall stratigraphic pattern is progradational (“regressive” section), the fluvial channel sands could possibly represent low-stand systems tract deposits that incised deposits of an earlier highstand systems tract.

6. Low-saturation methane gas hydrate occurring in shale section immediately overlying channel sands may attest to time-transgressive gas seepage frozen in time or, possibly, diffusion.

### Lateral gas hydrate formation

1. Lateral sand distribution is partially controlled by extensional tectonics, in that sands tend to occupy topographic lows provided by graben blocks
2. Locally, where meandering rivers are banked against faults, higher gas hydrate saturations appear to have become compromised, a phenomenon possibly suggestive of hydrate instability due to frictional heating/conductive heat flow.

## B. Geological Models

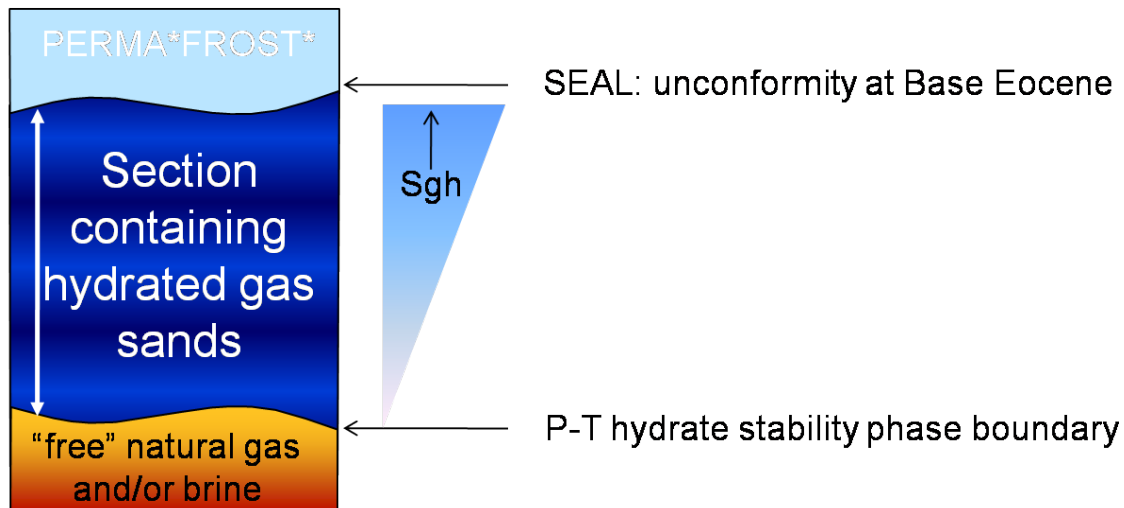


**Figure 19. Geological model of hydrate saturation.**

A geological model (Figure 19) depicts hydrate saturation to increase vertically, attaining a hypothetical maximum at a postulated pre-existing sealing boundary provided by an unconformity at the base of the Eocene. Another geological model (Figure 20) addresses the

observed overall progradational signature of clastic sequences that is paralleled by a basinward shift of paleoenvironments, as evidenced from a higher frequency of fluvial deposits beginning from the middle of the section toward the base of the Eocene.

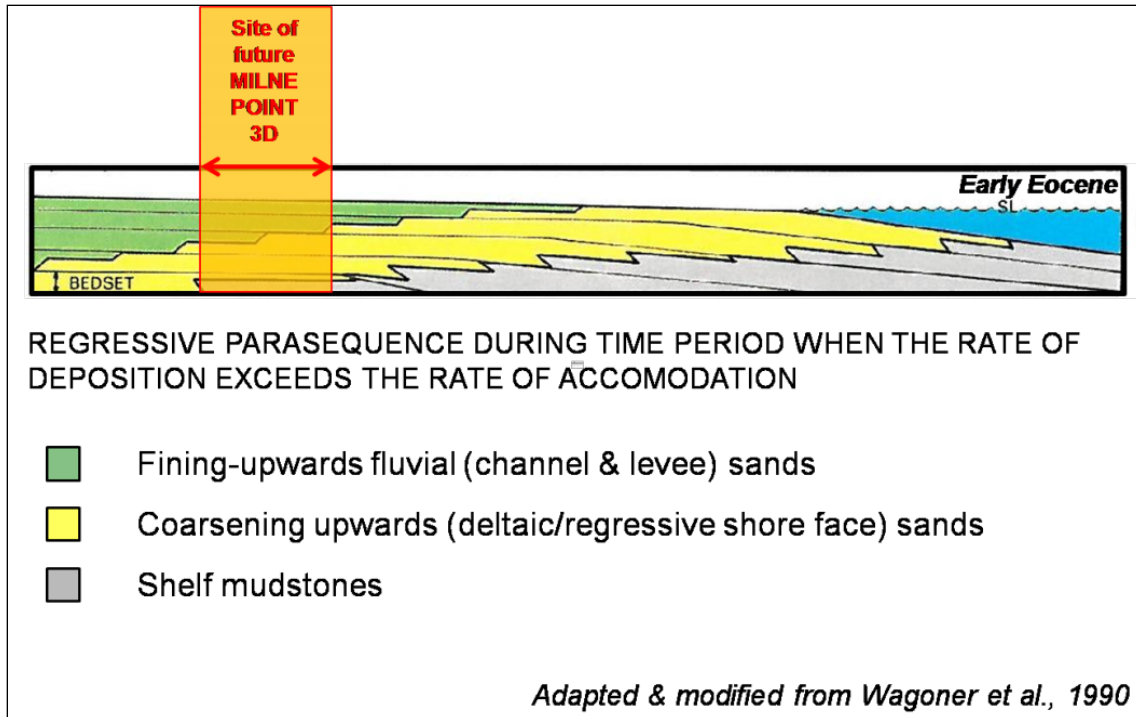


**Figure 20.** Sequence stratigraphic model.

### **C. Tectonics**

Since reservoir sands generally resonate at higher impedance values than shales, a side-by-side comparison of a time structure map to a horizon-based P-wave impedance value extraction map suggests that “E” layer sands accumulated within longitudinal, crudely NS-trending *graben* fault blocks (Figure 21). For seismically resolved sands, P-wave impedance attribute values resonate above a threshold value of about 15,000 kilorays, but that does not necessarily imply that such sands are fully hydrated.

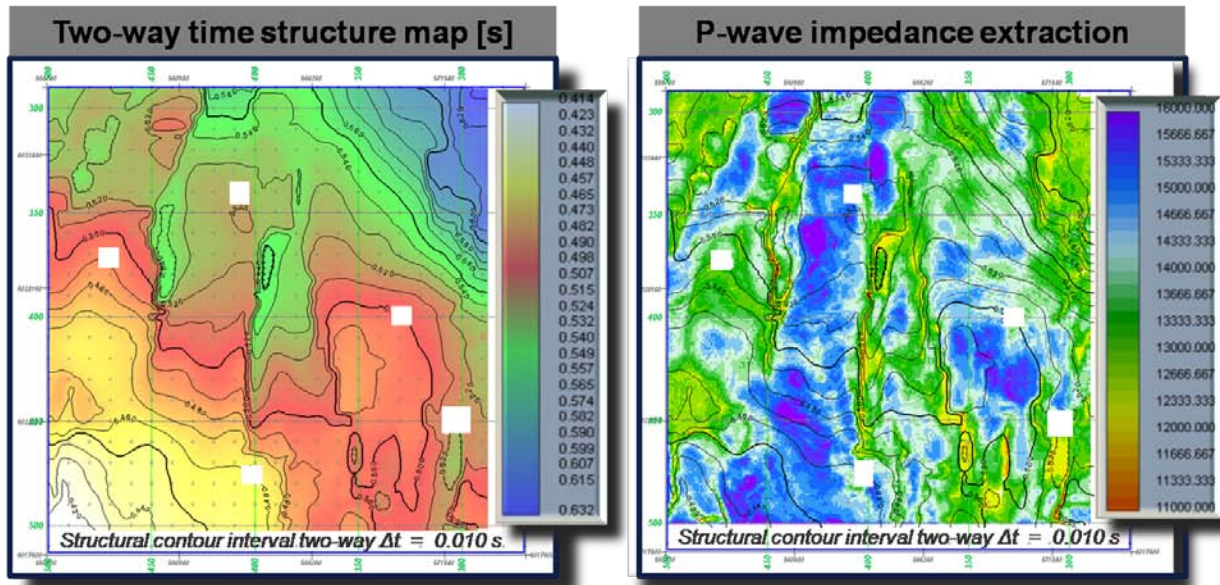


**Figure 21.** Left: Structure map (in seconds two-way travel time), right: map of extracted P-wave impedance (P-wave impedance [kilorays]) at the “E” sand level. Side-by-side comparison of map data suggests confinement of hydrated section to structural compartments provided by graben fault blocks. All confidential location and identification information has been removed honoring showright restrictions (white squares).

#### **D. Paleoenvironment**

Superposition of a  $V_{\text{CLAY}}$  log curve onto the seismic section known to retain hydrate identifies numerous, characteristic coarsening-upward cycles (Figure 22). Together with toplap (in this case characterized by reflection configurations terminating against the sequence boundary from below to form a complex seismic stratigraphic pattern known as “oblique progradation”) the coarsening-upward  $V_{\text{CLAY}}$  log curve shapes generally support a systematic seaward shift of coastal onlap (Figure 23).

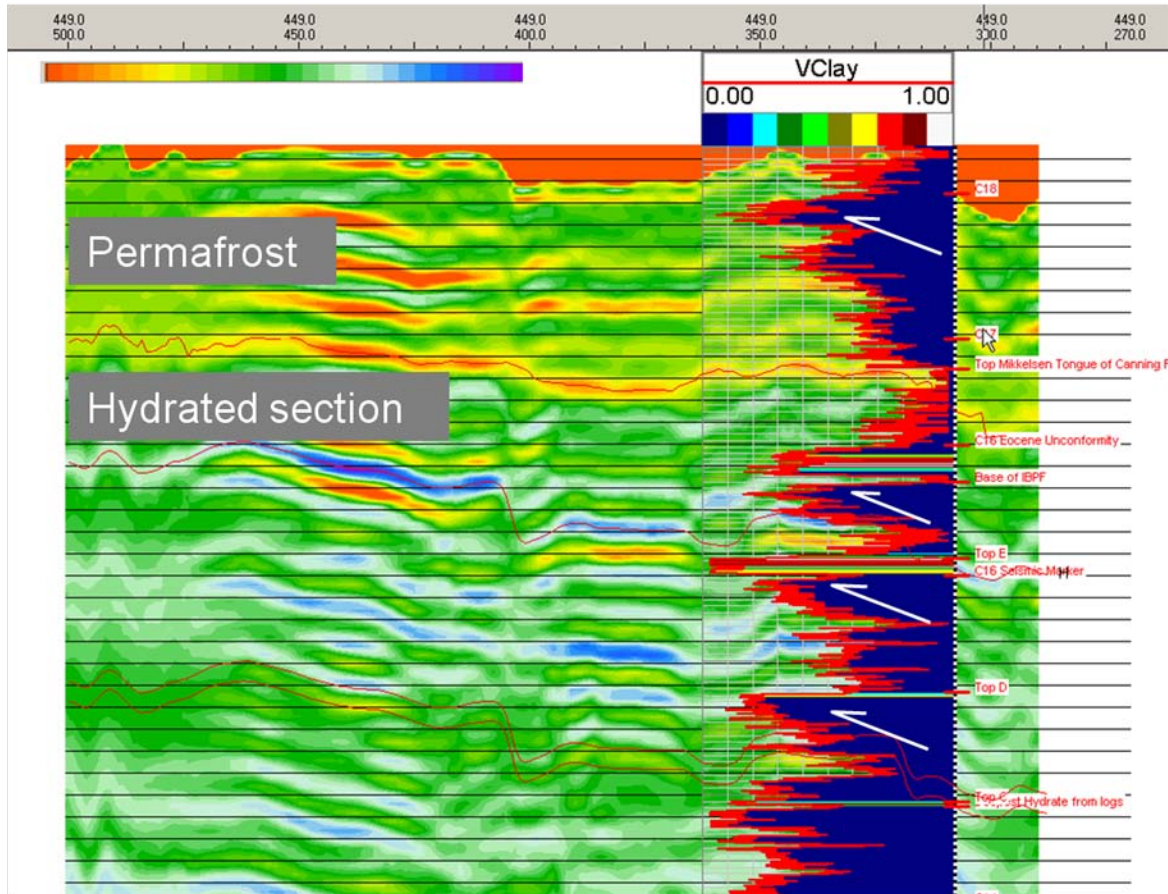


**Figure 212.**  $V_{CLAY}$  log shapes color-coded by gas hydrate saturation, unnamed Milne Point well. Arrows identify “coarsening-upward” trends. Due to showright restrictions no time scale may be provided.

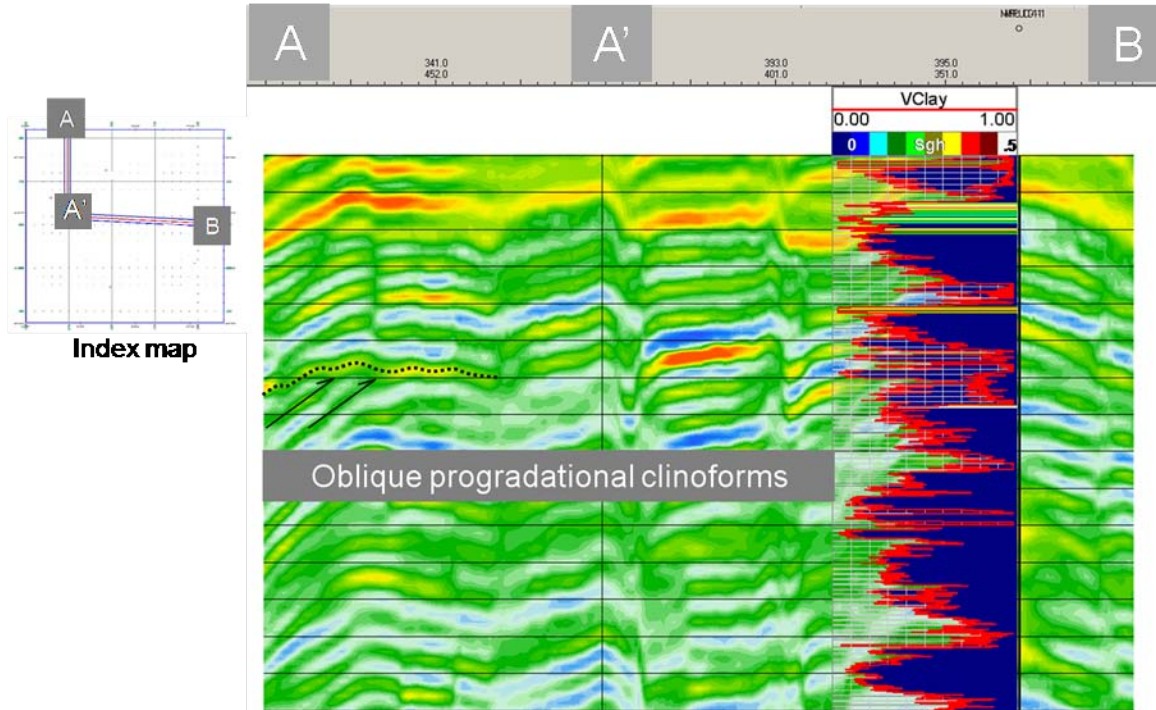


**Figure 223.** Arbitrary seismic traverse showing P-wave impedance section draped with  $V_{clay}$  log shapes color-coded by gas hydrate saturation, unnamed Milne Point well. Black arrows on seismic section denote toplap recognizable by reflection configurations terminating against the sequence boundary from below forming a complex seismic stratigraphic pattern known as “oblique progradation.” Insert shows arbitrary line orientation. Due to showright restrictions no vertical scale may be shown.

However, at a finer scale, we observe additional  $V_{CLAY}$  log curve shapes within the hydrated section that conform to generally accepted interpretations of other paleo-depositional environments (Figure 24). For instance, fining-upward cycles, interpreted as amalgamated fluvial channel-fill deposits, become more frequent in the upper half of the hydrated section, at the “D” and “E” sand levels, and above (Figures 24-27) (for stratigraphic position of sands, see Figures 14 and 22). Fluvial deposits ultimately prove very significant because retention of the highest hydrate saturations occurs in interpreted channels, point bars, and associated levees (Figures 24, 26). All channels are amalgamated, the youngest channel complex could be interpreted as multi-storey (Figure 24, panel 1), the other two channels are amalgamated and interpreted as being single-storey.

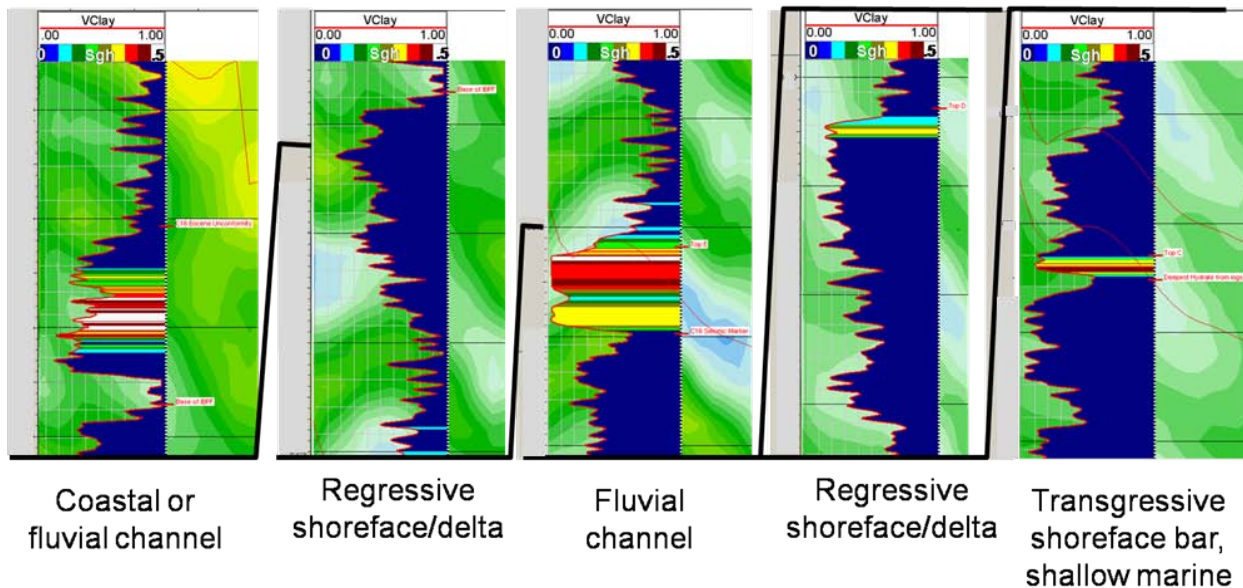


**Figure 234. Detailed successive seismic panels featuring  $v_{clay}$  log shapes incrementing by 5% steps in gas hydrate saturation (expressed as a fractional percentage, using a graduated color bar to denote the interval from zero to 0.05 [navy blue] and the interval from 0.45 to 0.5 [white]) at unnamed Milne Point well. Notably, methane gas hydrate saturations decrease from top to bottom of the depicted stratigraphic section. Locally, hydrate saturations are highest in fining-upwards cycles of interpreted fluvial deposits, and are lowest or absent in regressive shoreface/delta deposits. Channel deposits constitute less than 15% of the total time thickness of section capable of retaining hydrate. No vertical scale may be shown.**

#### In **fining-upward** cycles

- ❖ nearly the entire channel profile has become hydrated (Figure 24, panels 1 & 3)
- ❖ hydrate saturation ( $S_{gas\ hydrate}$ ) varies over the entire profile governed by  $V_{Clay}$  and structural elevation
- ❖ highest  $S_{gas\ hydrate}$  occurs near the channel top (locally, > 50%), lower  $S_{gas\ hydrate}$  occurs within channel stratification at amalgamation sutures (Figure 24, panel 3)
- ❖  $S_{gas\ hydrate}$  and  $V_{Clay}$  are inversely proportional (s. Figure 25)
- ❖ Channel sands are poorer in  $V_{Clay}$ , i.e., “cleaner,” than sands that coarsen upwards

#### In **coarsening-upward** cycles

- ❖ no hydrate may occur (Figure 24, panel 2)
- ❖ when saturated with hydrate, elevated concentrations occur near the parasequence top, at low  $V_{Clay}$  (Figure 24, panel 4)
- ❖ however, hydrate saturations are much lower ( $S_{gas\ hydrate} < 35\%$ ) than those found in the channel profile (s. Figure 25)
- ❖  $V_{Clay}$  climbs higher than in channel, i.e., slightly “rattier” sands

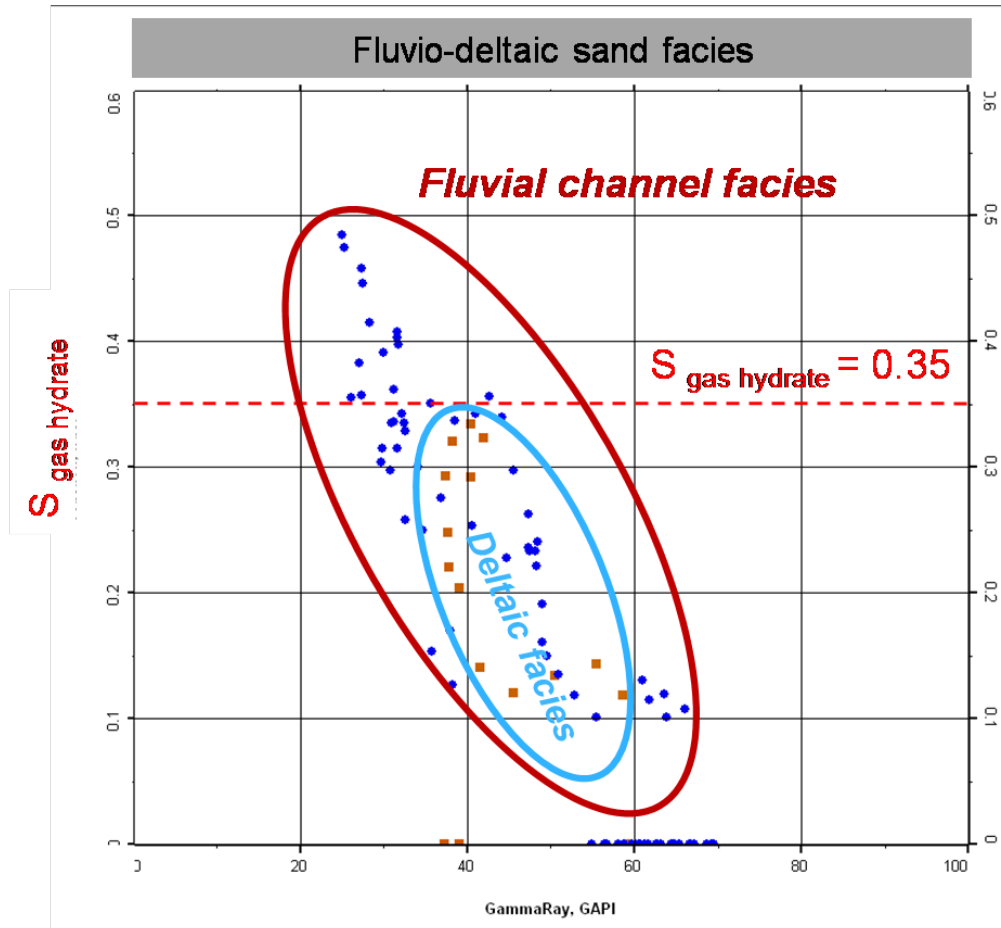


**Figure 245. Gamma ray versus methane gas hydrate saturation unnamed Milne Point well. Brown squares denote deltaic facies, blue dots identify channel facies.**

For a typical channel sand at Milne Point we find that  $S_{\text{gas hydrate}}$  and  $V_{\text{Clay}}$  are inversely proportional (Figure 25). Highest saturations occur in fining-upwards sequences (>35%). In fluvial channel profiles the highest gas hydrate concentration occurs near the top of the channel, before  $V_{\text{Clay}}$  starts to increase in the actual fining-upwards transition zone to the overlying shale section (Figure 26). Within the cleanest portion of the channel, the structurally highest position generally exhibits the higher saturation for similar fractional percentages of  $V_{\text{Clay}}$ . Lower  $S_{\text{gh}}$  occurs within the channel at amalgamation sutures.

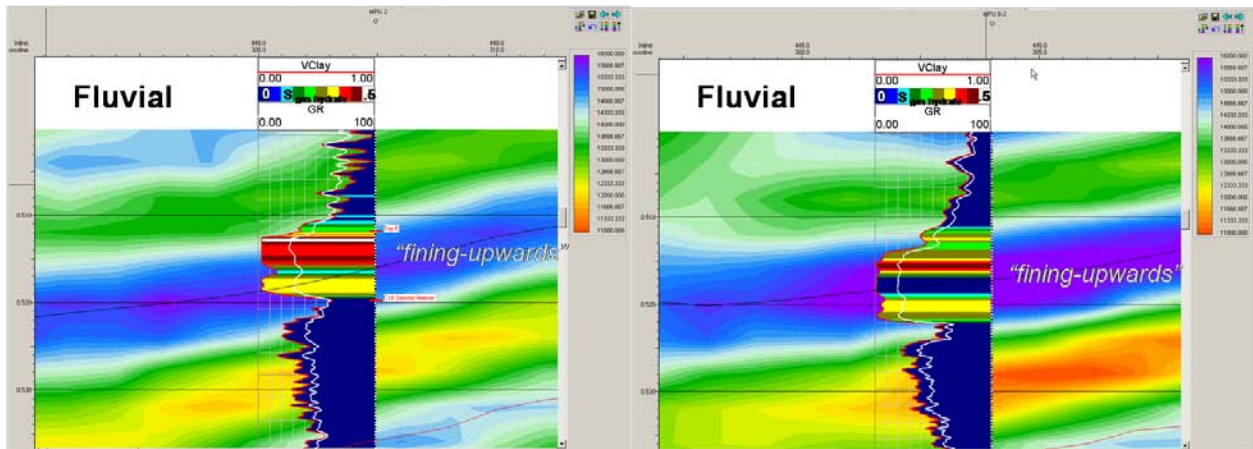


**Figure 256.**  $V_{CLAY}$  log shapes color-coded by gas hydrate saturation, for two unnamed Milne Point wells (with white GR curve overlay).  $V_{CLAY}$  log shapes have been color-coded by 5% increments in gas hydrate saturation (expressed as a fractional percentage, ranging from zero [navy blue] to 0.5 [white]) at these two neighboring wells.

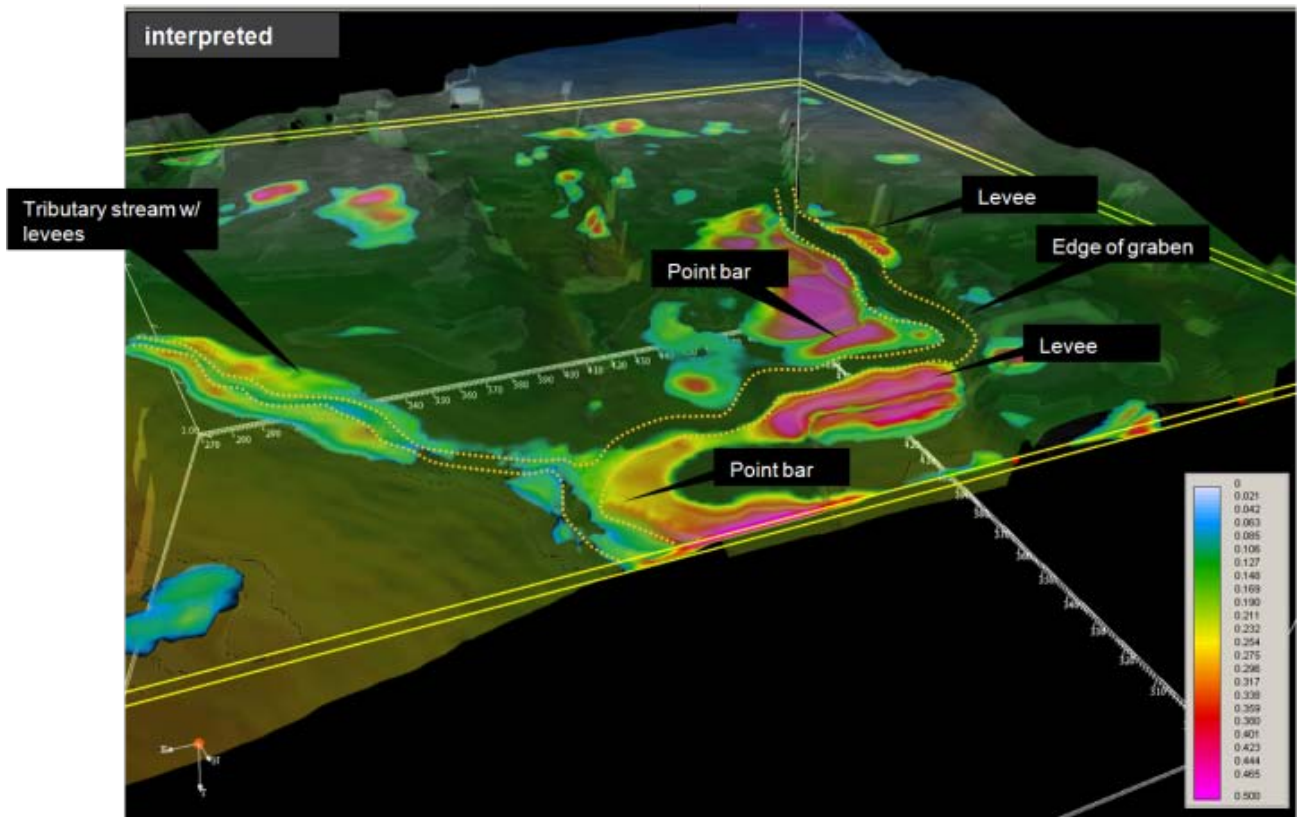


**Figure 267.** Perspective view of saturation cube from vintage point at the north end of the Milne Point 3-D survey. Hydrate-filled geobodies are interpreted as stratigraphic components (point bars, channel levees) of a fluvial paleo-river system (“E” Sand level). No vertical scale is shown due to showrights restrictions.

In opacity-rendered perspective views of a subsetting region of the saturation cube from the north end of the survey, hydrate-filled geobodies emerge that are interpreted as stratigraphic components (point bars, channel levees) of a fluvial paleo-river system (“E” Sand level) (Figure 27).

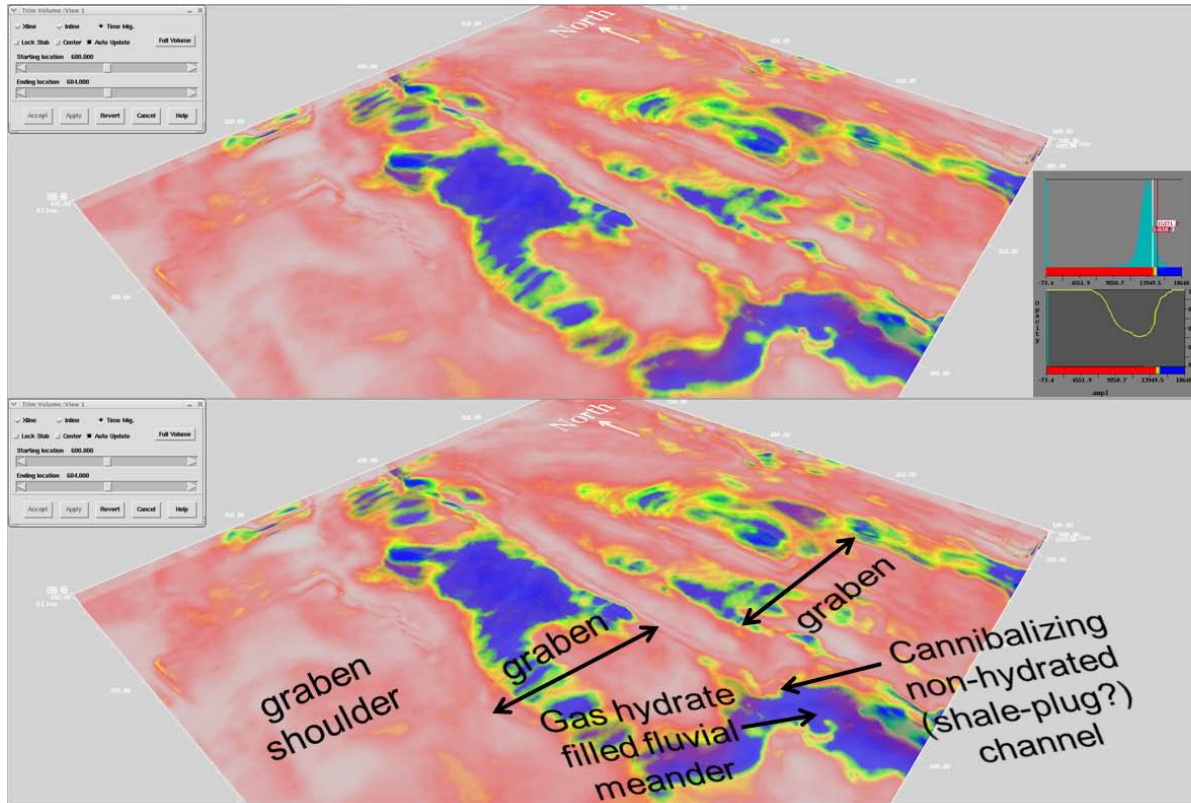


**Figure 278. Meander channel, “D”-sand level, uninterpreted & interpreted perspective views (for display purposes the volume is datumed on the E-horizon). No vertical scale is shown due to showrights restrictions.**

Additionally, an opacity-rendered acoustic impedance cube at the D-Sand level (Figure 28) reveals that hydrated sands conform to stratigraphy as well as to structure. There is minor evidence for cannibalization of future hydrate-filled channel sands by other, smaller channels that do not host hydrate later (possible shale plugs, oxbows, etc.). In any case, this observation suggests a stagnation in the rate of accommodation space. Field data support the presence of a major unconformity higher in the section (Base Eocene), but this may be the stratigraphic expression of a low-stand systems tract since these very deposits are downlapped by the oblique progradational clinofolds of an ensuing highstand systems tract already introduced in Figure 23.

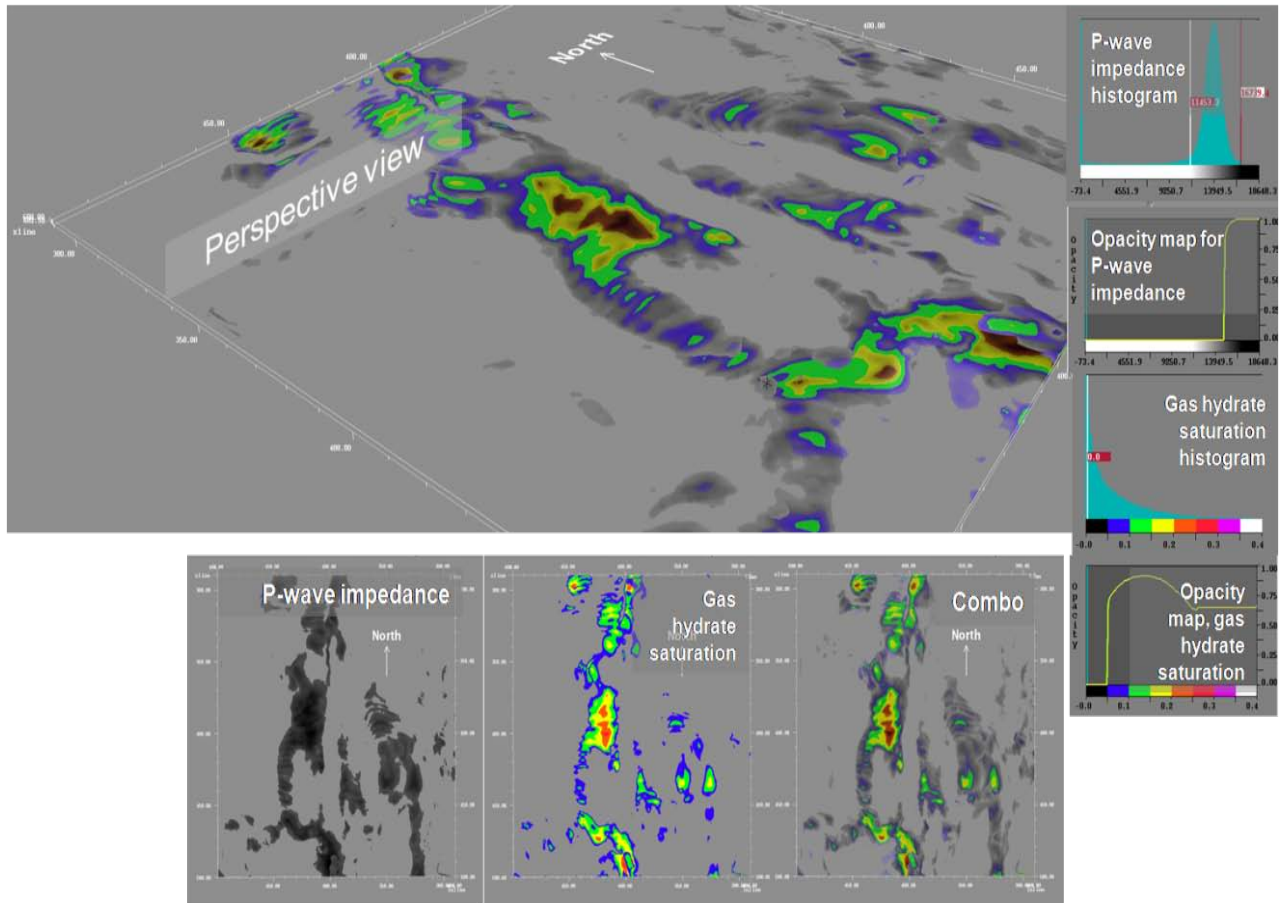


**Figure 289. Co-rendered attribute display of P-wave impedance and gas hydrate saturation attribute featuring meander channel at the “D”-sand level. Opacity color bars and attribute data histograms have been inserted on the right-hand side vertical panel. Base row features visual progression of adding partially rendered P-Wave impedance and hydrate saturation volumes into a single combination volume. No vertical scale is shown due to showrights restrictions.**

The volume combining partial opacity-rendered acoustic impedance and gas hydrate saturation at the D-Sand level (“Combo” volume; flattened on E-horizon; Figure 29) reveals that P-wave impedance values exceeding 15,000 kilorays with saturations greater than 5% generally exhibit a high degree of coupling between the presence of fluvial sand and high-saturation gas hydrate. The actual center of channel may locally exceed 25% gas saturation. However, elsewhere channel center sands are hydrated less than 5% (see next slide).

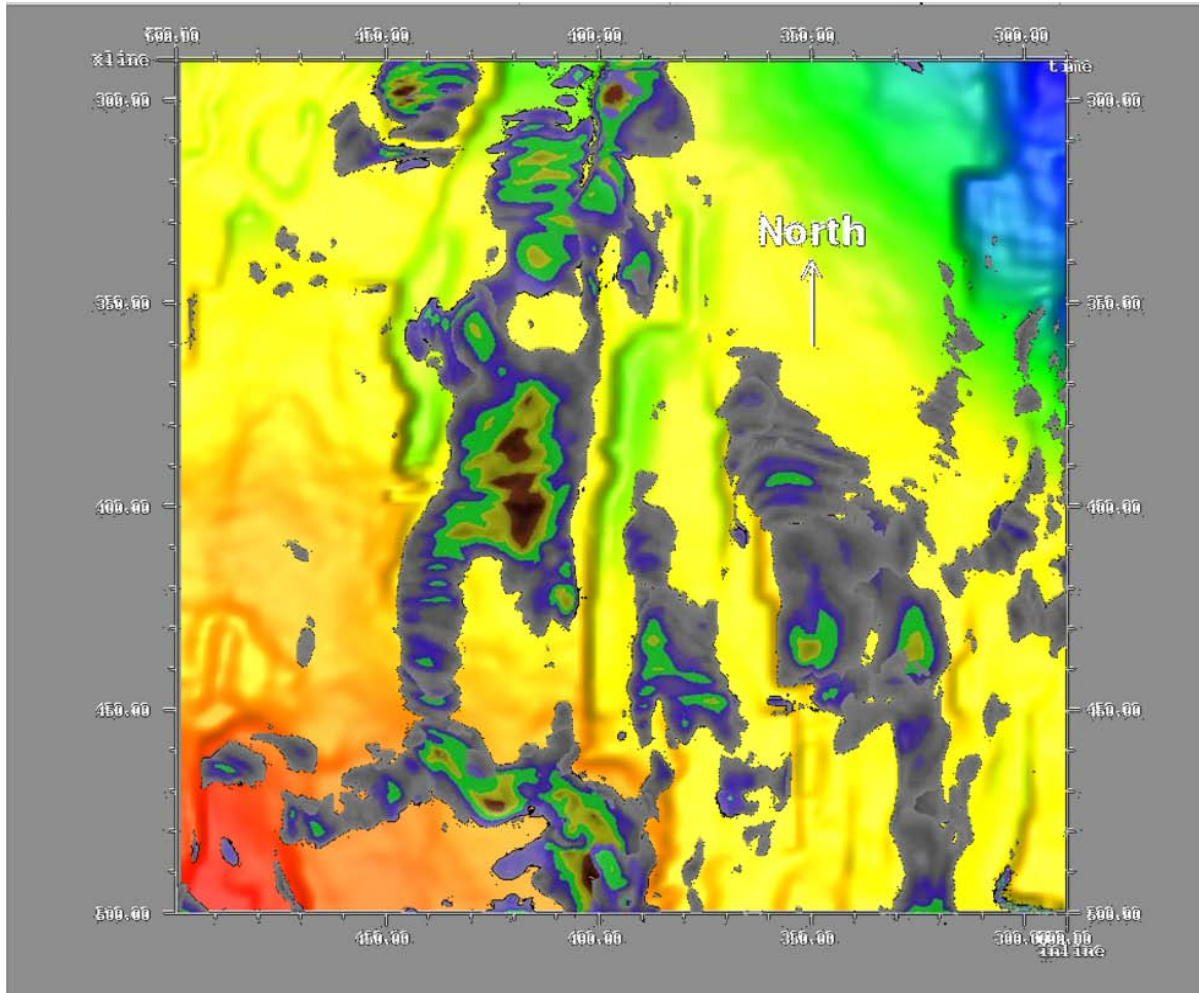


**Figure 30. Co-rendered attribute display of p-wave impedance and gas hydrate saturation attribute featuring meander channel at the “D”-sand level. Color bars as in previous slide.**

Underpinning (by downward bulk-shift) the time structure (warm colors = high on structure, cold colors = low on structure) for the overlying E Sand, it appears that gas hydrate saturations in the D sand drop considerably, wherever the course of the river channel runs parallel, and, in close proximity to, a fault strand (Figure 30). Lower gas hydrate saturations close to border faults may possibly hint at gas hydrate instability due to frictional heating (and fluid flow?) near reactivated fault segments? However, we do not observe any seismic evidence for catastrophic blowouts (“pockmarks”) on seismic maps above, and, therefore, we interpret the observed lower gas hydrate saturations where bordering normal faults lose slip to result from a lack of lateral seal.

## E. Resource Estimates

Contrasting maps views of cumulative Volume-Area attribute at different stratigraphic levels permits gauging of how quickly the hydrated section reaches its peak value.

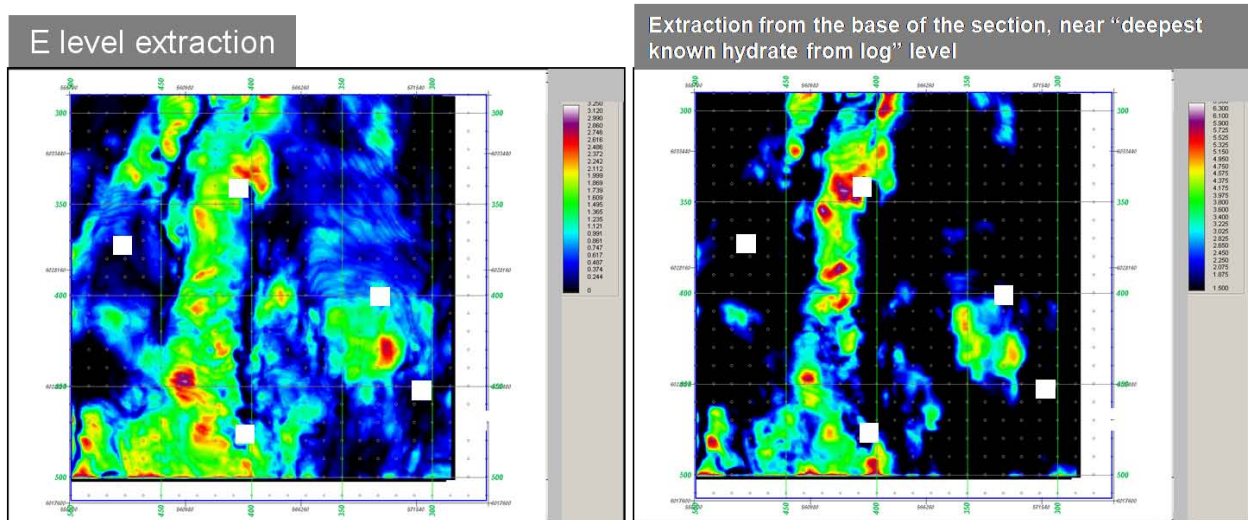


**Figure 29. Map views of cumulative gas hydrate volume attribute at “E” sand level (left) and at “deepest known hydrate from log” level (right). White squares conceal confidential location and identification information.**

Comparison of cumulative Volume-Area attribute at the E level to a horizon extraction from “deepest known hydrate from log” zone of this attribute reveals that 50% of the total gas hydrate saturation is already reached by the earliest encountered sands (Figure 31, left), less than mid-way into the section capable of retaining hydrated sands.

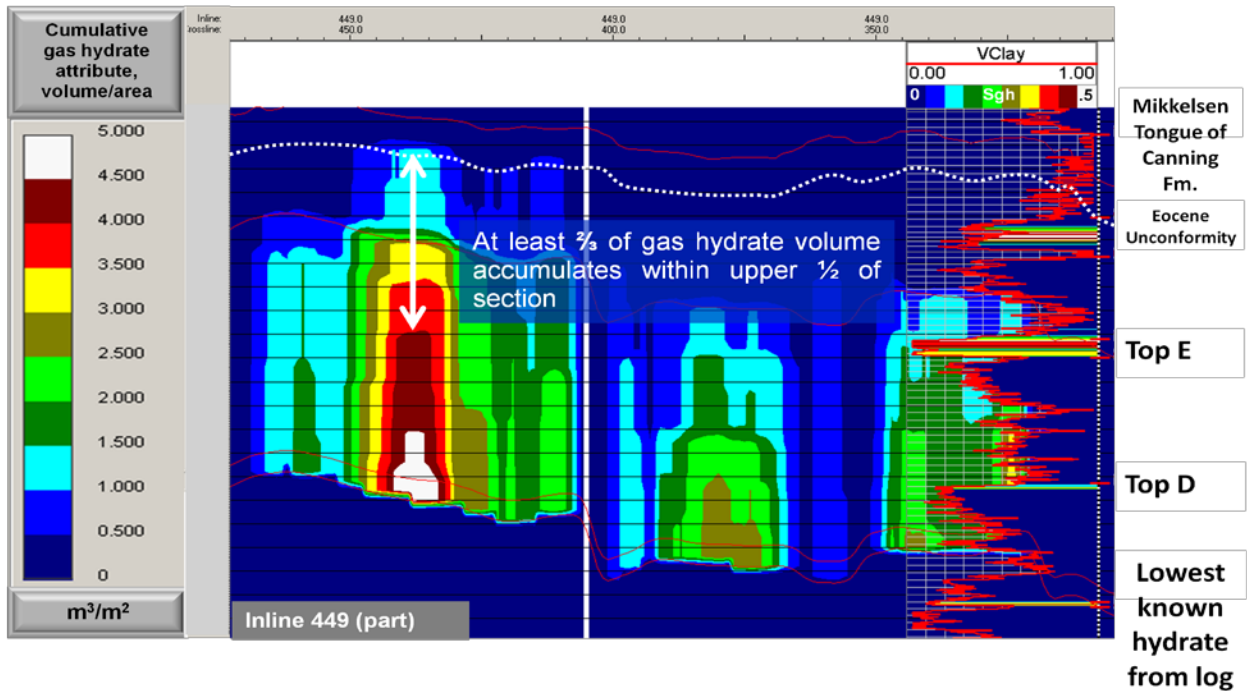


**Figure 30.** Cross-section of CATT, inline 449 (part). Due to showright restrictions no vertical scale may be shown.

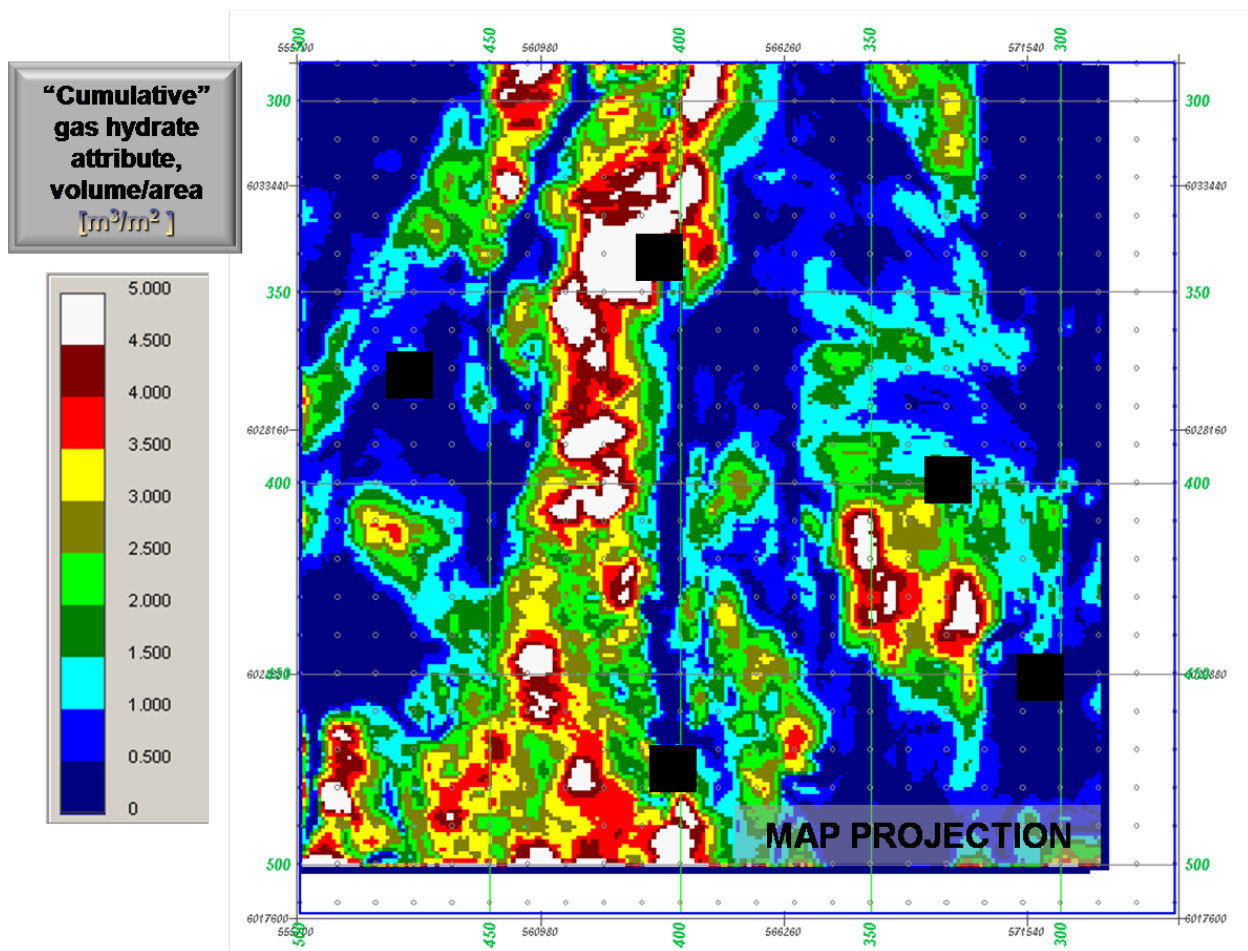


**Figure 31. Map view of cumulative gas hydrate  $[\text{m}^3/\text{m}^2]$ . Cumulative gas hydrate attribute displayed using a graduated color bar. Black squares conceal confidential location and identification information.**

Although a graduated color map of cumulative gas hydrate projects the maximum volume per area of the entire accumulated gas hydrate  $[\text{m}^3/\text{m}^2]$  (Figure 33), the genetic linkage between tectonics (graben shown in Figure 21) and depositional environment (volume-rendered paleo-river shown in Figure 28) shines through even in this categorized rendition of this cumulative attribute. Interpreted point bars and levees resonate at threshold values exceeding  $3.5 \text{ m}^3/\text{m}^2$  (red, brown, and white color fields).

	<b>Milne Point</b>
Total number of samples (traces)	44,722
Minimum attribute value	0 m <sup>3</sup> /m <sup>2</sup>
Maximum attribute value	6.34m <sup>3</sup> /m <sup>2</sup>
Average	1.51 m <sup>3</sup> /m <sup>2</sup>
Standard deviation	1.38m <sup>3</sup> /m <sup>2</sup>
TOTAL Gas Hydrate Volume w/in 3D SURVEY AREA	67,570 m <sup>3</sup>
Conversion from m3 to <u>scf</u> (X 35.31)	2,385,897 <u>scf</u>
HYDRATE TO GAS EXPANSION FACTOR 166.7	3.98 x 10 <sup>8</sup> <u>scf</u>
MINIMUM TOTAL GAS	ca. 400 BCF
BCF per km <sup>2</sup>	11.9 BCF
<b>BCF / mi<sup>2</sup></b>	<b>31.8 BCF</b>

**Table 1. GAS HYDRATE RESOURCE ESTIMATES**

\*Note: We conservatively selected an extraction horizon from near the “deepest known hydrate from logs” (USGS stratigraphic top marker designation) to eliminate potential contributions to reserve estimates from false positives. If contributions from the lower part of the section are included, the reserve total may climb, but only as much as 30%. 3-D survey area is 12.5 mi<sup>2</sup> (33.375 km<sup>2</sup>).

# Table of Contents – Part 2

<b>1.</b>	<b>Introduction .....</b>	<b>3</b>
<b>2.</b>	<b>Geophysical Well Log Analysis and Rock Physics Diagnostics.....</b>	<b>4</b>
A.	Discussion About Rock Physics Models .....	13
<b>3.</b>	<b>Seismic Data Conditioning .....</b>	<b>15</b>
A.	Spectral Balancing (SBAL) .....	16
B.	Edge-Preserving Smoothing (EPS) .....	17
B.	Phase Rotation.....	17
<b>4.</b>	<b>Well-to-Seismic Calibration .....</b>	<b>18</b>
A.	Well Tie .....	18
B.	Wavelet Analysis .....	21
<b>5.</b>	<b>Acoustic Impedance Inversion.....</b>	<b>24</b>
A.	Low Frequency Model .....	24
B.	Impedance Inversion Procedure.....	26
<b>6.</b>	<b>CATTs .....</b>	<b>32</b>
<b>7.</b>	<b>Amplitude Interpretation.....</b>	<b>37</b>
A.	Bottom-Simulating Reflector (“BSR”) .....	37
B.	BSR Reflectivity Placed Within Spatial and Temporal Context .....	37
i.	Spatial Context .....	38
ii.	Temporal Context .....	44
<b>8.</b>	<b>Attribute Analysis.....</b>	<b>46</b>
A.	BSR.....	46
B.	Hydrated Sand “A”.....	49
C.	Hydrated Sand “B”.....	50
<b>9.</b>	<b>Resource Estimates .....</b>	<b>55</b>
A.	Overview .....	55
B.	Quality Control Procedures.....	55
C.	Statistical Analysis of Resource Estimates .....	60
<b>10.</b>	<b>Discussion .....</b>	<b>61</b>
<b>11.</b>	<b>Conclusions.....</b>	<b>65</b>

<b>12. References.....</b>	<b>67</b>
<b>13. Cost Plan Status Report .....</b>	<b>70</b>

## **1. Introduction**

Part 2 of this report details the results of Phase III of DOE/NETL project DE-FC26-06NT42961. Phase I and II were carried out using onshore data from Milne Point, Alaska, whereas Phase III repeated the same workflow but using a data set from Hydrate Ridge, in relatively deep water offshore Oregon.

The overall objective of this project is to develop a new method to assess methane hydrate distribution using 3-D seismic data calibrated to wellbore data. The method was originally envisioned to be capable of detecting hydrates in multiple thin beds as well as in thick, massive beds. But as the project progressed it became apparent that the method could only quantify hydrate accumulations if those accumulations produced a seismic signature.

The project's goal is to provide a new seismic-based technology for detecting and appraising hydrate distribution and the nature of the associated geologic sediments and structures. By integrating geology, 3-D seismic, well logs, and rock physics, we hope to accurately assess the volume of gas hydrate over broad regions. The major advantage of this method is that it uses conventional 3-D seismic and well log data as inputs. No special tools or acquisition methods are needed; hence, the method will be economical and practical to apply.

The method is based on the computation of cumulative seismic attributes (CATTs) and their calibration to in-situ data from well logs and/or core measurements. CATTs are fundamentally different from other seismic reservoir characterization methods, such as amplitude-versus-offset and acoustic impedance inversion. They are designed to respond to multiple stacked layers of hydrocarbon-filled zones, and unlike most seismic attributes, they are well-suited to calibration with well log data.

## 2. Geophysical Well Log Analysis and Rock Physics Diagnostics

During Ocean Drilling Program (ODP) Leg 204, a suite of elastic logs were recorded in six drill holes. These boreholes penetrated the gas hydrate stability zone on the southern part of Hydrate Ridge, offshore Oregon (Figure 1). Wireline logs were measured in Hole 1244E, Hole 1245E, Hole 1247B, Hole 1250F, Hole 1251H, and Hole 1252A.

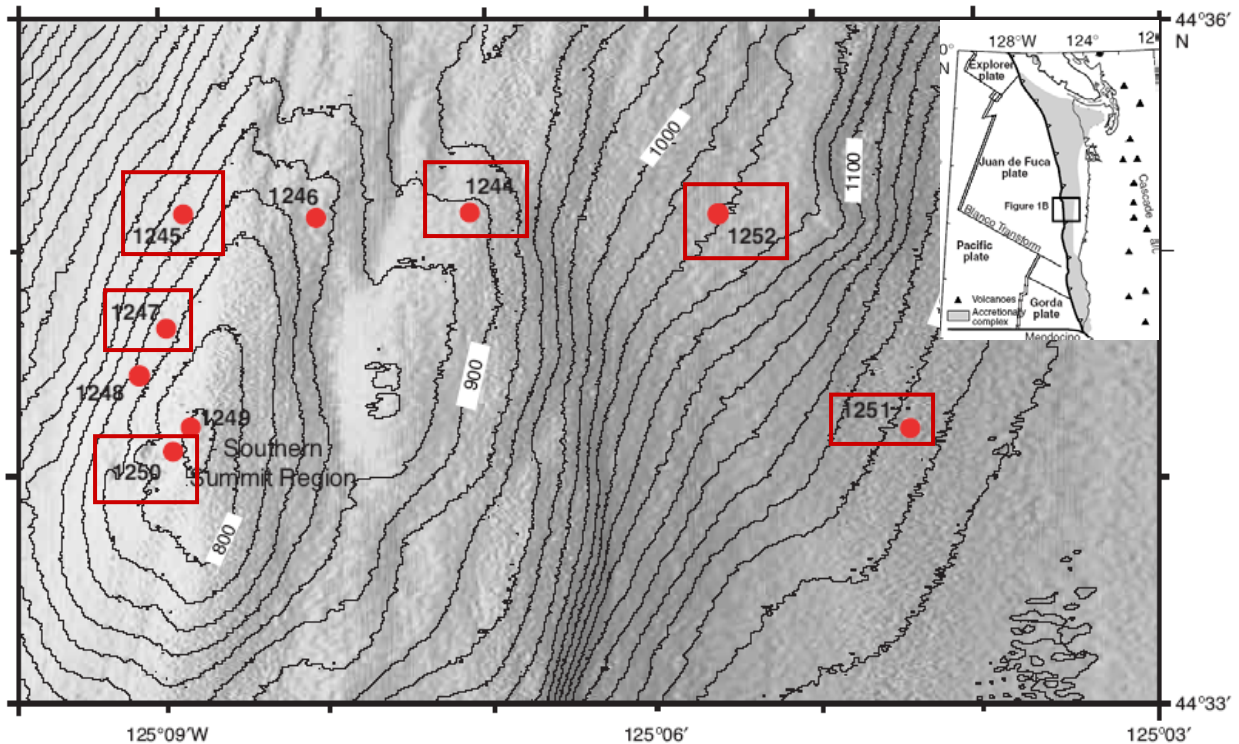


**Figure 1. Location of Hydrate Ridge and of the six wells (red boxes) used in this study. Modified from Tréhu et al., 2003, chapter 1, figure 1.**

Geophysical Well Log Analysis (GWLA, the first step in our well log editing process) involves editing logs from shallow-looking tools (sonic and density), derivation of lithology, porosity, and fluid saturation logs (Figure 2), followed by the generation of acoustically important curves (acoustic impedance and shear impedance) and combination logs such as  $V_p/V_s$  and Poisson's ratio (Figures 4 and 5).

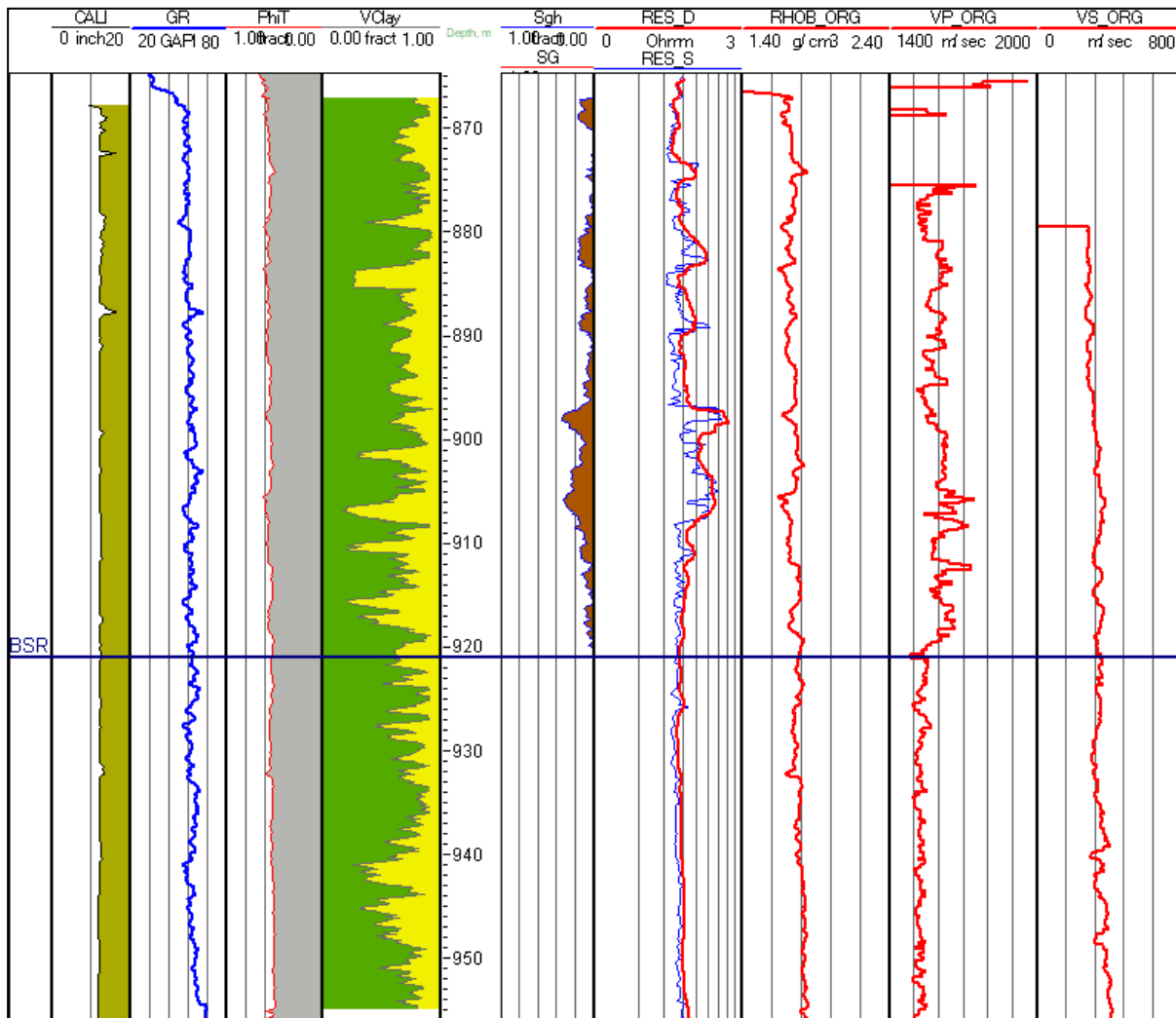


**Figure 2. Measured wireline logging data (red curves) from Hole 1250F along with petrophysically-derived curves from Geophysical Well Log Analysis (total porosity, volume clay, and hydrate saturation). Hydrate saturation is based on resistivity response. Note that Vp in general is higher in the hydrate stability zone but does not correspond to hydrate saturation. Therefore, there appears to be a disconnect between resistivity and Vp.**

Hydrate Ridge wells required a significant amount of editing during the GWLA process. The wells were initially edited for simple washouts over the entire logged interval of the well. This “simple” de-spiking procedure removed large deflections in the magnitude of the well data. Later, the wells were analyzed for lithology (relative proportions of mineral constituents). This was accomplished using the gamma ray log, neutron-density log, and core descriptions. Volumetric curves for gas hydrates and free gas were also calculated. Water saturation calculations utilized the Archie empirical relationship (Archie, 1942). The Archie parameters

used were:  $a = 1$ ,  $m = 1.3$ ,  $n = 2$ , and the value for formation water resistivity was determined for each well using a Pickett plot.

The typical log response of gas hydrate-bearing sediments is an increase in velocity and resistivity. This behavior has been seen in different well data sets around the world, for example in the Arctic Mallik, Northern Canada, and Blake Ridge in the Atlantic. However, in the Hydrate Ridge data set measured velocities associated with sediments containing gas hydrates do not exhibit this behavior (Figures 2 and 4), possibly indicating that to some extent the quality of the elastic curves is compromised (although other explanations may be possible). Therefore, in this study forward modeling based on the “soft-sand” theoretical model of Dvorkin et al (1999, 2003) was applied to predict the elastic properties of sediments with gas hydrates and wet sediments. The soft-sand model is based on the contact Hertz-Mindlin contact theory to calculate the effective moduli of a random pack of elastic spheres at different porosities using the modified Hashin-Shtrikman lower bound. After the solid moduli are calculated, the effect of the fluids is introduced by using Gassmann’s equation.

The soft sand model assumes that sediments are unconsolidated and contain any number of solid constituents. In our case, sediments at Hydrate Ridge contain sand, silt, and clay, as well as gas hydrates as part of the load-bearing matrix. Thus, gas hydrates fill the pore space and reduce porosity, and their rigidity increases the elastic moduli of the solid frame. The net effect is an increase in P- and S-wave velocity and thus impedance.

In our evaluation of log quality in Hydrate Ridge, we felt that the density log was reasonably accurate in its measurement of in-situ conditions. This determination was based on the agreement of density measurements obtained from different logging runs and with core density measurements. Figure 3 is an example of the good match between the wireline density log, LWD density log, and core measurements in Hole 1244 A and Hole 1244E. These two holes are located in close proximity to each other and penetrate similar lithology. Thus, based on what we felt were accurate density logs, P- and S-wave velocities were generated using the soft-sand model. The elastic values that we used for the various components are listed in Table 1. The elastic moduli and density for gas hydrates are from Helgerud (2001) while the mineral properties are from Mavko et al (2003).

Component	Density (g/cc)	Bulk Modulus (GPa)	Shear Modulus (GPa)
Gas Hydrate	0.910	7.40	3.30
Quartz	2.650	36.60	45.00
Clay	2.580	21.00	7.00
Calcite	2.710	76.80	32.00

Table 1. Density and elastic moduli of the matrix used for modeling.

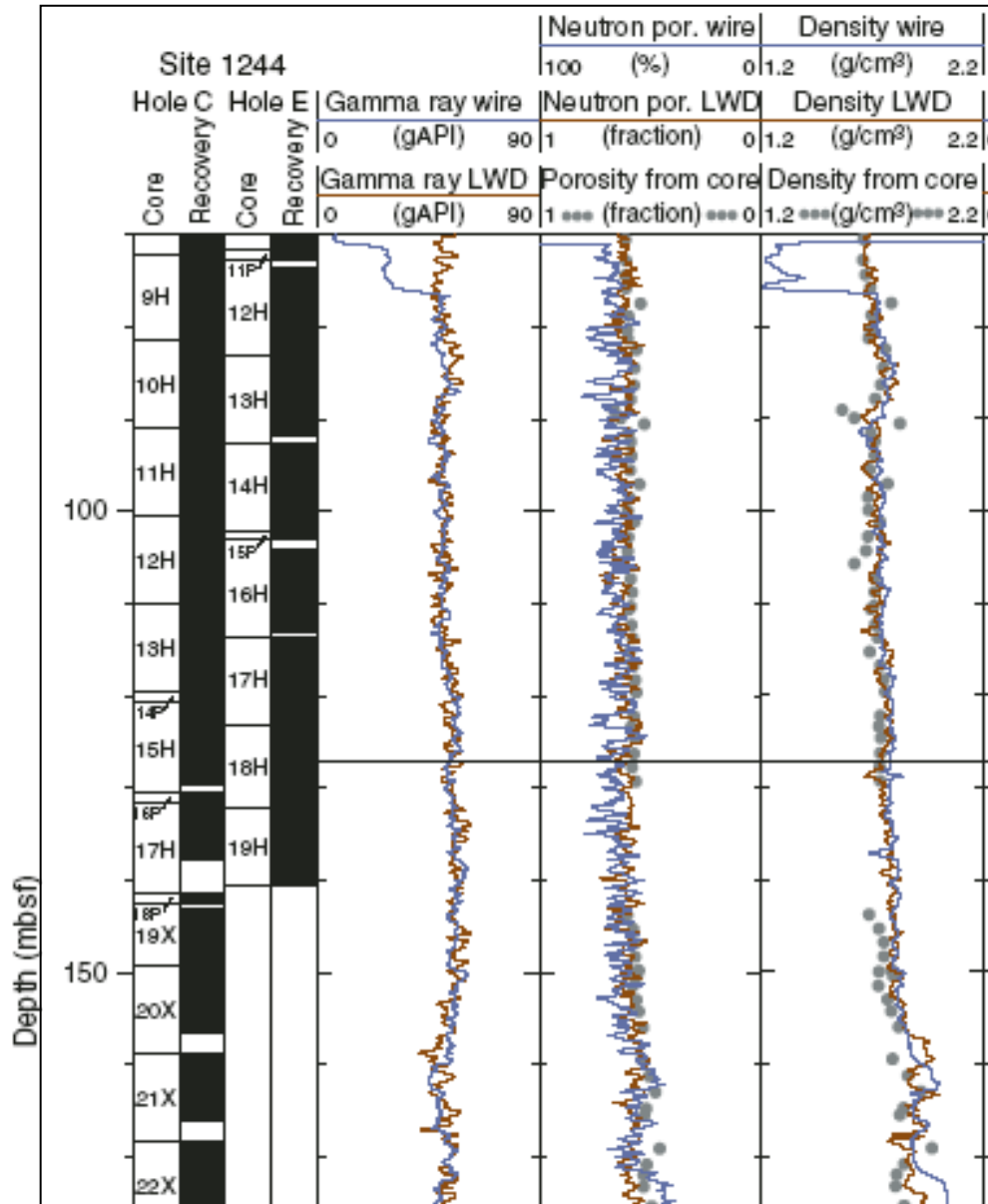
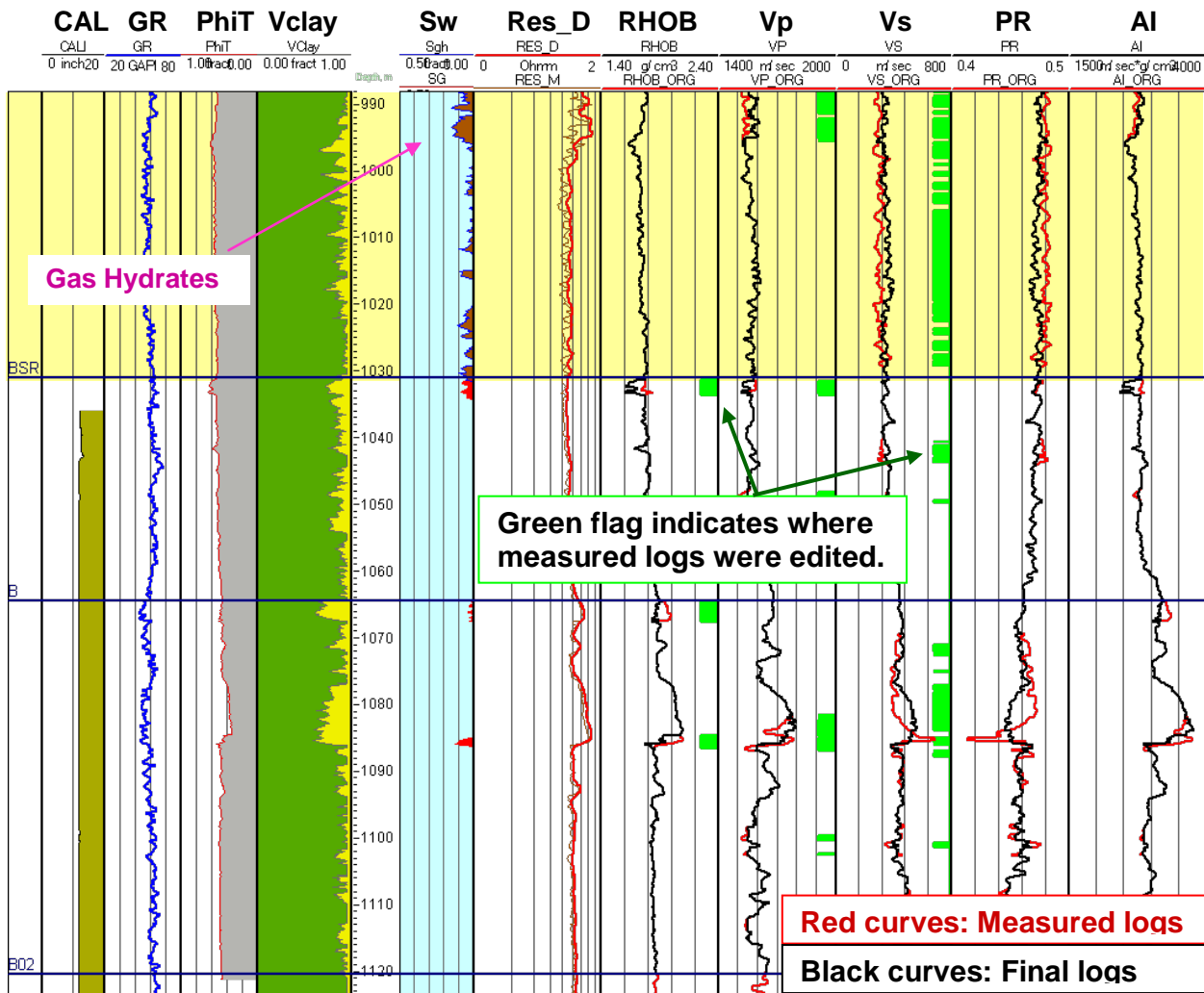
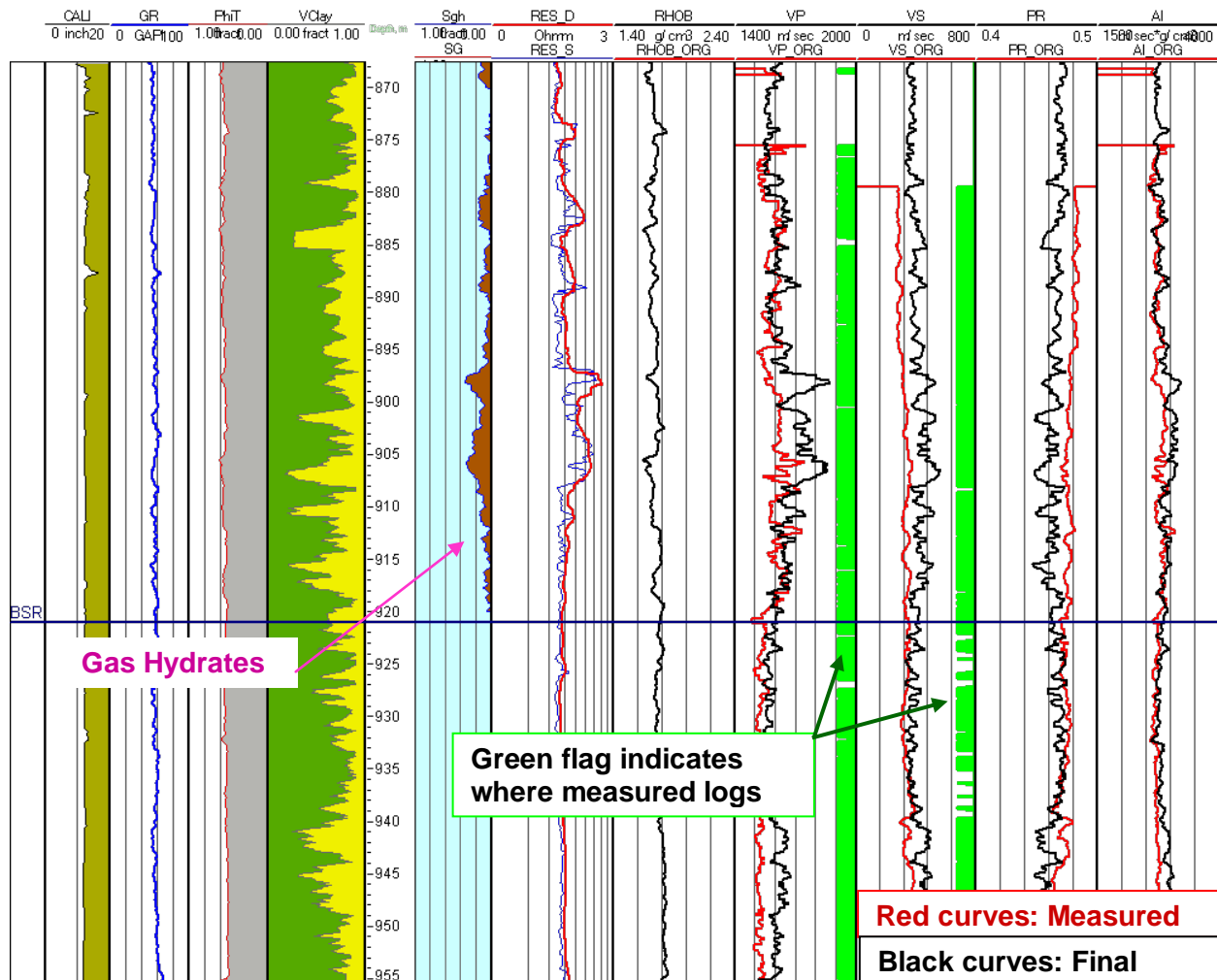


Figure 3. Comparison of density measurements from logging while drilling (LWD), wireline logging, and from core density in Hole 1244A and Hole 1244E. From Tréhu et al., 2003, chapter 3, figure 43.

The final elastic and density curves are combination of measured and modeled data. The measured data was kept as much as possible. In well 1244E the modeled velocities mostly matched the recorded velocities, and thus resulted in a high confidence level in the measured logs for this well (Figure 4). Note that the hydrate concentration is mostly low in the hydrate stability zone and the elastic logs don't appear to react to the presence of hydrates, even at the top of the well where the hydrate saturation exceeds 20%. Well 1250F is an example of a well that has high concentrations of gas hydrates (over 30% in some intervals) but whose velocity logs also do not show the classic hydrate signature (Figure 5). Note that the lack of correspondence between the logs and model extends the length of the well, so it is not merely an issue with the presumed behavior of hydrates in the hydrate stability zone.



**Figure 4. Measured Wireline logging data (red curves) and final log data (black curves) from Hole 1244E. Green flags indicate where measured data were replaced by modelled data. Note the good correspondence between modelled and measured elastic curves.**



**Figure 5. Measured Wireline logging data (red curves) and final log data (black curves) from Hole 1250F. Green flags indicate where measured data were replaced by modelled data. Note the poor correspondence between modelled and measured elastic curves.**

Rock physics modeling shows that sediments with less than 20% gas hydrate saturation cannot be discriminated from sediments that do not contain gas hydrates. However, sediments with more than 20% gas hydrate saturation may be distinguishable. This can be seen in Figures 6, 7, and 8, which are 3 different rock physics cross-plots. In each of these figures, sediments with less than 20% gas hydrates fall below the 100% quartz line, together with wet sediments. However, sediments with more than 20% gas hydrate saturation show higher P-wave velocities than wet sediments and plot above of the 100% quartz line.

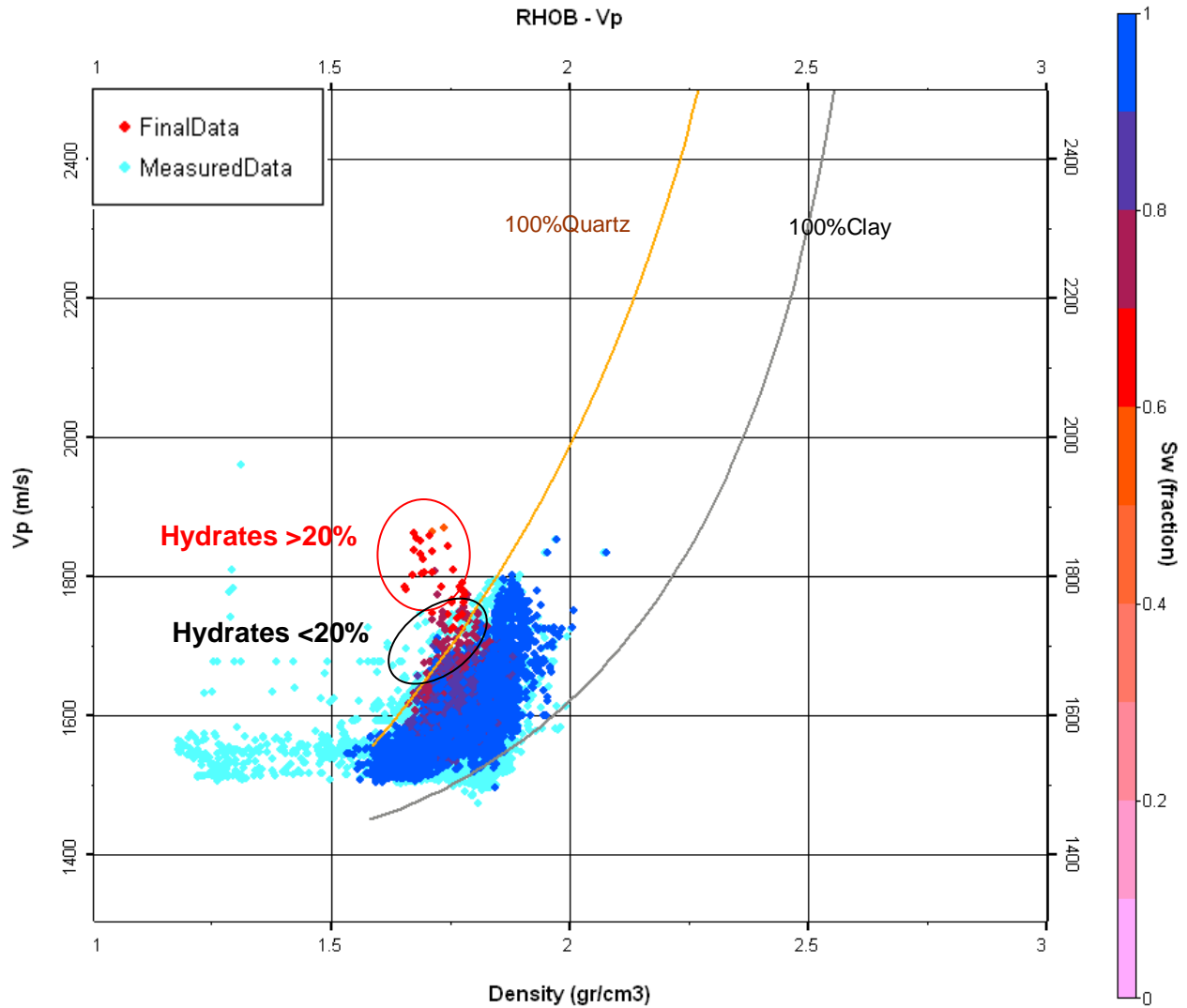


**Figure 6. Density vs. P-wave velocity crossplot color-coded by water saturation for all 6 wells used in this study. Sediments with gas hydrate saturation higher than 20% plot above 100% quartz line and thus can be uniquely identified. Sediments with hydrate saturations less than 20% crossplot over or in close proximity to wet sediments, and thus cannot be uniquely discriminated.**

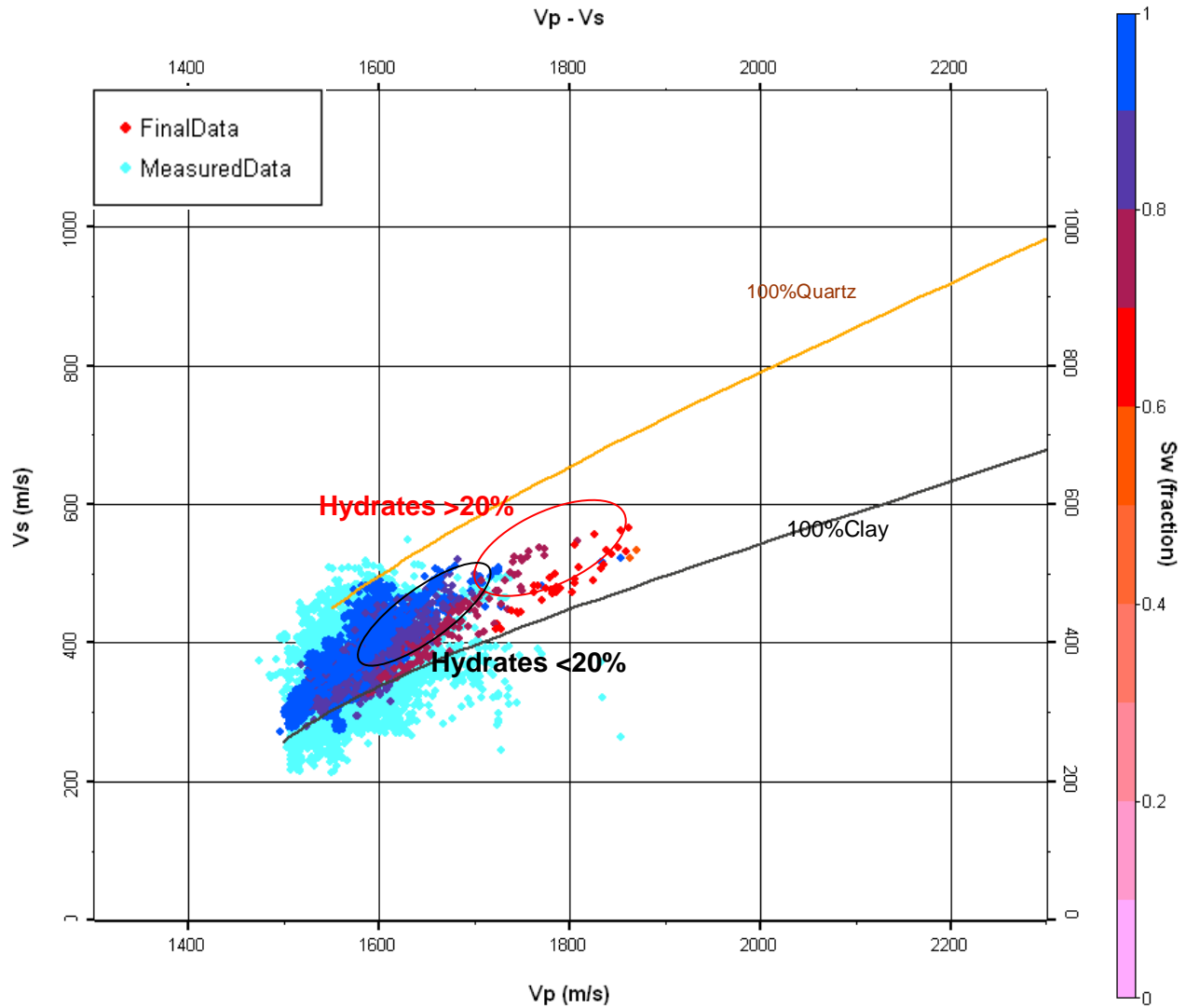


**Figure 7. P- vs. S-wave velocity cross-plot color-coded by water saturation for all 6 wells used in this study. Sediments with gas hydrate saturation higher than 20% have higher compressional velocities and thus can be uniquely identified. Sediments with hydrate saturations less than 20% cross-plot over or in close proximity to wet sediments, and thus cannot be uniquely discriminated.**

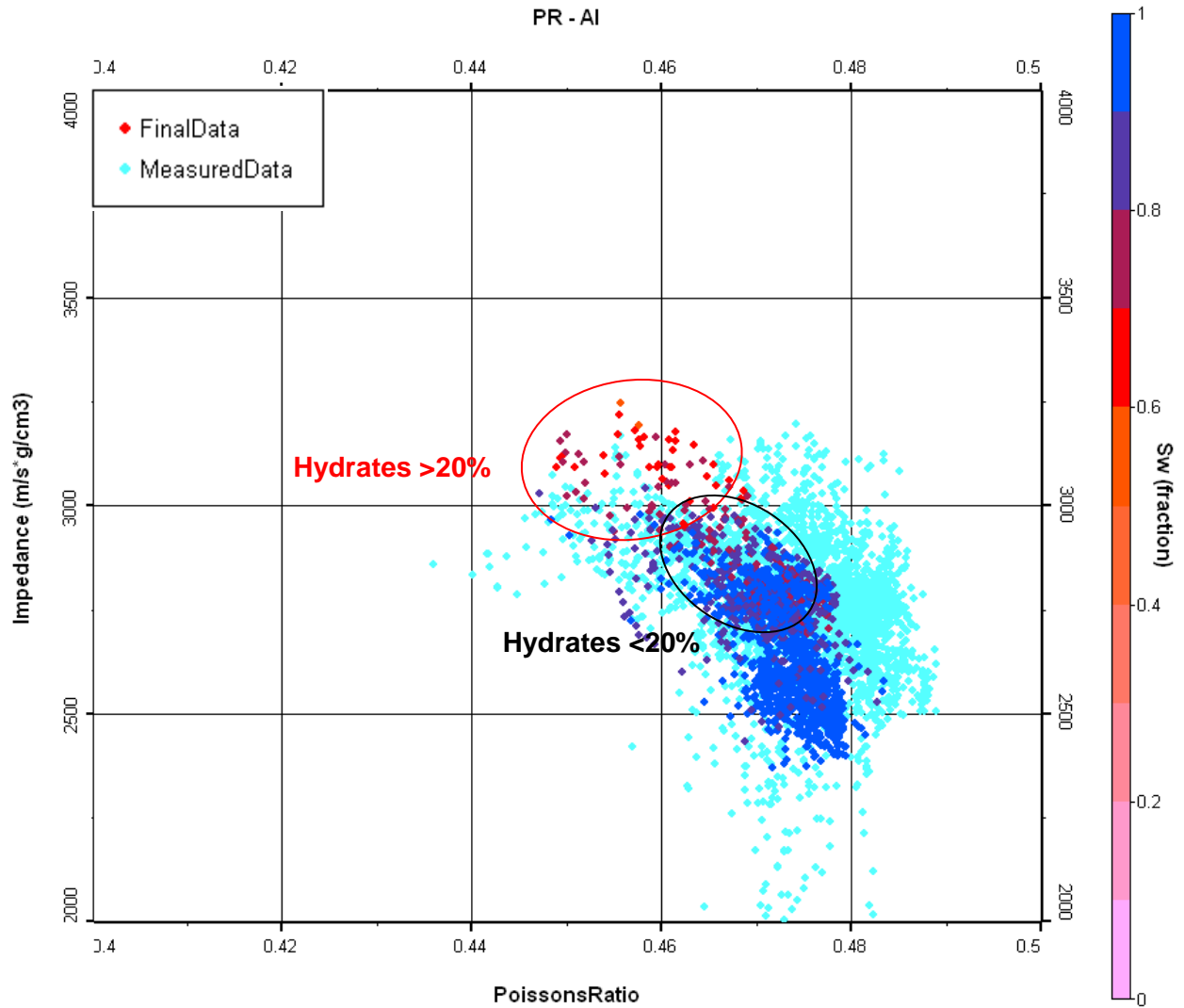


**Figure 8. Poisson's ratio vs. P-wave impedance crossplot color-coded by water saturation for all 6 wells used in this study. Sediments with gas hydrate saturation higher than 20% have higher compressional velocity (and thus acoustic impedance) and thus can be uniquely identified. Sediments with hydrate saturations less than 20% cross-plot over or in close proximity to wet sediments, and thus cannot be uniquely discriminated.**

## ***A. Discussion About Rock Physics Models***

Different studies of gas hydrates worldwide indicate that both P- and S-wave velocities increase with increasing gas hydrate saturation. Several rock physics models have been employed in order to quantify this effect. Two of them are the “soft-sand” model and Walton’s model.

The “soft-sand” model of Dvorkin et al (1999, 2003) is based on the Hertz-Mindlin contact theory and links elastic wave velocities, porosity, fluid compressibility, mineralogy, and effective pressure of unconsolidated sediments. Gas hydrates are considered as part of the matrix, decreasing porosity and subsequently increasing the frame matrix moduli. On the other hand, Sava and Hardage (2006) propose the same approach treating the gas hydrate as part of the frame but instead of Hertz-Mindlin theory, they use the Walton’s smooth model. Walton’s model describes unconsolidated sediments at low effective pressures where normal and shear deformation occur simultaneously.

In this study, these two rock physics models were compared using the same physical parameters. Acoustic properties predicted by these models are very close to each other and to reliable measured data in the upper portions of the well bores. Walton’s smooth model underpredicts the elastic properties in intervals where sediments are more consolidated, such as in the harder sands below the base of the hydrate stability zone. For that reason the “soft-sand” model was used to model the Hydrate Ridge data. This model has been used successfully for modeling sediments with gas hydrates in other parts of the world, for example in Milne Point, Alaska (DE-FC26-06NT42961 – Phase II).

Another approach was taken by Lee and Collett (2006). They estimated the amount of gas hydrates in sediments using the modified Biot-Gassmann theory (BGTL) on shear-wave velocity logs. They then estimated free gas saturations using the standard Biot-Gassmann theory (BGT) on P-wave velocity logs with the Gassmann coefficients determined using BGTL. This methodology was adopted because the authors noted the same phenomenon as the current study – namely that the P-wave velocities in several of the boreholes were low for sediments containing hydrates. They suggest that the low P-wave velocities coupled with normal S-wave velocities might be caused by the existence of free gas. We note that it is theoretically possible to have free gas in the hydrate stability zone, as evidenced by an expulsion vent just to the west of borehole 1250 where gas is bubbling to the surface (this is discussed later in this report). It is

also possible that if free gas is present, it is the result of hydrates becoming disassociated during the drilling process.

During the current study, we ran modeling tests assuming 3% free gas was occurring simultaneously with the hydrates. We noted that it did reduce P-wave velocities as expected, but in most boreholes we did not need to call upon such an assumption to match P-wave velocities with S-wave velocities. In boreholes 1245E and 1250F (Figure 5) both Vp and Vs were low and were replaced; borehole 1247B required a slight increase in Vs with no changes in the trendline of the Vp log (although the log was noisy and was replaced with the modeled log); and borehole 1244E (Figure 4) had accurate Vp but low Vs until the very top of the log where the hydrate saturation exceeded 15% and the Vp was low but the Vs was mostly accurate (just as Lee and Collett report).

Instead of taking the Lee and Collett approach, our basic assumption is that we need to first verify the fidelity of the velocity and density logs before calling upon other explanations for their behavior. Density log quality was discussed earlier in this report and is generally of high quality. We then investigated the slowness-time coherence analyses to assess the quality of the velocity logs and found that the coherency signatures were quite scattered in some wells (particularly in borehole 1250, Figure 5) but stable in others (Guerin, et al, 2006). In fact, we noted a good correlation between low coherency log intervals and modeled-log-replaced sections. This situation was acknowledged in the ODP Initial Reports for Leg 204 (Tréhu et al., 2003, chapter 9, p. 25):

“The recorded sonic waveforms from both lowerings of the DSI are of very high quality, but the very low velocity of the formation made it difficult for the automatic slowness/time coherence (STC) picking program to select accurate compressional velocities. Some adjustment of the STC parameters allowed for improved compressional velocity but further reprocessing is required. The quality of the recorded shear wave data was very high, but it also will require additional processing.”

With this knowledge, we feel that modeling of the velocity logs was needed and replacement of log intervals that do not match the model was justified.

### 3. Seismic Data Conditioning

The Hydrate Ridge seismic survey was a multichannel 3D acquired on the continental slope offshore Oregon (USA) during the summer of 2000 and covered an area of 48 Km<sup>2</sup>. The inline by cross-line spacing is 12.5m x 25m. A low cut filter (15-25Hz) was applied by the processor (the University of Texas) to remove noise resulting from choppy seas and large swells. Velocity analysis was performed each 10<sup>th</sup> line and every 100<sup>th</sup> common midpoint. After NMO corrections were applied, 3D post-stack Kirchhoff migration was performed (Chevallier, et al, 2006). The frequency content ranges from 10 to 220 Hz with the dominant frequency being centered at 150Hz.

The resulting data volume has high resolution and reasonably good fidelity; however, time shifts between inlines considerably degrade the data coherency in the crossline direction. This is the result of “static effects due to tidal changes in water depth, swell, and changes in the towing depth of the streamer and/or GI guns” (Chevallier, et al, 2006). Not tracking these effects during acquisition and then removing them during processing is a fatal flaw in this data set that likely is unrecoverable at this stage. The resultant time lags between adjacent inlines are not simple static shifts, but are dynamic and change with depth (due to raypath changes) and with CDP (due to all other statics problems).

In order to improve the image quality in the inline direction (since nothing can be done in the crossline direction), the data was conditioned to improve the signal to noise ratio. The workflow used to enhance the input post-stack migration is described below (Figure 9):

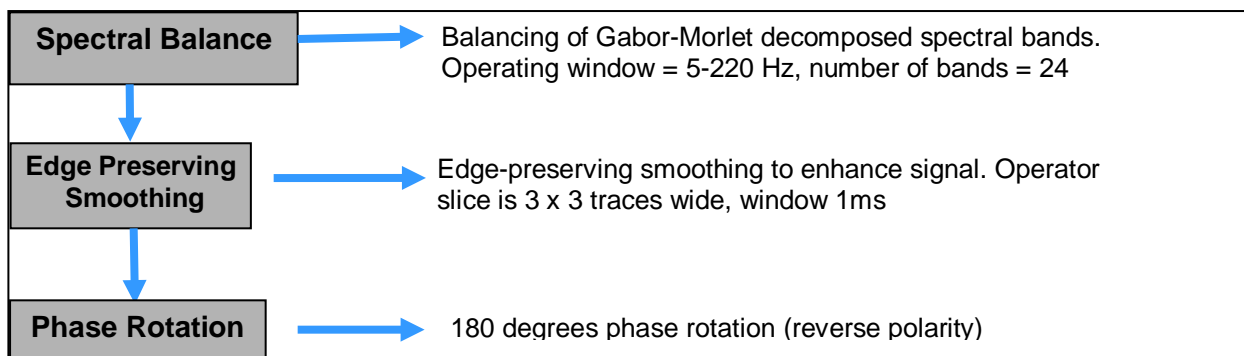


**Figure 9. Workflow used for post-stack seismic data conditioning of the Hydrate Ridge 3-D seismic data.**

## A. Spectral Balancing (SBAL)

Spectral Balancing (SBAL) uses the Gabor-Morlet transform in a Joint Time Frequency Analysis (JFTA) to decompose the data into a user-defined number of sub-bands and adjust their amplitudes according to the trace envelope. Each sub-band is scaled accordingly before summing the sub-bands, maintaining the total energy within the trace envelope and preserving the original trace amplitude profile.

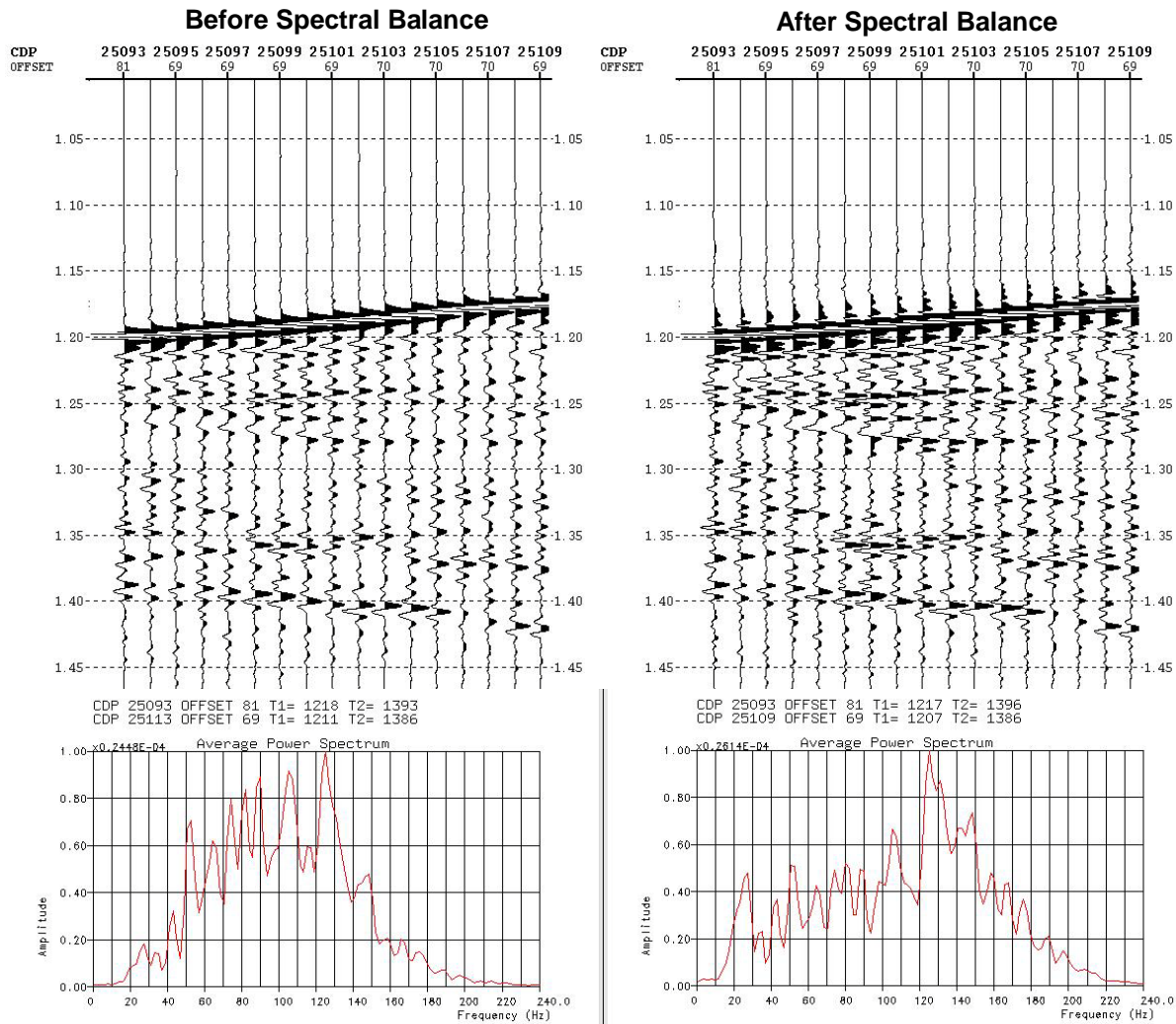


**Figure 10. Shows the application of spectral balance in a section through the 1250F location. Below of each section are amplitude spectra before and after the application of spectral balance.**

The parameters used in this process were defining the potential bandwidth to be 5-220Hz and subdividing this bandwidth into 24 sub-bands. This process seeks to enhance the frequency

bandwidth, but does so by balancing the spectrum without altering the original amplitudes. Quality control plots show that the bandwidth has been enhanced at low frequencies between 20-60Hz, and at high frequencies between 140-180Hz (Figure 10).

### ***B. Edge-Preserving Smoothing (EPS)***

Edge-Preserving Smoothing (EPS) is a signal enhancement procedure that removes random noise but preserves discontinuities in the data while doing so. The method is based on a correlation computation between traces in a neighborhood (3x3), and uses them as weighted averages summing those above of a certain similarity threshold (here a cross-correlation above 0.25). The operation estimates the gradient or curvature attribute, which is perpendicular to the possible edge. This information allows local calculation of the structural dip, which determines the trace samples to be summed along individual reflectors.

The result is a general clean-up or S/N enhancement of the data, with incoherent noise being removed without affecting geological boundaries or reflector amplitude (Figure 11). Reflectors in the conditioned data become cleaner and laterally more continuous, thus facilitating a more accurate horizon interpretation.

### ***B. Phase Rotation***

Finally, a phase rotation of 180° was applied to the seismic data so that it conforms to our standard polarity convention wherein an increase of acoustic impedance is represented by a peak in the seismic. This step did not change the data fidelity and was only done for cosmetic purposes only.

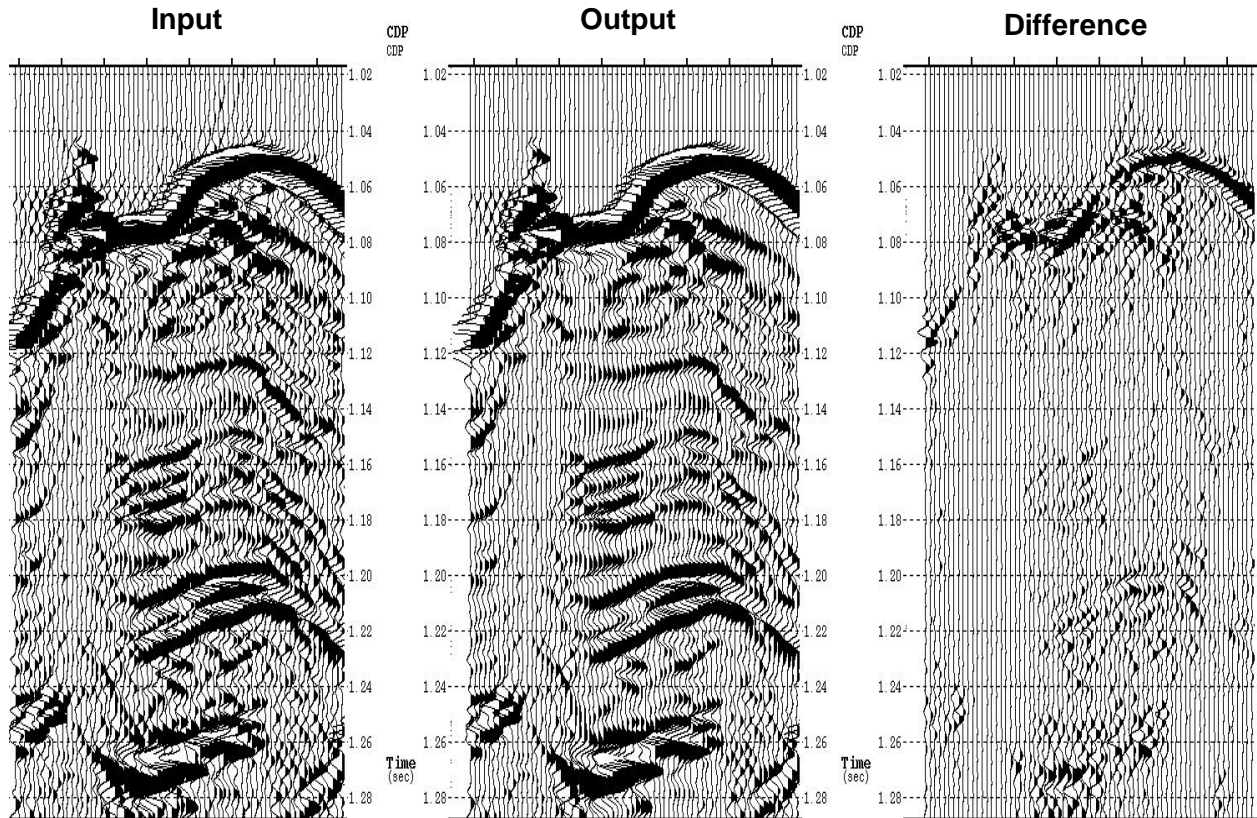


**Figure 11. Inline through site 1250F (inline 250) from left to right: Input post-stack, the application of the EPS procedure, and the difference between the two panels.**

## 4. Well-to-Seismic Calibration

### A. Well Tie

In order to tie the well logs to the seismic, normal incident synthetic seismograms were created using acoustic impedance logs and a wavelet extracted from the seismic (see Section 5b). Synthetics were generated using logs modeled with the “soft-sand” model and then upscaled by Backus averaging (see Section 3). All 6 wells were used in this process, although only those with the highest correlation were used to derive a composite wavelet for the inversion (Section 5b).

Initial positioning of well synthetics in the seismic volume was achieved using three VSP checkshots that were run during the well program (1244E, 1247B, and 1245E). However, well ties from those three checkshots were not satisfactory, including one (well 1245E) that was not

on the same depth trend as the others (Figure 12, left). Therefore, although the other two checkshots (1244E and 1247B) were used as guides, the primary time-depth relationships were derived using the P-wave sonic. The process used is described below. During the tie procedure, a necessary QC is a plot showing all time-depth pairs along with the two good checkshots (Figure 12, right). This QC demonstrates that all final time-depth relationships share a common time-depth trend with the exception of well 1251 which was located in the basin southeast of the others wells (Figure 1).

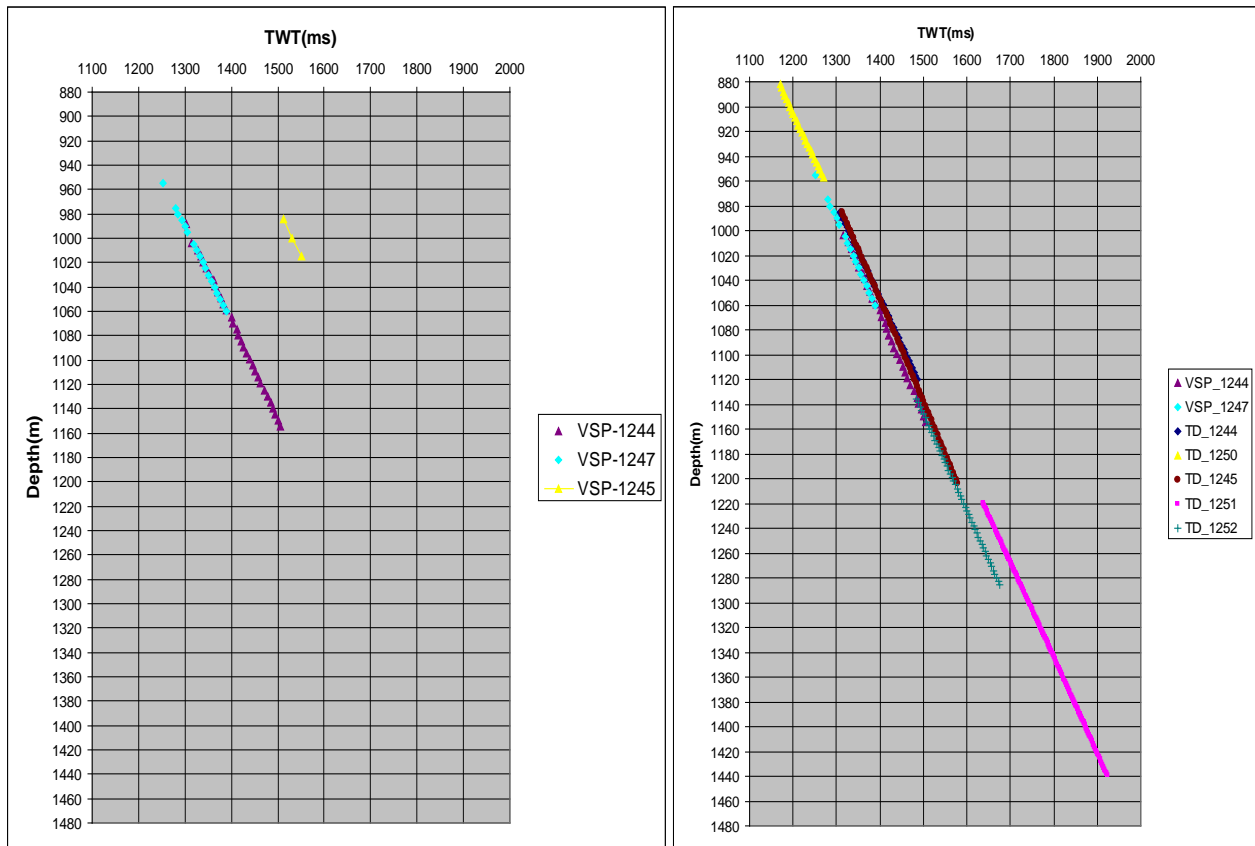


**Figure 12: Original checkshots from VSP (left) and final time depth relationships for each of the sites compared with two original checkshots (right).**

The process of using  $V_p$  logs to tie wells to seismic involved first selecting the main seismic reflectors as anchor points, which in most wells was the seafloor and BSR but occasionally included one or more high amplitude sand reflectors. Because none of the wireline velocity or density logs extended to the seafloor, these logs were extrapolated using the “soft-sand” model in conjunction with any other information that was available, such as core descriptions, LWD

logs, and information from the closest holes if that was of assistance. After the tie was anchored at the water bottom, the other primary reflector(s) were then tied, stretching or squeezing the Vp time-depth relationship if needed to bring the other reflectors in line (Figure 13). As part of the iterative well tie process, a wavelet was extracted from a user-specified window and used as a QC (Figure 13, inset).

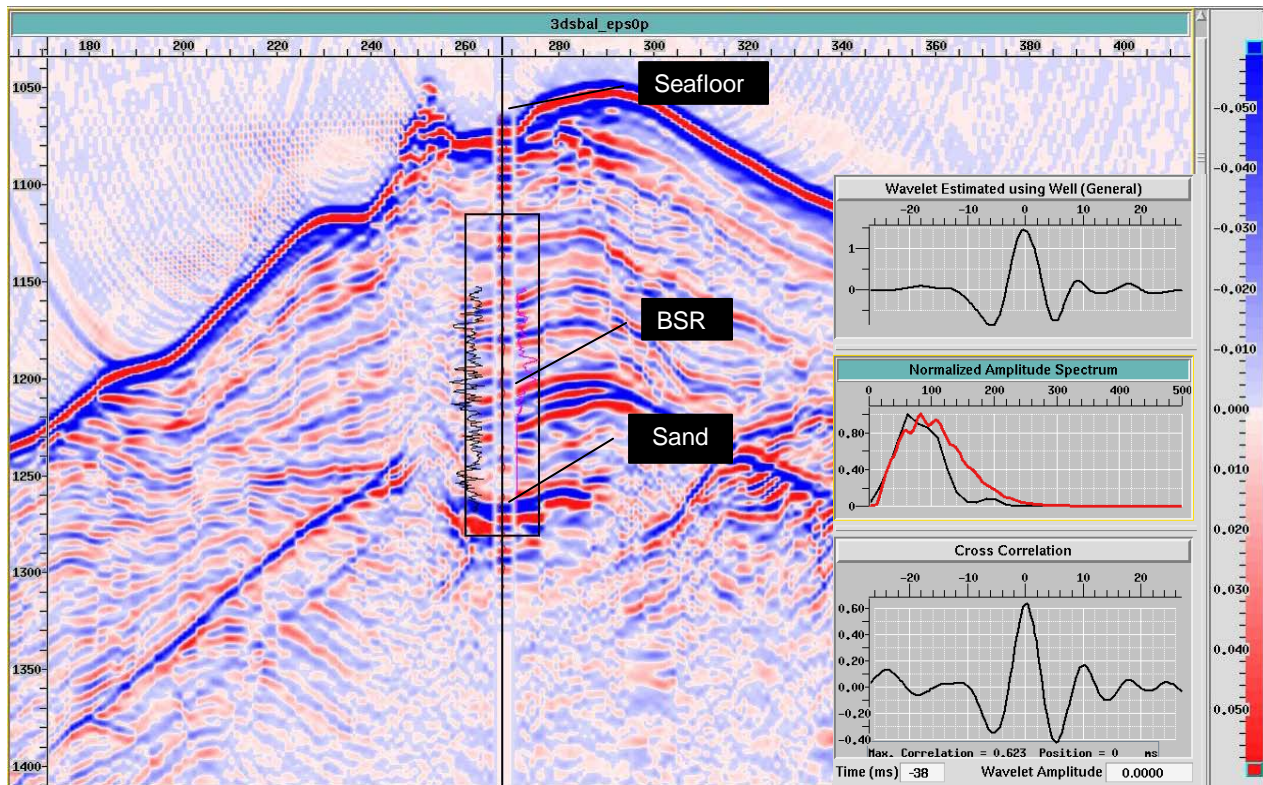


**Figure 13. Synthetic seismogram overlaying the seismic trace at well 1250. Logs shown are volume of shale (black) and water saturation (magenta). Black box indicates the wavelet extraction window. At right (inset) are shown the extracted wavelet, spectral analysis, and cross-correlation plots. The red spectral curve represents the seismic spectra within the black box on the seismic section.**

Quality control plots were used to check the velocity changes that bulk shift and stretch/squeeze may have introduced. In the case of well 1250 (Figure 13), the QC plots (Figure 14) show a velocity decrease of 20m/s as a result of stretch being applied (Track 2) causing the synthetic to extend lower in time (Track 3 red curve). The time and velocity drift curves (Tracks 4 and 5) show that velocity changes were achieved by a stretch between 890m and 910m.

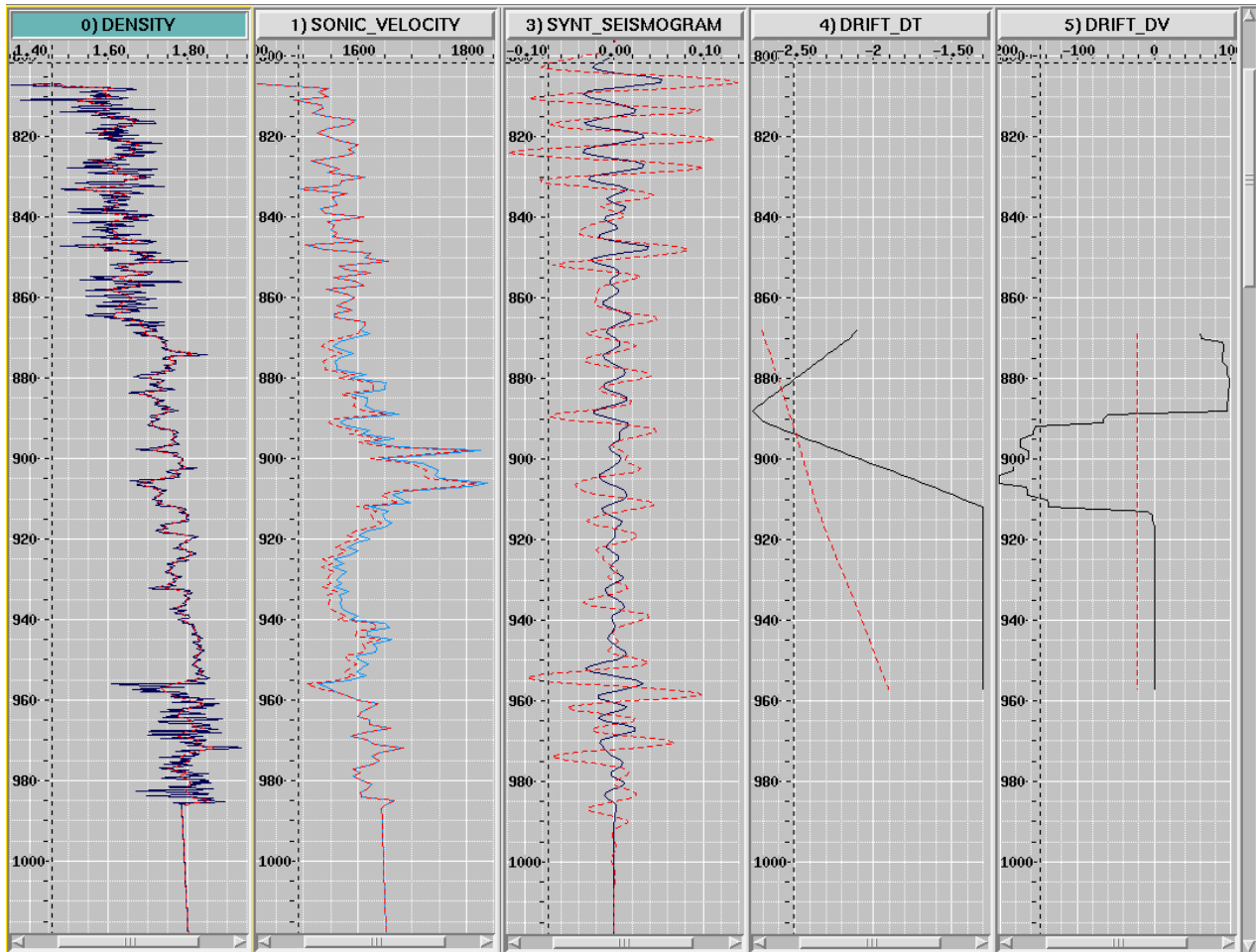


**Figure 14.** Changes due stretch and squeeze in well 1250. The density log (in g/cc) on track 1 is not affected by these changes (the Backus-averaged log is in red). Track 2 shows the velocity logs (m/s) before (light blue), and with the application of the drift curve (red). Track 3 shows synthetic traces, tracks four and five show drift curves in time and velocity. The final curves are the red dotted curves in all tracks.

## B. Wavelet Analysis

Wavelet extraction assumes the convolutional model, which states that the seismic trace is basically a convolution of the earth's reflectivity with a seismic source function (wavelet) plus added noise. In an ideal situation the noise component is near zero and it becomes easier to identify the seismic wavelet using seismic traces around the well and Backus-averaged acoustic impedance logs.

The quality of the well-tie, and consequently that of the wavelet, is evaluated by a cross-correlation between seismic traces and a synthetic trace produced by the Backus-averaged AI

log convolved with a user-specified wavelet. In the six Hydrate Ridge wells, correlation coefficients range between 0.5-0.7 (Table 1). For reference, a correlation coefficient of 0.5 means that an equal number of reflectors tied as did not tie. This is considered on the low end of what is normally acceptable. In this study, however, a number of key assumptions were made with regard to the validity (or lack thereof) of the wireline well logs and to the rock physics models governing this depositional environment (Section 3). For example, well 1250 appears to show an accurate tie except in the area at and immediately below the BSR (Figure 12), suggesting that the final well logs do not show enough of a velocity change at this boundary. Inspection of the original Vp log shows that it does in fact have a significant velocity reduction at this boundary (Figure 5), leading to questions about the validity of the model in that zone.

<b>Well</b>	<b>Correlation Coefficient</b>	<b>Time Windows (ms)</b>
1250F	0.62	1120-1270
1247B	0.51	1180-1330
1245E	0.63	1310-1420
1244E	0.70	1300-1400
1252A	0.58	1510-1620
1251H	0.53	1790-1940

**Table 2. Well tie correlation coefficients and extraction windows for each well used in this study. Wells are ordered clockwise from the summit in the southwest portion of the survey area.**

We computed a composite wavelet using a module developed at Rock Solid Images. The composite wavelet is calculated in the frequency domain. It uses a weighted-averaging process based on the correlation coefficient calculated during the wavelet extraction. Thus, wavelets from poorer well ties have less influence on the estimated composite than those from better well ties. In order to average the phase, it is unwrapped to make sure all wavelets are consistent. To determine the average phase of the composite wavelet, linear regression is performed. The intercept of this regression represents the average phase and the slope indicates the wavelet time shift. The lower and upper frequency limits used for the regression are chosen so that the calculation is only performed within the main energy band of the wavelet.

We obtained a composite wavelet using only the three most stable wavelets in the project area (Figure 15). These three wavelets are from wells 1244, 1245, and 1250, all of which have correlations greater than 0.60 (Table 1). The resulting composite wavelet has the desired characteristics of a large central lobe of energy combined with much reduced reverberations on the tails of the wavelet (as compared to the original input wavelets), indicating that noise cancellation has occurred as we would expect. The average phase of this wavelet is approximately zero (the phase regression gives a value of  $4.2^\circ$ ).

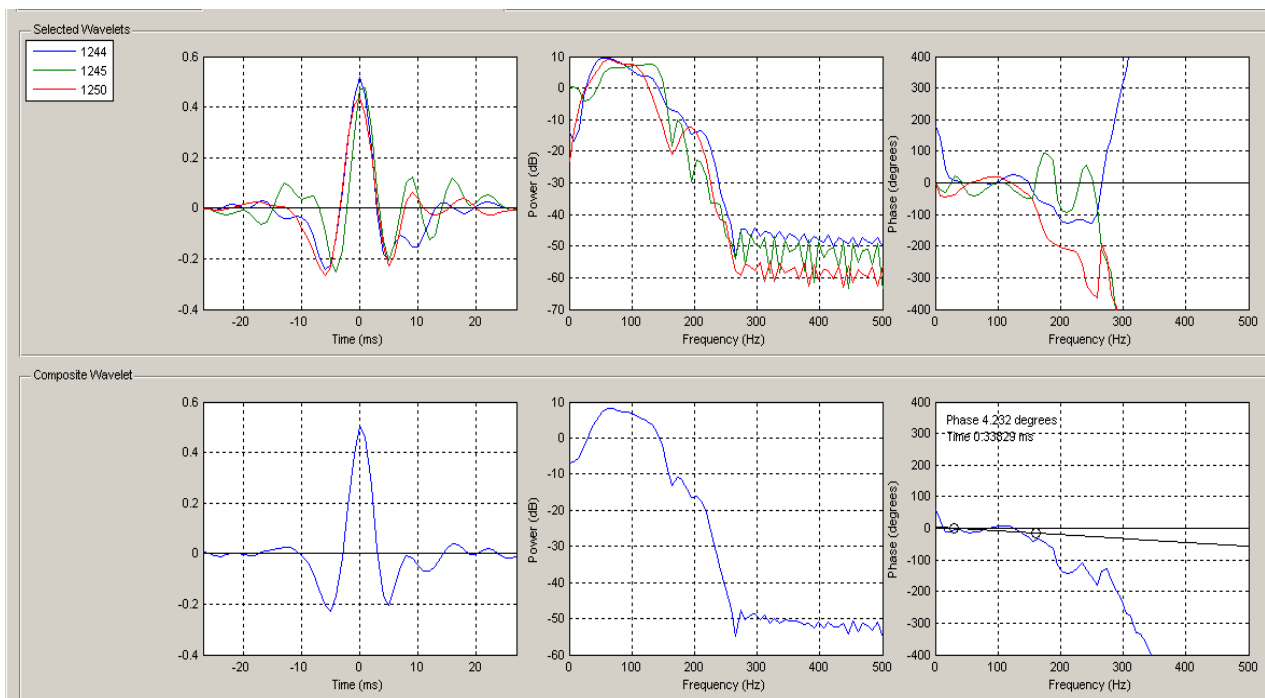


**Figure 15.** First row shows extracted wavelets from sites 1244E, 1245E, and 1250F (left), along with their respective amplitude (center) and unwrapped phase spectra (right). The second row shows the same analysis for the composite wavelet, as well as the linear regression of the unwrapped phase spectra.

## **5. Acoustic Impedance Inversion**

Impedance inversion is a geophysical technique for creating an earth model incorporating seismic and well log information as input, where the geological model of one or more elastic parameters is iteratively updated to find the best fit with the seismic data. We applied this technique to hydrated sediments in 3D data from Hydrate Ridge. These sediments are characterized by higher velocity and lower density than surrounding sediments. As a result, the acoustic impedance of hydrated sediment is generally higher than that of the surrounding sediment. In addition, marine sediments bearing gas hydrates are commonly underlain by a reflection that runs approximately parallel to the seafloor called the bottom simulating reflector (BSR). This reflector indicates the base of the hydrate stability zone and whose amplitude is generally accentuated by free gas below the BSR.

### ***A. Low Frequency Model***

Seismic data does not contain a low frequency component in its frequency spectrum. This information is important because it conveys various rock properties such as lithology, compaction, and pore pressure. Full-band impedance inversion to rock properties requires this information to be present. To do this, data from different sources are combined to create what is called a “low frequency model”. These sources include smoothed well logs, RMS or interval velocity from seismic, and picked horizons. At Hydrate Ridge, seismic velocities were not available, leaving out an important source of spatial low frequency information. Velocities stabilize the low frequency model where there is no well control, adding information that defines the compaction trend, overpressure zones, or large scale lithologic trends. In Hydrate Ridge, velocities would define the intensity and lateral extent of hydrated sediments, which well control alone is unable to do (this is demonstrated in Kumar, et al, 2006).

To build a geological model in Hydrate Ridge it was necessary to map seismic horizons throughout the seismic volume. We used three horizons in the low frequency model: 1) the seafloor (“Seafloor”), 2) horizon defining the west flank of the structure (“Unconformity”), 3) the BSR. A fourth horizon constraining the inversion at its base was obtained by adding a constant of 200ms to the BSR horizon.

Smoothed versions of the acoustic impedance logs from the five wells were spatially interpolated by honoring the internal geometries between each horizon. For this study, the stratigraphic architecture that best described the geology was proportional topology, where the internal sub-layers are parallel to the mapped seismic horizons (Table 2). Well control was interpolated throughout the volume using kriging to determine the spatial continuity of acoustic impedance over the principal layers. The final model appears reasonable given the limitations in the input data (Figures 16, 17).

Hydrate Ridge	Top	Base	Topology
Layer 1	Water Bottom	Unconformity	Proportional
Layer 2	Unconformity	BSR	Proportional
Layer 3	BSR	BSR +200ms	Proportional

**Table 3. Layer configuration for the low frequency model in Hydrate Ridge.**

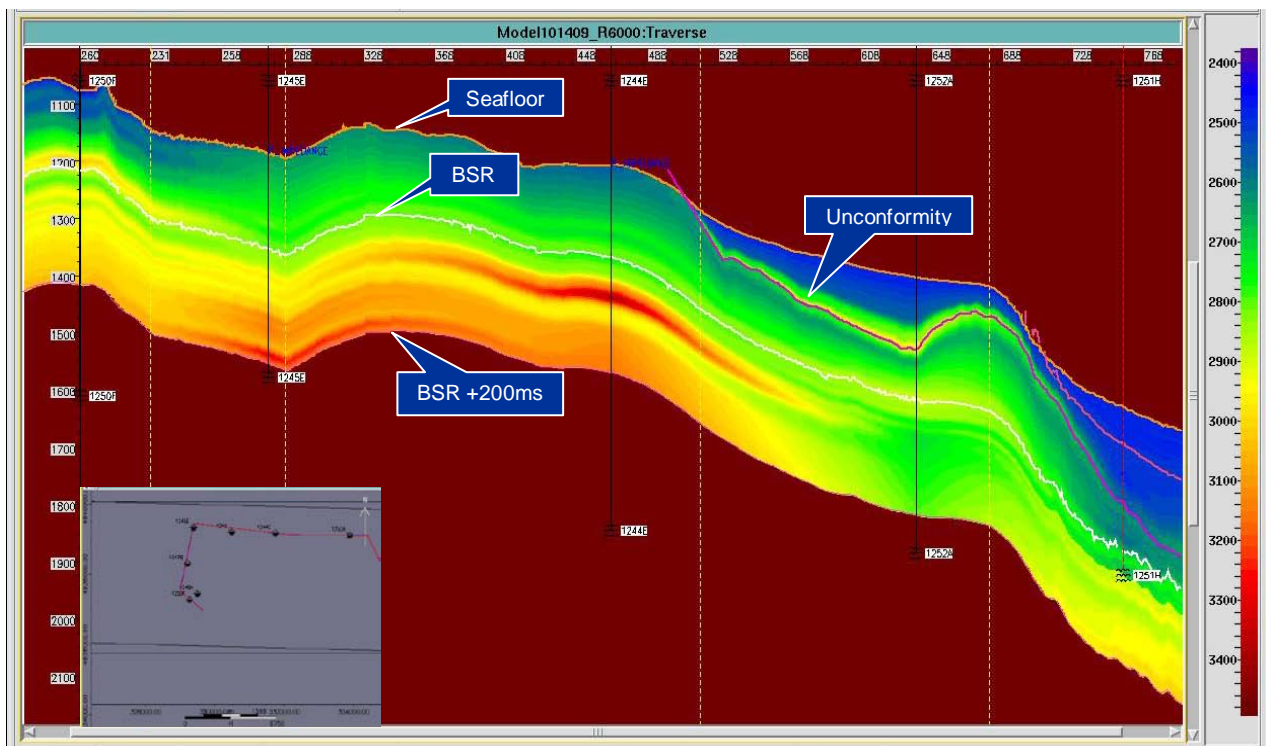


**Figure 16. Arbitrary line through wells 1250F, 1245E, 1244E, 1252A, and 1251H showing the low frequency model from west to east. Overlying are the horizons used for this model.**

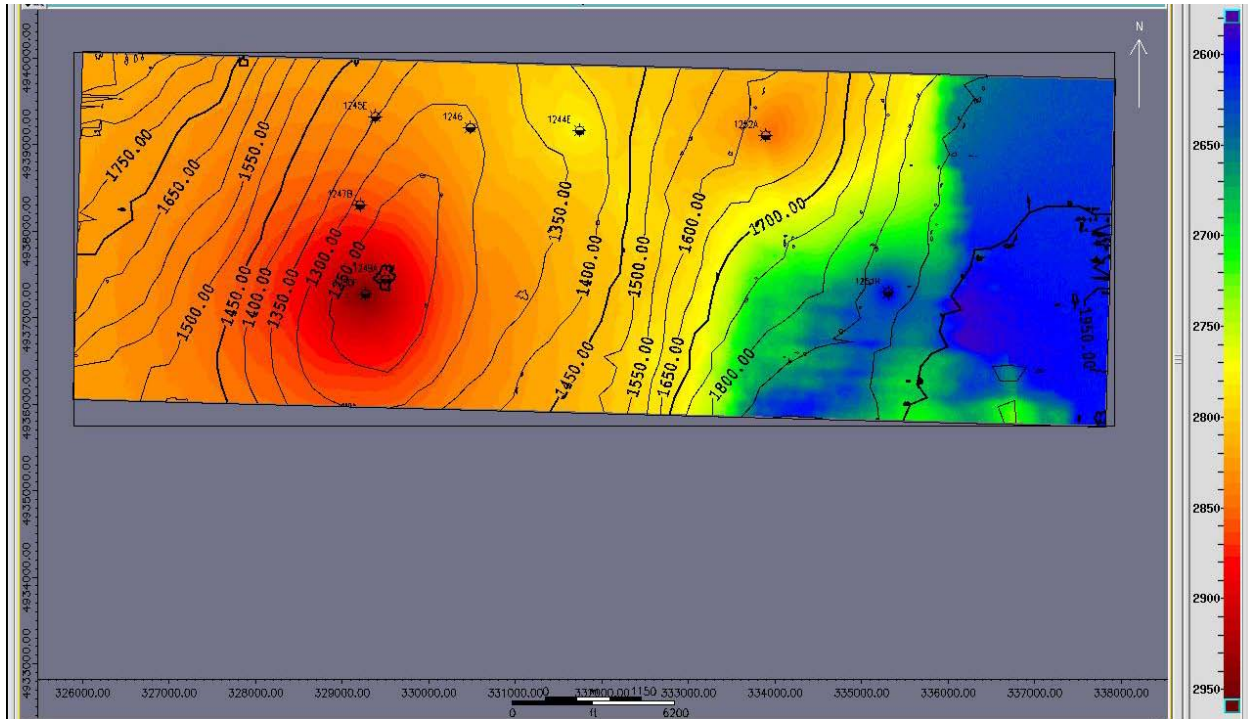


**Figure 17. Low frequency model extraction on BSR horizon. Sample values extracted at a point 30 ms above the BSR to avoid potential edge effects. Contours show BSR horizon times.**

## ***B. Impedance Inversion Procedure***

For this project, we used the IFP (Institut Francais du Petrole) Bayesian prestack simultaneous inversion algorithm. Although it is a prestack algorithm, we used it in a post-stack sense, meaning that we inverted a stack data set to obtain an acoustic impedance volume. The algorithm uses a model-based inversion approach where the input background model is continually modified until reaching a stable solution. It assumes that seismic noise and elastic model uncertainties can be described by zero-mean Gaussian probabilities. Using those assumptions, an objective function is minimized that has both seismic and geological terms (Tonellot, et al, 2001; Tonellot, et al, 2002).

Inputs into the inversion were the composited wavelet, background model, and seismic conditioned stack. When using this algorithm in a post-stack sense, several parameters need to be tested to optimize the inversion (Table 3). The first two are confident factor (noise content) and standard deviation of the acoustic impedance. The confident factor indicates the reliability of the seismic information used in the inversion. Its values vary from 0 to 100 with 0 being the minimum credibility and 100 being the maximum credibility. A value of 30 is the default value

and indicates average noise content in the seismic. Standard deviation is the maximum allowable variation from the background model. A standard deviation of 100 was used, meaning that the inverted impedance was allowed to have a maximum standard deviation from the low frequency model of 100 g/cc\*m/s. Its purpose is to ensure that the inversion does not generated unrealistic results.

The next three parameters are: (1) Wavelet scale factor (determined during wavelet extraction and fine-tuned during inversion parameterization), (2) lateral constraints (sets the distance in both inline and crossline directions for correlation to the trace being inverted), and (3) number of inversion iterations that are calculated for error minimization between seismic and modeled synthetic seismic (Table 3). Wavelet scale factors are chosen such that the inversion impedances have about the same excursion or absolute values as the upscaled well logs. In this case, a value of 0.56 means the wavelet was scaled down by a factor of 2. The lateral constraints were set to one trace width (12.5 m), meaning they were essentially not used. The default number of iterations is 30 but can range up to 150-200. Typical values are 60-100, as was used in this case. The result is shown in Figures 18,19.

<b>Inversion Interval:</b>	Seafloor to BSR+ 200ms
<b>Input Seismic:</b>	Post-stack conditioned
<b>Noise Content:</b>	30
<b>AI Standard Deviation:</b>	100
<b>Wavelet Scale Factor</b>	0.56
<b>Lateral Constraints</b>	12.5 m
<b>Number of Iterations</b>	60

**Table 4. Parameters used for the acoustic impedance inversion.**

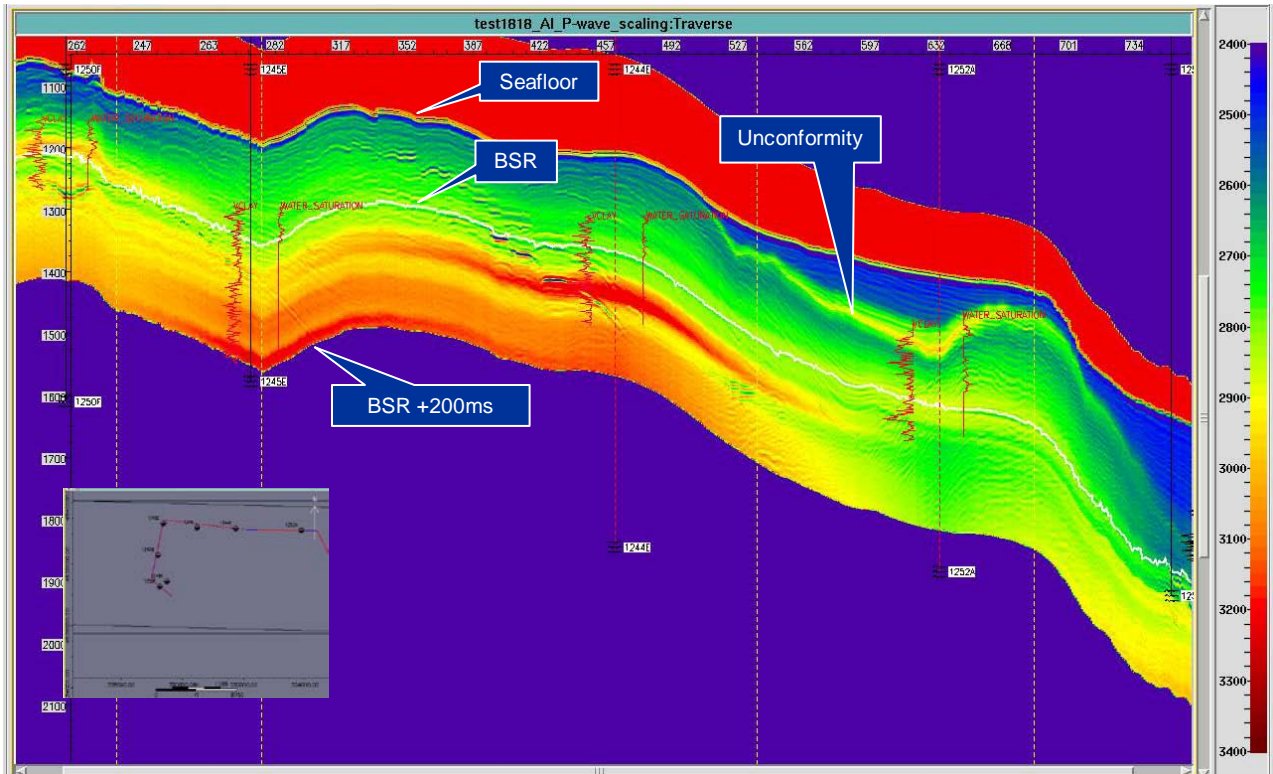


Figure 18. Arbitrary line through wells 1250F, 1245E, 1244E, 1252A, and 1251H showing the inverted AI volume from west to east. Overlying are the well locations, with volume of shale log (left) and water saturation log (right).

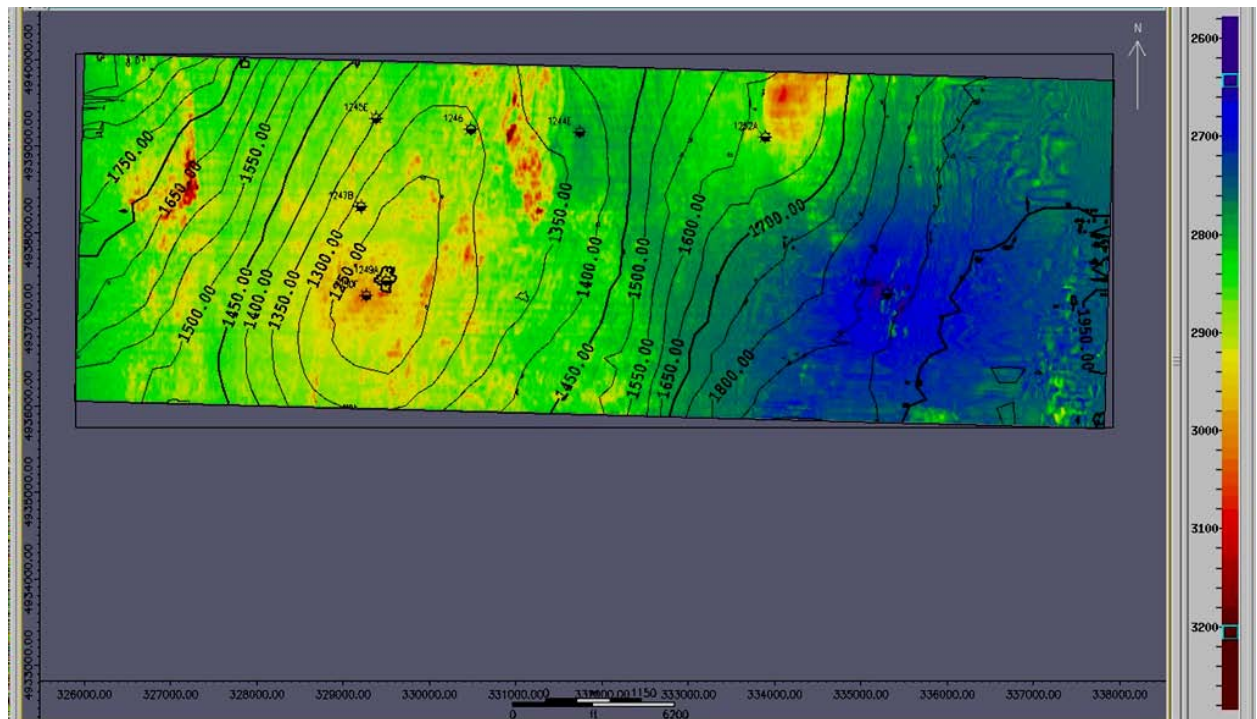
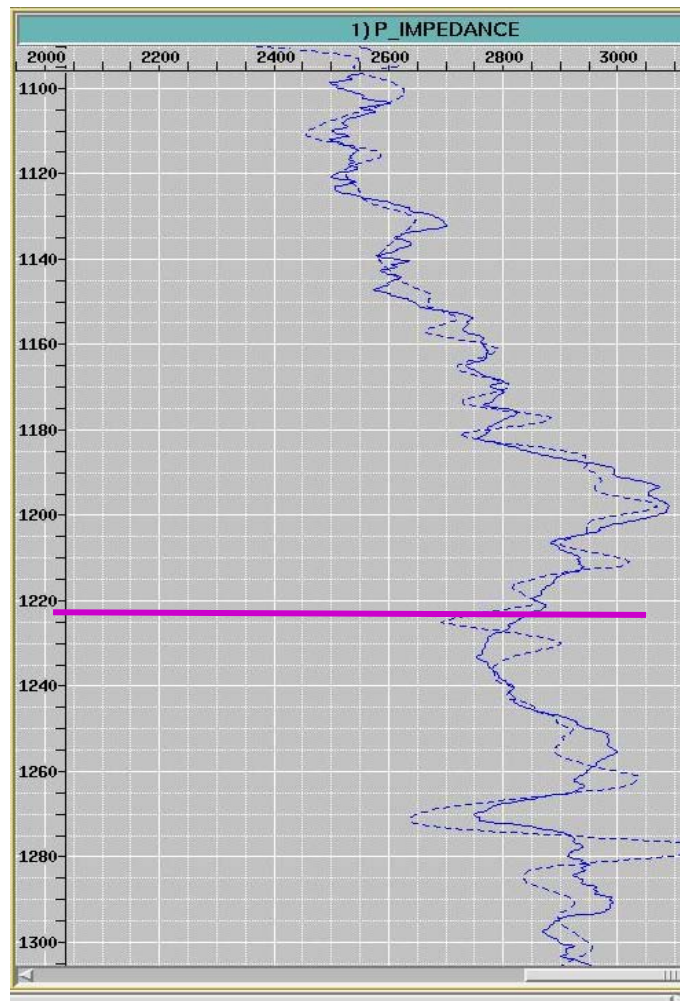


Figure 19. AI inversion extraction on BSR horizon. Sample values represent the maximum value from 0-100 ms above the BSR. Contours show BSR horizon times.

Several displays were used to quality control (QC) an inversion results. An important QC is a comparison of the extracted impedance curve from the inverted volume and the upscaled acoustic impedance log curve (Figure 20). The two curves overlay each other reasonably, although the reflectors at the BSR and in the gas-charged sand at the bottom of the well are more pronounced in the inversion than they are in the upscaled log. This was commented on previously (Section 5b, and shown on Figure 13) in context with the modeling performed on the well logs (Section 3).



**Figure 20. Inversion QC plot: Acoustic impedance trace extracted from the inverted volume (dotted) versus upscaled acoustic impedance log (solid).**

Another QC is the evaluation of inversion residuals, defined as the difference between the input seismic and the synthetic seismic after the 60<sup>th</sup> iteration. Inversion synthetics are produced by a

simple convolution of the reflection coefficients produced by the inversion of the seismic data, with the wavelet used in the inversion. In theory, a perfect inversion will have no residuals. However, in the real world, seismic data is not a completely accurate image of the subsurface, the seismic wavelet is not laterally and vertically stationary, and the extracted wavelet is not a perfect representation of the seismic wavelet. Therefore, an analysis of the inversion residual is a key diagnostic QC to determine how the inversion performed.

In the Hydrate Ridge inversion, the residuals are quite low over the inverted section except for the highest amplitudes (Figure 21, top). Excluding the seafloor, the BSR, and the gas-charged sand below the BSR, all that can be seen is a low frequency oscillation in the residual section. This observation is confirmed in the spectral domain (Figure 21, bottom), where the dominant residual energy band is about 50 Hz compared to a dominant seismic energy of 70-130 Hz. This is a direct result of the inverted synthetic seismic having a narrower bandwidth than the original seismic data. Nonetheless, this residuals analysis shows that the inversion is in general faithfully transforming the seismic signal into the appropriate impedances.

The seafloor reflector quite obviously has a more compact wavelet than was used to invert the remainder of the seismic section. The synthetic seafloor reflector has multiple oscillations that are not present on the seismic data.

The BSR and gas-charged sand in the lower portion of the section have similar seismic and synthetic signatures, but residuals are still present. These residuals are distinctly lower in frequency than either the seismic or synthetic reflectors, and again indicate that there are lower frequencies in the seismic than are present in the inverted synthetic.

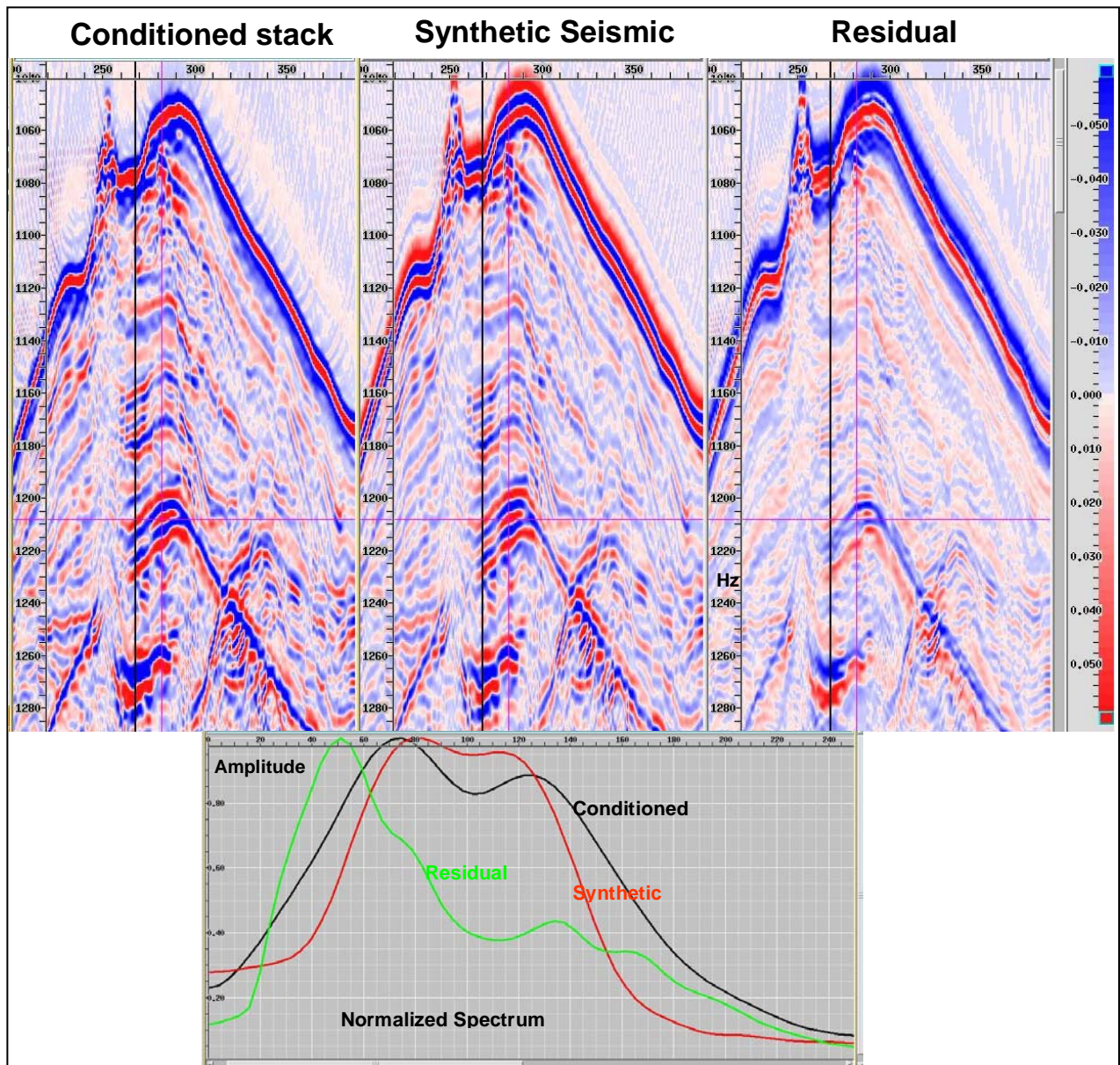


**Figure 21.** Top: Residuals analysis from left to right: 1) conditioned stacks, 2) synthetic seismic, and 3) residuals. Bottom: normalized amplitude spectra of the three panels. Because the spectra are normalized, the plot does not indicate the energy contained in the data, only the relative shape of the spectral curves.

## 6. CATTs

CATTs are obtained by cumulative integration and reflect a summation of petrophysical properties. Thus, they represent bulk properties rather than a single point response. These attributes are designed based on specific rock physics transforms that relate gas hydrate saturation to P-wave velocity.

We computed two seismic cumulative attributes -- saturation and accumulative volume. Saturation is a cumulative property that relates the fraction of hydrate concentration to acoustic impedance. Cumulative volume is a correlation between impedance and hydrate percentages across a hydrate bearing interval.

In order to calculate CATTs on seismic data it is necessary to use rock physics transforms that are case-specific. Thus, the transforms employed in this study are valid only for Hydrate Ridge. Figure 22 shows a crossplot between the inverse of the P-wave impedance squared ( $AI^{-2}$ ) versus gas hydrate saturation ( $S_{gh}$ ). The data plotted included all six wells employed in this study. The relationship between  $AI^{-2}$  and hydrate saturation is an empirical relationship from well log data (Equation 1). It appears to be linear and the best fit can be expressed by:

$$S_{gh} = -13.3 / AI^2 + 1.8 \quad (1)$$

where  $AI$  is in km/sec gr/cc.

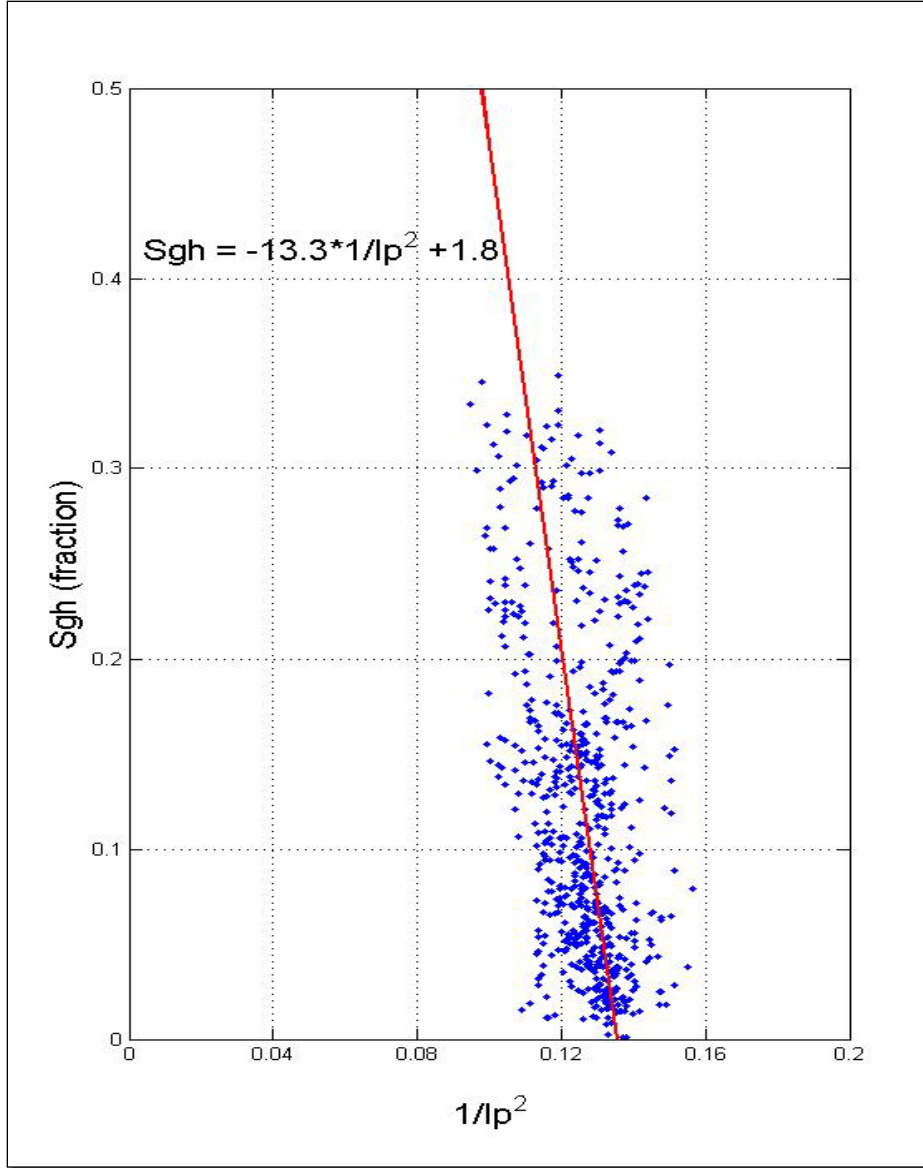


**Figure 22. Inverse of the P-wave impedance square ( $1/AI^2$ ) vs. gas hydrate saturation crossplot. Red line is the best linear fit to the data from all six holes.**

The next step in calculating CATTs on Hydrate Ridge seismic data is to estimate the accumulated gas hydrate volume. Hydrate Ridge bulk density is about 1.7 g/cc at hydrated sediments. This density corresponds to sediments with 60% porosity. Thus, the accumulated volume of gas hydrates found between two vertical stations is:

$$V_{gh} = \int_{\tau_1}^{\tau_2} [-1.56AI^{-2} + 0.211AI]d\tau, \quad (2)$$

where  $AI$  is in km/sec gr/cc.

The limits of integration for a hydrate volume in Equation (2) were set to 2.8 km/sec gr/cc. Accumulated gas hydrate volume is measure in hydrate volume per horizontal area ( $m^3/m^2$ ).

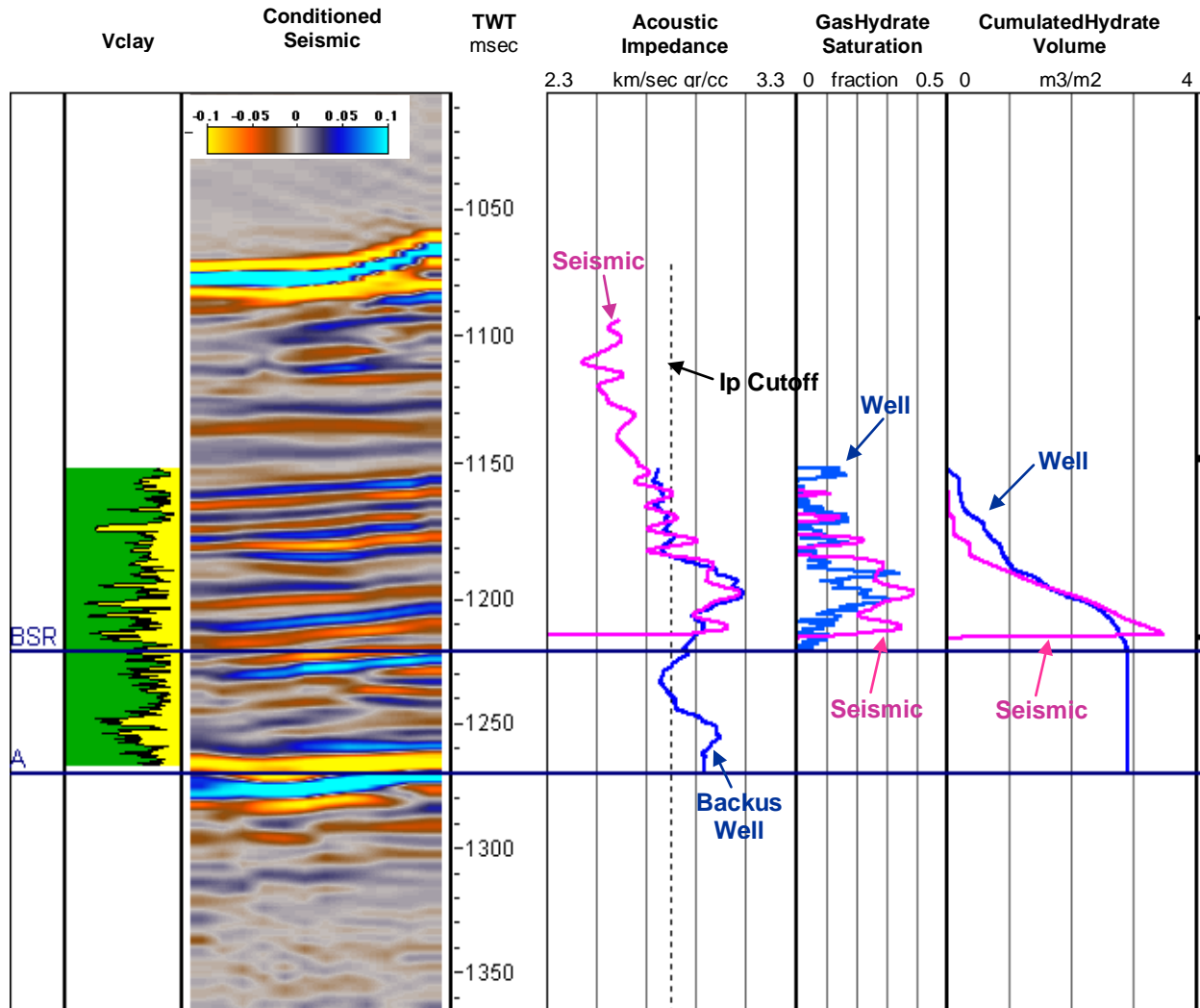


**Figure 23. CATT results at Hole 1250F. Track are as follow: 1. clay volume, 2. conditioned seismic data, 3 smoothed log impedance (light blue), and the extracted seismic P-wave impedance (magenta), and impedance cutoff (dashed black). 4. log hydrate saturation and the estimated seismic hydrate saturation. 5 cumulated gas hydrate volume from well log data (light blue) and from seismic data (magenta).**

Once the seismic saturation and the cumulative volume of gas hydrates have been obtained, traces at the well locations from these two outputs are extracted (Figure 23). Overall, hydrate saturation and cumulated hydrate volume calculated using well data is close to that calculated with seismic data, although in some intervals the seismic estimation misses and/or detects more hydrate saturations than well data. For example, in Hole 1250 (Figure 23) well log data indicates a gas hydrate interval at 1160 msec but seismic data does not have any reflector at that position. Similarly, seismic data show higher saturations than well log data between 1185 and 1215 msec.

One of the assumptions about unconsolidated sediments with gas hydrates is that these sediments have P-wave impedances much higher than the surrounding unconsolidated sediments without gas hydrates. This is true in some places, but clearly this is not the case everywhere. Reflectivities in some of the small hydrate accumulations are not large enough to bring them above the background. As a result, the method successfully detects some hydrates intervals but misses hydrate intervals that do not have seismic expression and also detects some false positives.

However, note that the accumulated hydrate volume in track 5, Figure 23 does match the well log-derived CATTs volume. This is obviously the result of hits, misses, and false positives, but does demonstrate that this method might show promise for approximating gas hydrate volume.

Thus, these two attributes were calculated on the inverted seismic volume. The hydrate saturation volume (Figure 24) shows the main accumulation in the highest elevations of the summit area with areally smaller but higher saturation accumulations associated with structural elements in the prospect area. Note that the saturation indication to the northeast of well 1252 is a false positive resulting from a high impedance sand in that fold block. The cumulative hydrate volume (Figure 25) shows by far the highest accumulations in the summit area. Again, the reading at the 1252 well is a false positive.

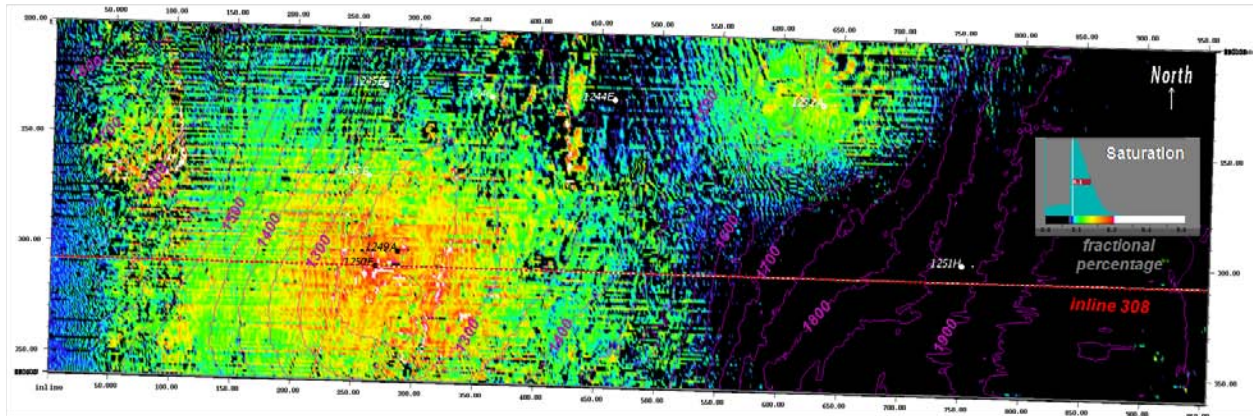


**Figure 24. Hydrate saturation in decimal percent. Extraction of saturation values is from within the hydrate stability zone for a horizon slice 13 ms above the BSR. Histogram depicts positively skewed frequency distribution of saturation values extracted for this surface. Contours show BSR horizon two-way travel time [ms].**

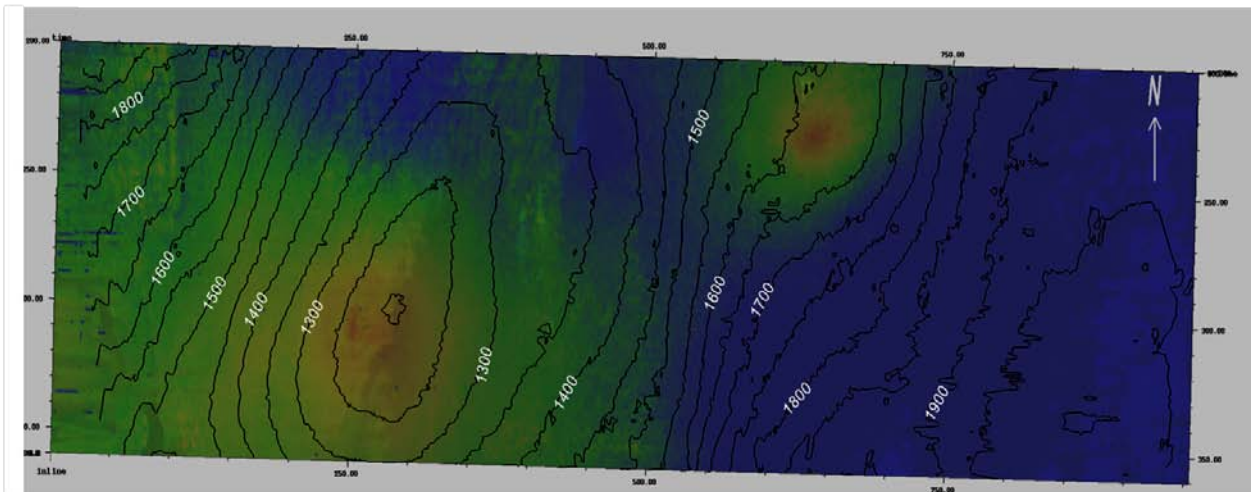


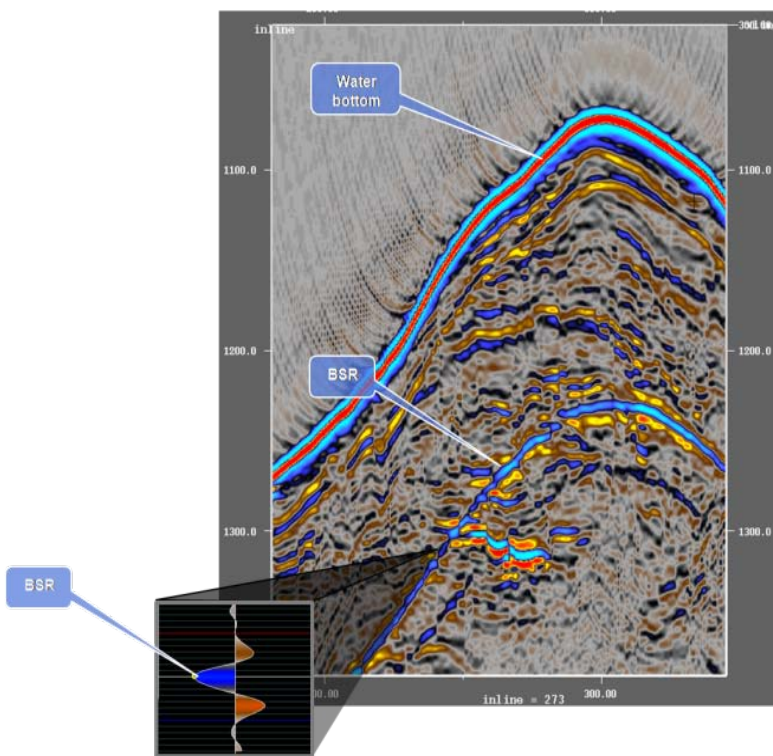
**Figure 25: Volume of hydrate saturation in  $m^2/m^3$ . This is the integrated cumulative attribute (CATT). Contours show BSR horizon two-way travel time.**

## 7. Amplitude Interpretation

### A. Bottom-Simulating Reflector (“BSR”)

This section reviews the controlling effect that pressure and temperature exert on a bottom-simulating reflector (BSR) by examining its spatial and temporal distribution. The BSR demarcates the base of the gas hydrate stability zone (“GHSZ;” e.g. Torres et al., 2004).

#### Definition



AGI’s glossary describes the bottom-simulating reflector as:

*“A reflection that roughly parallels the sea-floor reflection, caused by the [acoustic] contrast between an overlying clathrate (gas hydrate) and underlying gas-saturated sediment [Figure 26]. Occurs in deep-water where subseafloor sediments at low temperature are under substantial pressure.”*

*from AGI’s “Glossary of Geology,” edition 5, 2005*

**Figure 26. BSR in relation to water bottom (detail of IL273).**

### B. BSR Reflectivity Placed Within Spatial and Temporal Context

BSR reflectivity is primarily governed by the acoustic contrast between the GHSZ and the underlying, fully thawed section. Therefore, BSR reflectivity is generally high, where overlying strata have been substantially hydrated ( $S_{gh} > 20\%$ ) which is generally the case at high structural elevations cored by older, thrust strata (Chevallier, et al., 2006) and for middle Pleistocene

turbidite sands draping the eastern structural flank of the dome at *albeit* lower structural elevations. However, locally, where the top of an underlying, “free gas”-bearing sand coincides with the base of hydrated section above, anomalously high BSR reflectivity values can be recorded. Although these amplitude values receive a boost from constructive interference between two negative polarity reflections (Chevallier, 2006) — and, therefore, may not necessarily be proportional to the degree of hydrate saturation experienced by the section above — such heightened BSR reflectivity may still provide valuable exploration leads to locate hydrated sands by tracking “free gas”-bearing sands structurally updip. In this case, reflections from the seismically resolved top and base interfaces of such a sand interval will undergo a characteristic polarity reversal across the BSR, because the formerly “free gas”-bearing sands have become “frozen” above the BSR contact, thus effectively inverting the negative acoustic contrast to the encasing fine-grained sediment.

In this report we focus on two intervals exhibiting acoustic behavior that verifies gas-to-hydrate phase transition within the same reservoir sand. We analyze one of them in detail (i.e., hydrated sand “B;” see section 9[c]. below). Prior to attribute analysis of individual sands, however, we place BSR reflectivity within its spatial and temporal context.

## **i. Spatial Context**

Because a BSR is the seismic expression of a pressure and temperature controlled phase boundary above which methane gas–water emulsions transition to a combined solid crystalline state known as “clathrate,” the BSR’s subsurface elevation may fluctuate regionally or locally, as governed by variable confining pressures and freezing temperatures. Potentially, the BSR’s acoustic signature may even be obliterated if convective flow and thermal perturbations create conditions unstable for hydrate retention in general (Figure 27).

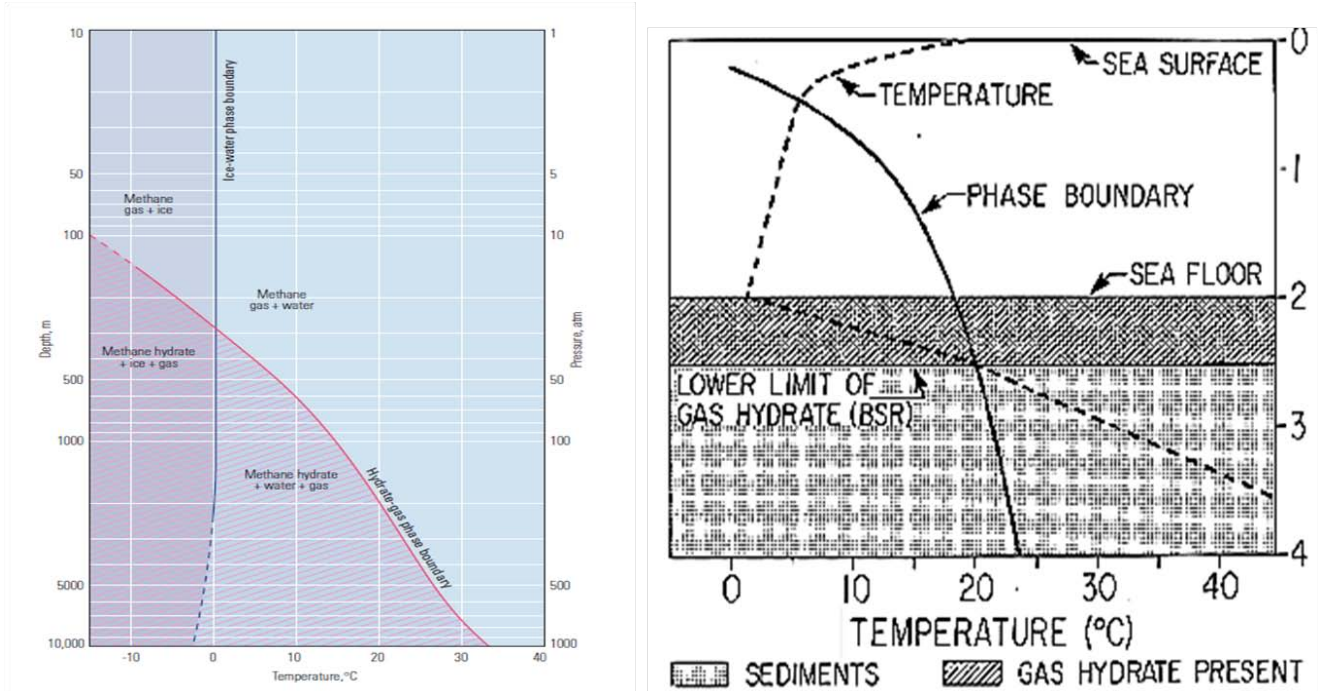


**Figure 27. Temperature-pressure phase boundary diagram of gas hydrate-methane gas-water-ice system (left image from Collett et al., 2000; right-hand side image from USGS Woods Hole Oceanographic Center,2000)**

To investigate and potentially separate the effects of pressure and temperature variation on BSR subsurface elevation, we chose the mapped water bottom as a datum (Figure 28 top) and then flattened the stacked seismic section (Figure 28, bottom). Projecting the outline of the original water bottom onto the flattened amplitude volume (Figure 28, bottom), we generally observe a positive correlation between water depth and thickness of the GHSZ. However, we also notice an increase in subsurface elevation of the BSR wherever water depth has increased (Figure 28, bottom). This observation suggests that BSR subsurface elevation is primarily a function of pressure and not of temperature. Moreover, we observe that for equal water depths, the two-way travel-time thickness of hydrated section on the western flank of the dome is slightly diminished compared to its eastern pendant (Figure 28, top). This observation may be attributed to either a laterally varying temperature regime, lateral velocity changes (the rocks on the west are older, and, perhaps, faster [e.g., Chevallier et al., 2006]), or, a combination of both. Primarily, however, these observations suggest that pressure exerts the dominant control on BSR elevation.

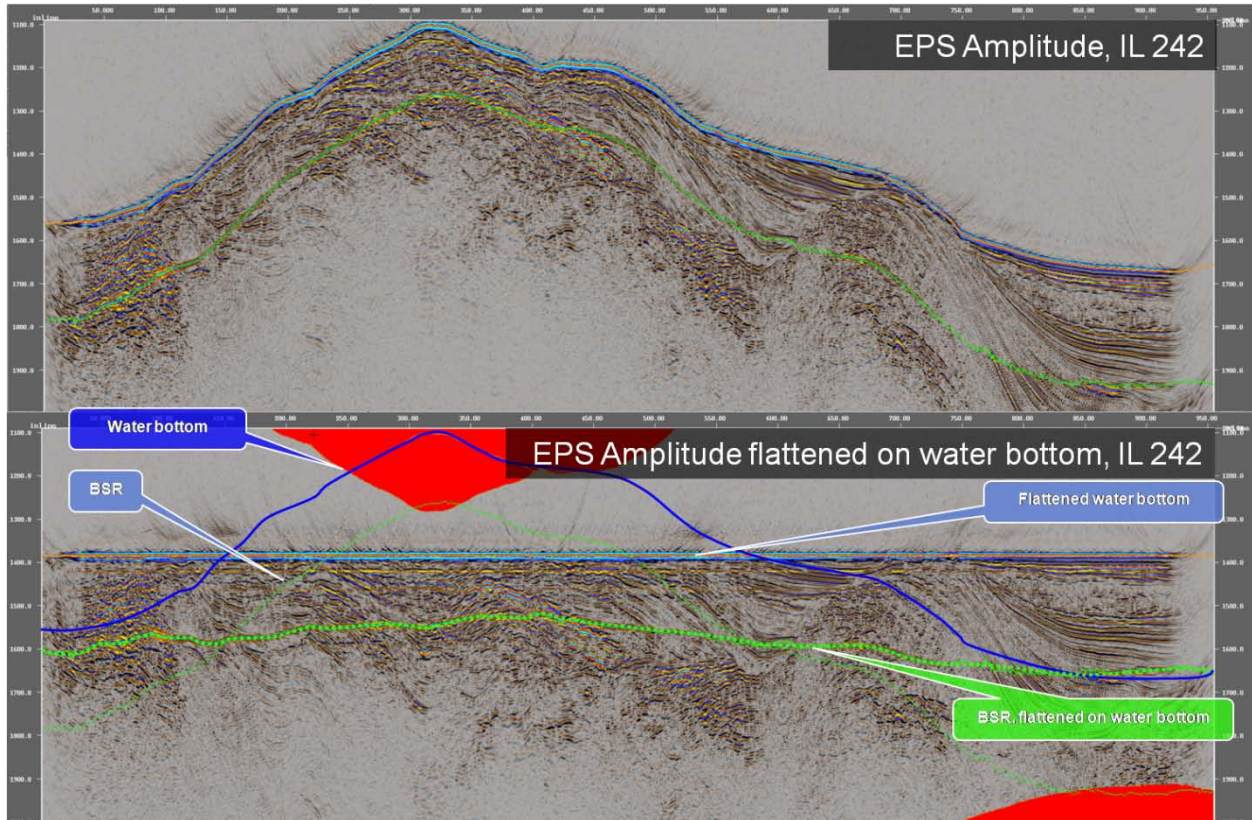


**Figure 28. Unflattened (top) and flattened BSR (bottom). BSR in flattened amplitude section does not exactly run parallel to the water bottom reflection. Mud line to BSR depth is maximized where water depth is greatest, because hydraulic head increases permitting the BSR contact to subside in subsurface elevation.**

To calculate GHSZ thickness we used a single, but deemed adequate, constant velocity of  $1,600 \text{ ms}^{-1}$  (given by Chevallier et al., 2006), primarily because RMS velocities from processing were not available. We then cross-plotted hydraulic head against GHSZ thickness (Figure 29). Because this cross-plot depicts thickness of hydrated section as a function of pressure, if points diverge from what should be a single, established trend line (red arrow, Figure 29), they would do so in response to changes in temperature or because application of a constant velocity provides too general an approximation.

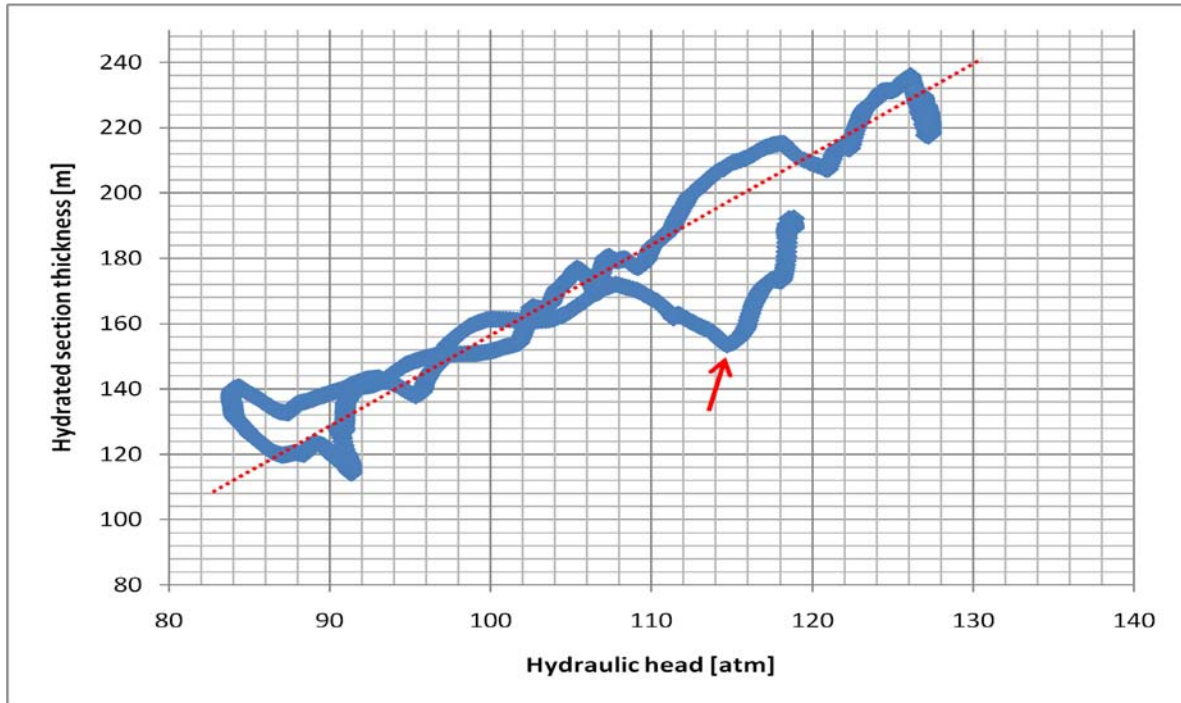


**Figure 29. GHSZ thickness as a function of hydraulic head (data from inline 242 shown in Figure 28). Dashed red line depicts the general trend line in the data. The red arrow highlights the largest deviation from this trend line which is found to be for data points from the western edge of the dome (denoted by red arrow). This deviation (more than one standard deviation removed) either reflects the effects of a higher thermal gradient, presence of a higher than applied average velocity in the west (older rocks are present there as pointed out by Chevallier et al., 2006), or a combination of both mechanisms, that has reduced thickness values for the GHSZ in that area.**

Nevertheless, within the Hydrate Ridge 3D data we observed that the subsurface position of the BSR is primarily pressure-controlled, as its location shifts toward greater depth with increasing water depth. Only in one instance can the primary importance of temperature on BSR subsurface stability clearly be documented: on the crest of Hydrate Ridge a cap carbonate pinnacle crowns a cone-shaped chimney structure at the base of which the BSR has been completely obliterated (Figure 30). At that location, the cone-shaped chimney structure contains low amplitude reflectors immediately overlying the projected tip of a fault-propagation thrust cutting (but not offsetting) the present-day BSR. This structure supports the notion that higher-temperature “free gas”-bearing fluid flow sourced from “Horizon A” of Tréhu et al. (2006) below the BSR, possibly facilitated by the fault, is causing hydrate dissolution within the GHSZ. Seismically this zone is evidenced by a narrow vertical corridor near the crest of the dome that is seismically transparent (Figure 30).

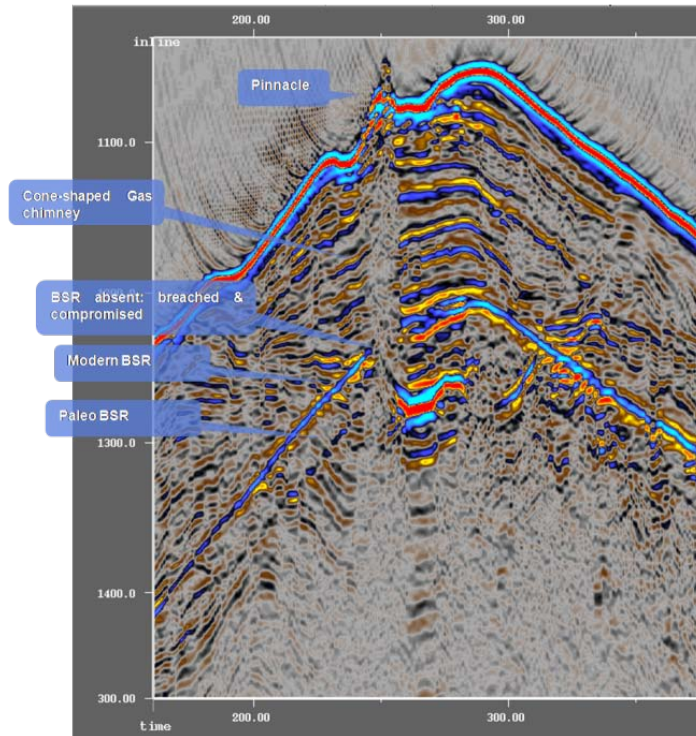


**Figure 30. Pinnacle with gas chimney and breached bs (il300).**

However, the observed effect on seismic data of elevated temperature on BSR stability quickly dissipates away from this local disturbance after a distance of less than 150 m. Areally the cone-shaped expulsion zone within which gas is transported to the seafloor appears to be rather narrowly confined (“base of chimney,” Figure 31, lower).

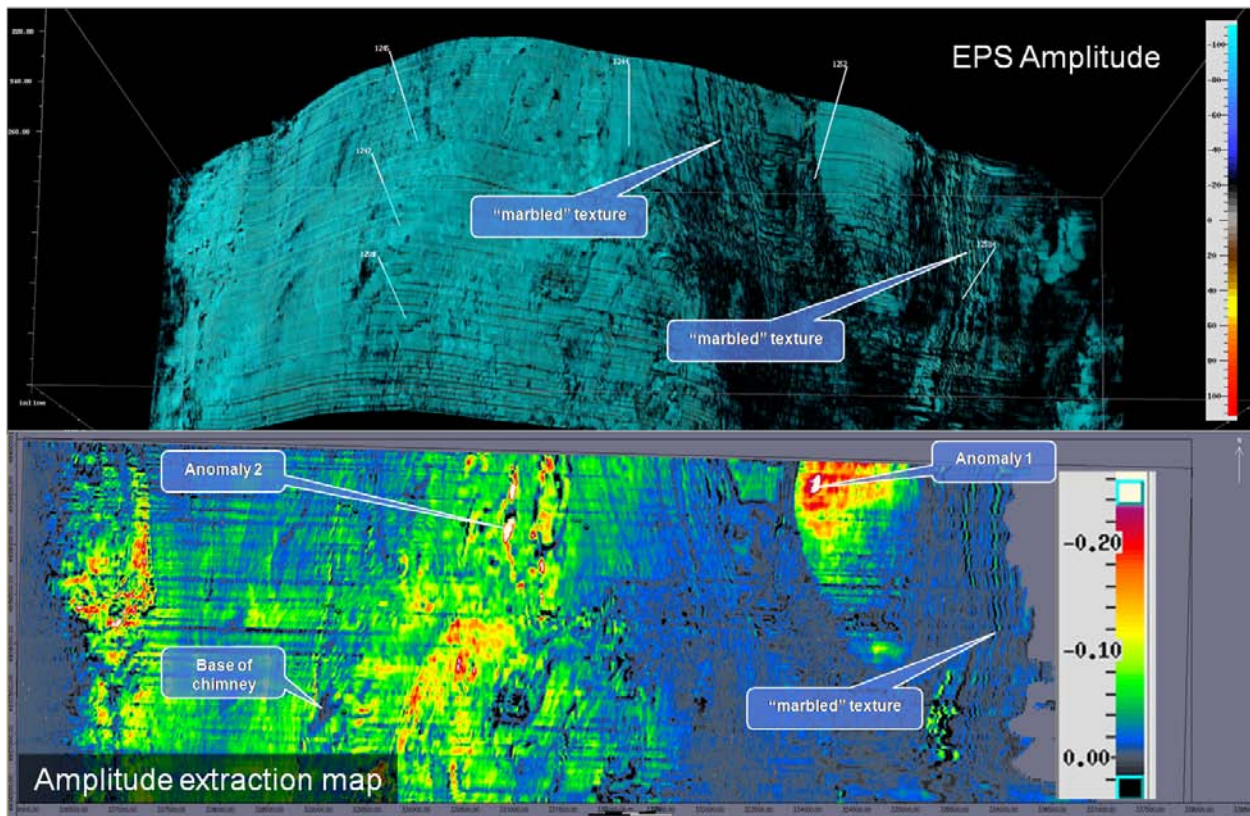


**Figure 31. Perspective view (top image) and map of BSR (bottom image). On the flanks of structural domes the BSR cuts across steeply dipping reflections, producing a marbled reflectivity texture that pre-empts a direct proxy of gas hydrate from BSR amplitude reflectivity alone. In contrast, two amplitude minima occupying gently dipping areas suggest increased acoustic contrast there, possibly due to higher hydrate content above the reflective interface or “free” gas below the interface generating the BSR reflection.**

As follows from its name, the BSR mimics seafloor topology. Hence, where strata dip is incongruent with seafloor dip, the BSR cuts across stratigraphy, forcing a complex pattern of phase changes giving the appearance of a marbled texture (Figure 31), not unlike that of an unconformity in seismic data. This complexity results in increased heterogeneity of attribute signatures over those areas. This is the case in the eastern region of the survey, which does not have a clear BSR, because of an obtuse dip angle between the BSR and seismic reflections, creating a marbled texture from juxtaposition of alternating zones of constructive and destructive interference (Figure 31). For this entire region, the BSR had to be mapped manually by extrapolating intermittent segments within which the BSR reflection is coherent, and therefore well documented. We attribute the poor or even completely absent BSR in this overall region to a lack of entrapment of migratory gas above generally low-lying structural zones, and, perhaps, a lack of faulted conduits (e.g., Chevallier et al., 2006), but not to temperature. Where dips of

the BSR and genuine strata reflections run subparallel to one another, stronger BSR reflectivity results (Anomaly 1, Figure 31). In other cases, constructive interference from gas-bearing sands with the BSR creates amplitude anomalies (Anomaly 2, Figure 31; Chevallier et al., 2006). Therefore, BSR reflectivity, taken as a whole, is not a good proxy for gas hydrate occurrence in the GHSZ.

## ii. Temporal Context

In addition to depth variations of the BSR, we present evidence for temporal (pseudo-4D) BSR abandonment, mobilization, and re-equilibration (Figure 32), as described by Bangs, et al., 2005, and Tréhu, et al., 2006. We note, however, that other scientifically valid explanations have been proposed elsewhere to explain the observed seismic signature of a faint “ghost” image in a deeper, BSR-parallel trough reflection. One theory is that it is an acoustic contrast generated by Structure II hydrate (Claypool, et al., 2006). However, *“ambiguity remains about whether a second faint BSR.....is due to the presence of Structure II hydrate”* or represents an acoustic *“relic”* stemming from an abandoned paleo-BSR (e.g., Bangs et al., 2005; Tréhu et al., 2006). Although sediments below the primary BSR theoretically are of slightly lower density, if they also contained a higher number of large cavities, it would permit Structure II hydrate (if present) to create a similar acoustic contrast as a Structure I hydrate (a likely phenomenon in hydrates that are populated, at least in part, by thermogenic gas). However, we note that the observed BSR-parallel reflection always features weaker reflectivity than the primary BSR, and thus conclude that a “relic” BSR interpretation appears more likely.

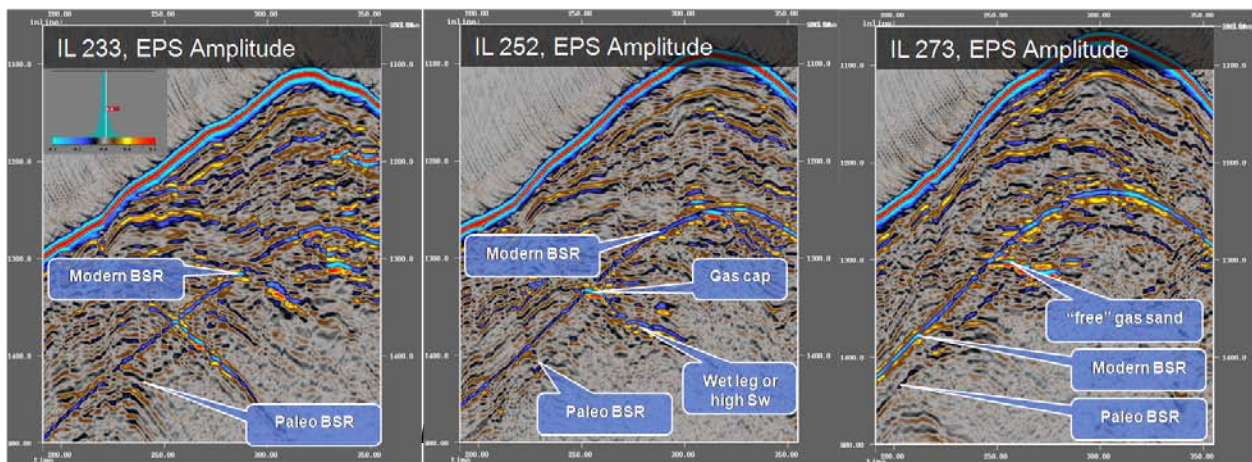


**Figure 32. BSR abandonment, mobilization, and re-equilibration.**

Given a  $V_p$  of 1.7 km/sec, the vertical distance between the interpreted paleo-BSR and the primary BSR at well 1247B amounts to a  $\Delta TWT$  of 32 ms, equating to a vertical distance of 27.2 m (~89 ft.) (Figure 33). Likewise, using this interval velocity gives a  $\Delta TWT$  of 35 ms and a vertical distance between the paleo-BSR and the primary BSR at Well 1245 of 29.75 m (~98 ft.) (Figure 34). Generally sub-parallel and regional translation of the BSR suggests abandonment of a paleo-BSR in response to reduced hydraulic head from glacio-eustatic sea-level fall and/or an episode of tectonic uplift after which the BSR re-equilibrated to its present-day elevations.

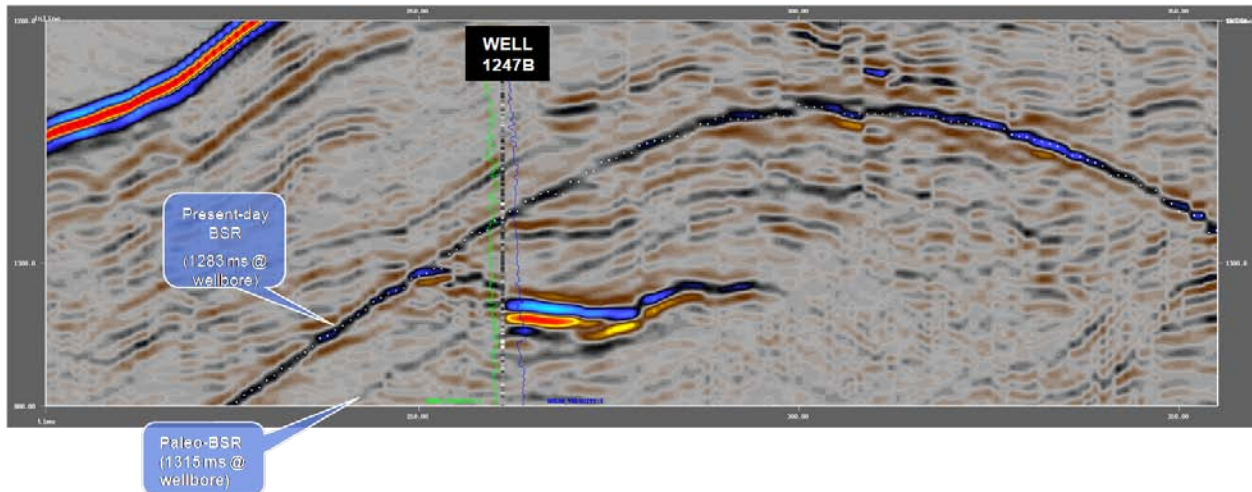


**Figure 33.** Temporal context of the BSR, well 1247B. Note entrapment of free gas against interpreted paleo-BSR suggesting retention of sealing capacity after methane evacuation from above the BSR at this site. This is in contrast to the more typical pattern of “free gas” bearing sands cutting across the paleo-BSR. (Well data: left track = sonic velocity; right curve = shear velocity; center track is ribbon band displaying  $V_{clay}$  content, with black = low  $V_{clay}$ , Yellow = high  $V_{clay}$ ).

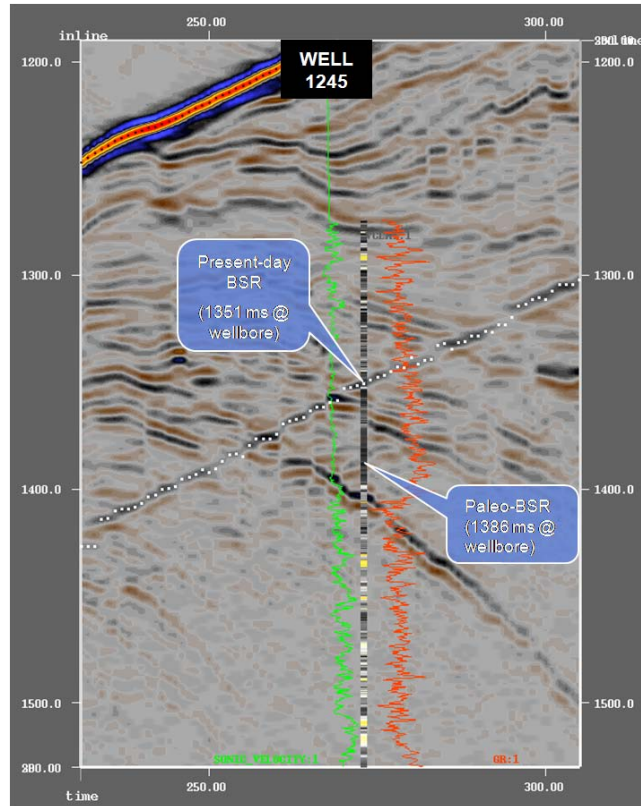


**Figure 34. Temporal context of BSR, well 1245. (Well data: left curve = sonic velocity; right curve = GR; ribbon band displaying varying Vclay content occupies the center track is, black = low Vclay, Yellow = high Vclay).**

## 8. Attribute Analysis

### A. BSR

Under the polarity convention wherein a peak corresponds to an increase in impedance, a propagating acoustic wave field will leave behind a strong, seismic amplitude half-cycle trough reflection upon exiting the base of the GHSZ. For this reason, the BSR frequently cuts across other reflections. Therefore, manual mapping of this subsurface feature is advised because a geological horizon ideally represents a surface of constant phase. Proper attribute extraction and successful visualization are phase-dependent and therefore require careful mapping of a geological feature without errors introduced by cycle skipping (phase shifts).

As mentioned, the BSR cuts across and in most cases “drowns” out seismic reflections that originate from the interaction of the wave field with reflective stratigraphic layers, implying that the acoustic contrast of the BSR is a non-stratigraphic contact that competes successfully

against most other naturally occurring impedance contrasts. In that sense, the BSR resembles an unconformity, as it often cuts across chronostratigraphic seismic events, but unlike an unconformity that may exhibit a phase shift or polarity reversal due to juxtaposition of layers of different acoustic impedance, the BSR polarity generally remains unaltered. The BSR reflection generally remains a “trough” throughout this dataset, except for areas where the location of the BSR had to be extrapolated because it was weak or absent.

BSR amplitude values vary considerably across the survey. They are most commonly weak, with strong trough amplitudes occurring only locally. This results in a negative skew in the frequency distribution of amplitude (Figure 35).

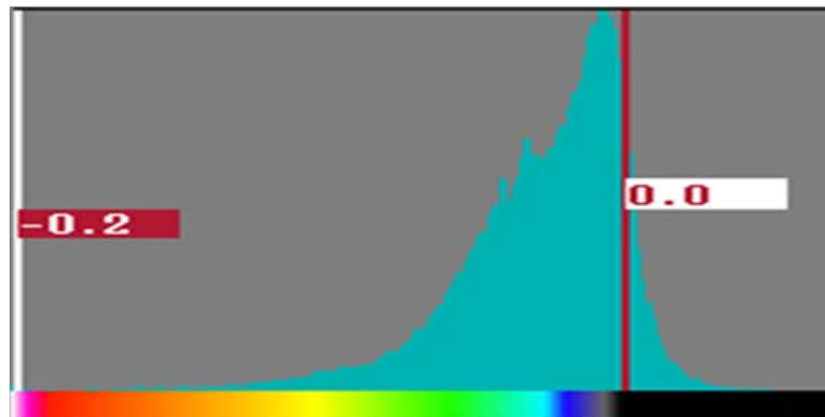


**Figure 35.** Frequency distribution of amplitudes extracted from BSR surface. Amplitude values have been extracted from the mapped BSR surface and pooled into a histogram distribution. The distribution shows a strong negative skew of the data population. A few positive samples stem from the eastern area of the survey across which the position of the BSR had to be interpolated.

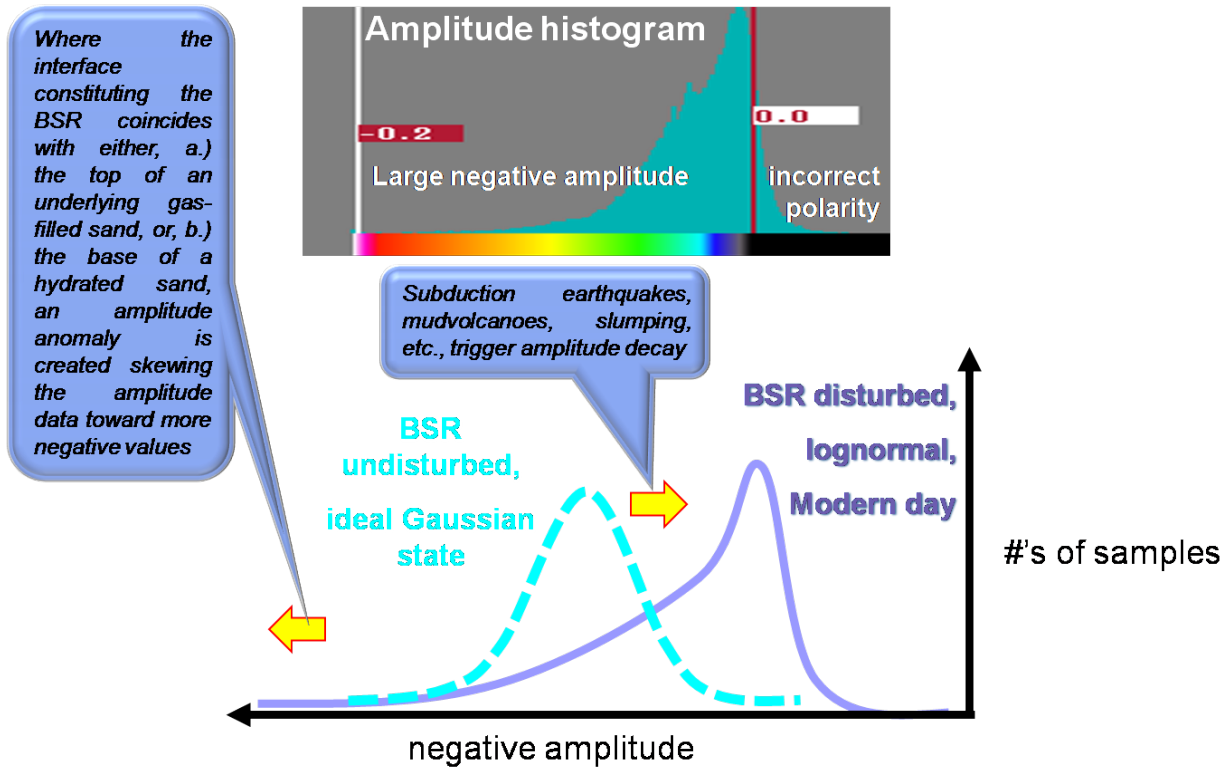


**Figure 36. BSR reflectivity explained in spatial & temporal context.**

The divergence of the observed amplitude distribution from the idealized Gaussian state suggests the presence of an “edge” having been superposed onto the seismic data. For instance, coherency, an attribute that depicts the degree of self-similarity between seismic traces, allows discernment of geologically meaningful edges in the seismic data that commonly correspond to faults or stratigraphic boundaries. Therefore, a skewed amplitude distribution here suggests importance of at least one “edge” effect that causes a transition in acoustic character from an idealized Gaussian distribution via either amplitude decay or amplitude boosting (Figure 36). Amplitude dimming at the BSR interface can generally be attributed to a lack of free gas migrating upwards and/or the lack of a well-defined GHSZ base. We speculate that relative sea-level fall causes upward translation and “melting” of the basal methane hydrate layer. Thus, uplift, a likely process to occur within an accretionary prism, may adversely affect hydrate saturation and result in reduced BSR reflectivity. In our experience gleaned from circum-Pacific analogs (Atsumi & Kumano 3-D surveys, Nankai trough), mud volcanoes and slumps overlying sectors of weak signal strength corroborate to support this interpretation of negative BSR amplitude skew from tectonic instability.

In addition to amplitude decay mechanisms, we also observe amplitude reinforcement from constructive interference of two half-spaces that artificially increase BSR reflectivity thus widening the negative skew within a histogram tallying BSR amplitude resonance (Figure 36).

### ***B. Hydrated Sand “A”***

We introduce two of several hydrated sands characterized by peak-trough couplets located above the BSR (“A” & “B” sands; Figure 37). For all hydrated sands, the general statement holds that the greater the resonance of the peak amplitude defining the top reflective interface of the sand in seismic data, the higher the degree of hydrate saturation. One of these sands, the hydrated sand “A,” could be located because at the site where the top of an underlying, gas-bearing sand coincides with the base of the hydrated section above, anomalously high BSR reflectivity values are recorded (Figure 37). Although the BSR amplitude values have become boosted by this constructive interference and the magnitude of BSR amplitudes at this site may not necessarily be proportional to the degree of hydrate saturation in the section above, this elevated reflectivity may still provide good clues to locate formerly gas-bearing sands that have become frozen above the BSR contact. Therefore, the projected dip of this “free gas”-bearing sand above the BSR contact can potentially help locate a hydrated sand. Interestingly, the overlying “B” sand boasts higher reflectivity in the hydrated section but no polarity reversal of the waveform occurs below the BSR, suggesting the presence of a wet leg of this sand. This supposition is supported by the  $S_w$  curve at well 1244E, which shows no gas in that portion of the sand (Figure 37).

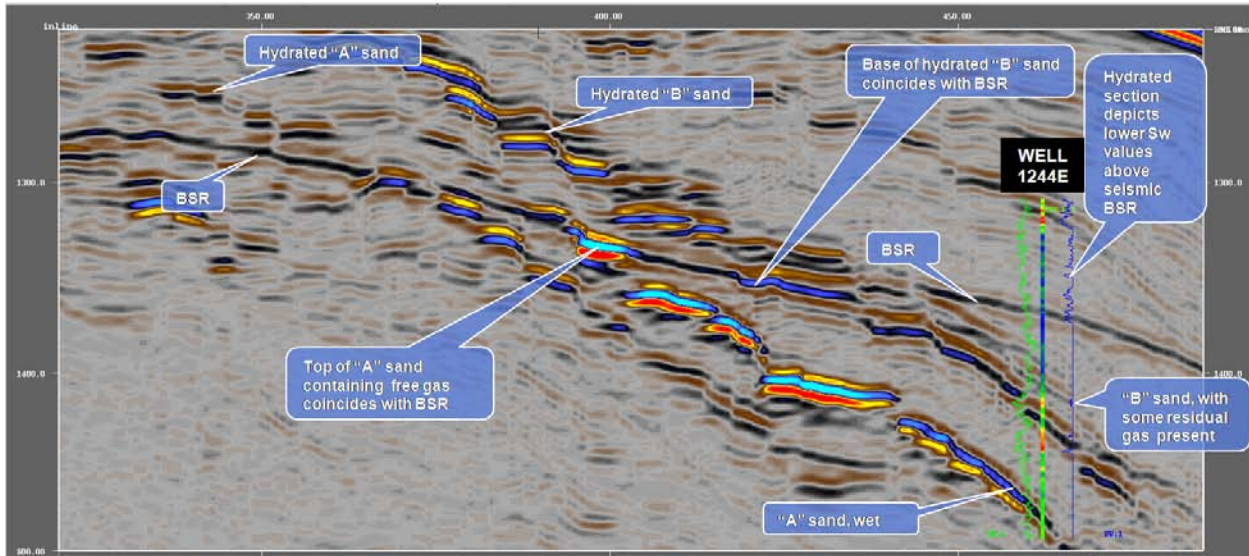


**Figure 37. Hydrated A & B sands.** The “free” gas in sand layer “A” that approaches the GHSZ from below boosts BSR reflectivity where the top interface of that gas-bearing sand coincides with the base of the hydrated zone. Immediately above the BSR, the top of sand A reverses polarity. Although generally of only moderate amplitude, the BSR amplitude flares up due to the added energy from this trough defining the top of the gas-bearing interface (constructive interference). In contrast, hydrated sand “B” exhibits no polarity reversal indicating that the gas-water contact occurs above the BSR within the GHSZ. (Well data: left track = gamma ray; right curve = SW; center track uses rainbow color map with red = high resistivity).

### C. Hydrated Sand “B”

Overall, the amplitude peak defining the top sand interface of “B” is greater than that of sand “A”. In addition, the area enclosed by sand “B” is larger than that of sand “A”. This can be seen on map views of attributes extracted from its upper reflective interface (Figures 38-41), which are discussed below and in figure captions.

Although acoustic impedance represents a linear property that is best represented by a linear color bar, assigning a graduated color bar nevertheless accentuates the observation that no impedance value greater than  $2,800 \text{ kg m}^{-2} \text{ s}^{-1}$  is observed south of the zero-slip perimeter established by normal faulting (green-to-red color transition in right-hand side image of Figure 39; white geobodies of Figure 40).

The integrated cumulative attribute (Figure 41) is designed to portray bulk properties of the rock column and is discussed more fully in subsequent sections on reserve calculation.

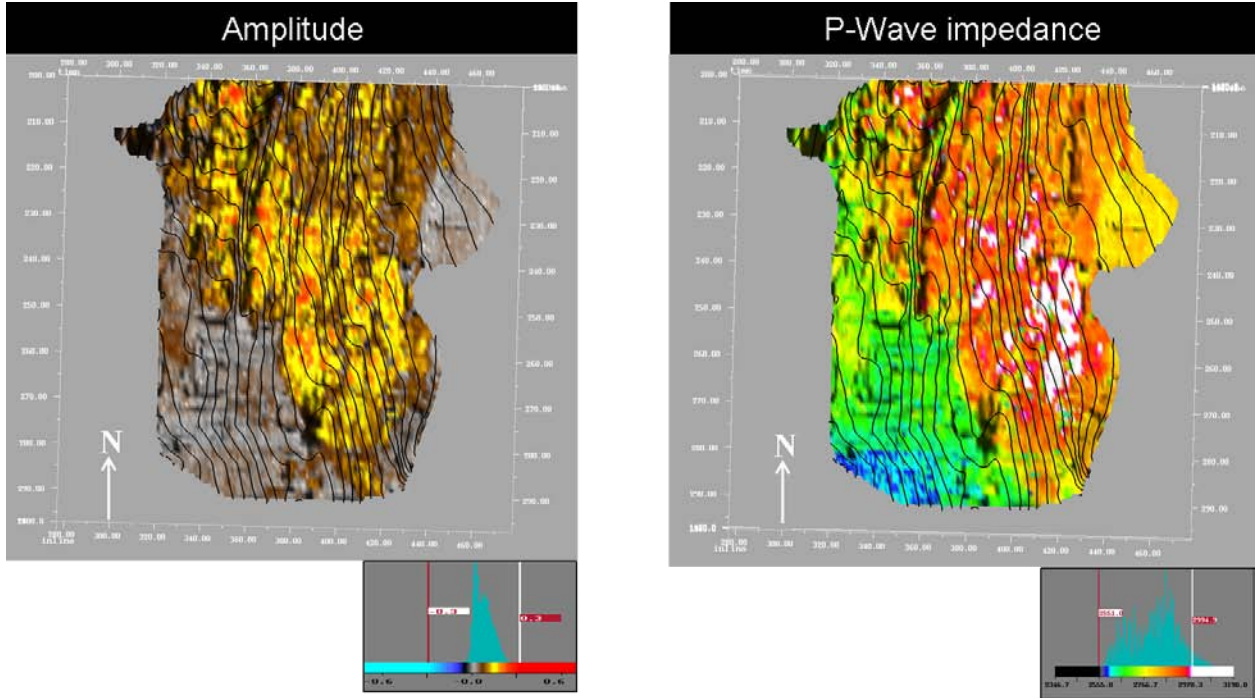


**Figure 38. Amplitude vs. AI extractions.** The attribute extractions are from a surface atop (amplitude) and within (P-impedance) sand “B”. The top of the hydrated sand is characterized by moderate to high peak amplitudes. Higher amplitudes and impedances occur closer to the base of the GHSZ, suggesting that sediments below the GHSZ are sourcing the hydrates.

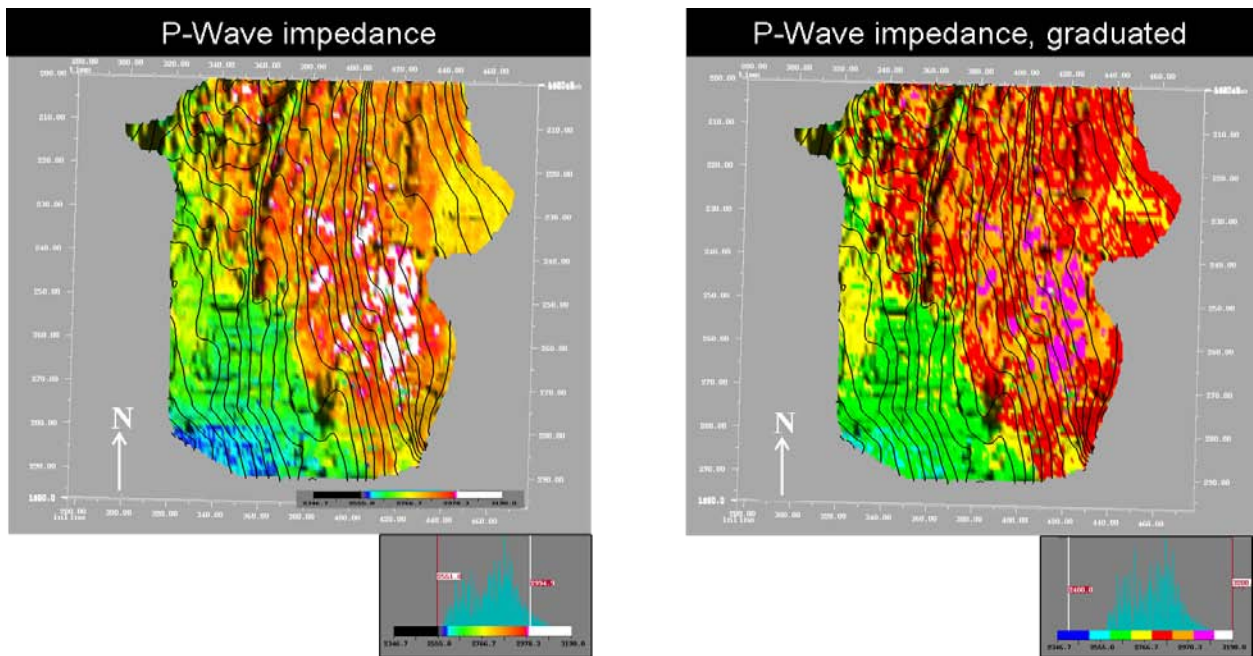


**Figure 39. Acoustic impedance display using linear (left) and graduated (right) colorization.** The graduated color bar emphasizes that no impedance value greater than  $2,800 \text{ kg m}^{-2} \text{ s}^{-1}$  (coinciding with the red to green histogram interval boundary) is observed south of the zero-slip perimeter established by normal faulting.

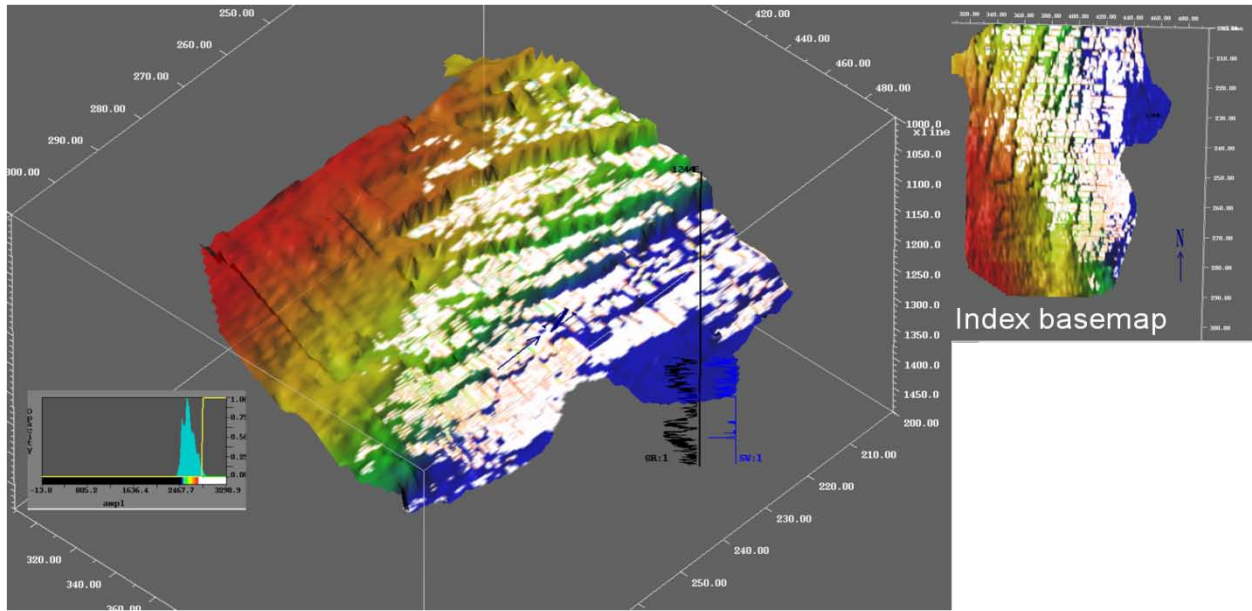


**Figure 40. Volume-rendered, high-impedance geobodies, “B” sand interval. Structure map (with warm colors identifying highs) features the extent of the base of the “B” sand above the BSR (i.e., within the GHSZ). White geobodies sculpted from high-impedances greater than about  $2,800 \text{ kgm}^{-2}\text{s}^{-1}$  coincide with areas of crescent-shaped normal faults. Generally speaking, high impedances within “B” sand cease to occur south of this escarpment region (see index basemap to right). Also, the most intense hydrate occurrence ceases where the normal fault slip goes to zero (high on structure), supporting a genetic linkage between faulting and methane gas hydrate occurrence.**

Interestingly, high hydrate saturations stemming from high impedances encountered at generally intermediate structural elevations support a genetic link between faulting and gas migration (Figures 39, 41), since unfaulted, yet higher structural elevations in the same sand layer do not ever record gas hydrate saturation levels as high. In contrast, high saturation levels are maintained all the way to the down-dip limit of the resource where the top of the hydrated sand projects below the BSR (eastern edge of map; Figures 39, 41). These map patterns support a link between faulted conduits and hydrate saturation, and helps resolve a question posed by earlier workers (Tréhu et al., 2006):

“...we speculate that Horizon B may have acted as an important conduit for free gas migration and may have fed a former seafloor vent system prior to being tectonically disrupted. Alternatively, the vertical faults in this region may facilitate upward fluid flow of fluids supersaturated with methane, which release this methane to form hydrate when they intersect Horizon B because the grain size and pore structure facilitate gas hydrate nucleation.”

Additionally, this map pattern of high gas hydrate saturation levels being spatially confined to the down-dip edge of where the sand meets the BSR may hint at a hydrocarbon charge from a more southeasterly (“landward”) source. It may indicate a past problem of limited migration gas supply or disrupted gas migration across (partially) sealing faults, or both, since the sand did not become fully saturated toward the north of the map and the structurally higher, but more remote western extent of the sand.

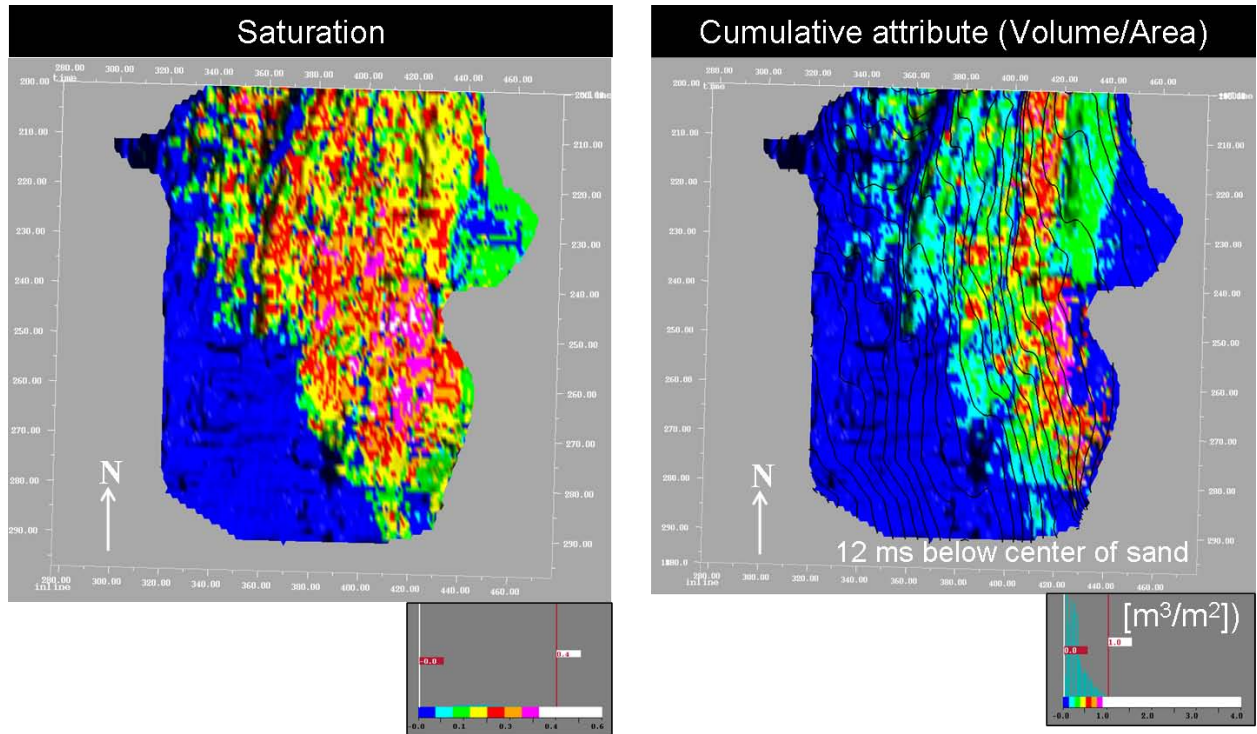


**Figure 41. Saturation and integrated cumulative attribute (cumulative total to base of horizon [12 ms below ZOI] {left image} & interval sum only {right image}).**

Encased by the break-up unconformity below and deposits from syndepositional faulting above the deposition of this sand predates the migration of hydrocarbons along faults and reflects a short-lived phase of turbidite deposition onto an emergent paleo-high undergoing flexure and, eventually, extensional segmentation of a “piggy back” basin by normal faulting (e.g., Chevallier, et al, 2006).

Although this observation supports a close genetic linkage between faulting and hydrocarbon migration, and even though the seismic section overlying this sand is characterized by

expansion across faults (syndepositional faulting), subtle thickness changes observed for this hydrated sand are attributed to stratigraphic pinch-out against a pre-existing high and not syndepositional extension (no major thickness changes for this sand across faults). However, the sand apparently overlies a “break-up” unconformity that heralds a change in tectonic regime. In terms of its timing, this sand is probably best interpreted as a turbidite sheet deposited during the initial phase of renewed and protracted uplift. However, the stratigraphic section immediately overlying this sand exhibits noticeable thickness increases (a minimum of 40% for the section spanning the top of this sand to the low-impedance layer that runs about 40 ms below the water-bottom) suggesting syntectonic deposition (Figure 42).

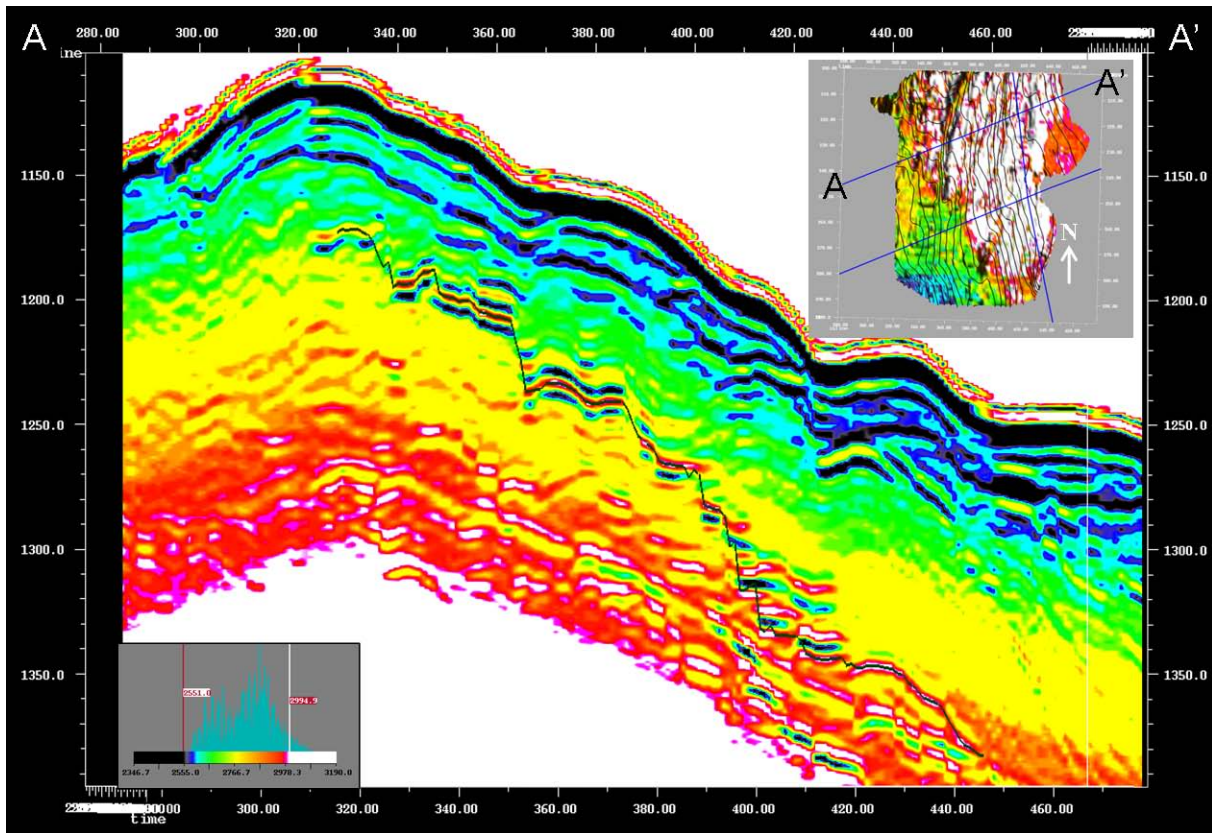


**Figure 42.** Acoustic impedance along arbitrary transect A-A', running approximately perpendicular to structural dip. Hydrated sand resonates at high impedances within the seismic section. Anomalous low impedance zones encasing the sand are an artifact from energy contributions by strong side lobe energy. Up-dip termination of sand is via stratigraphic pinch-out, whilst down-dip termination of the hydrated sand interval is via truncation by the BSR.

## 9. Resource Estimates

### A. Overview

Since only 6 scf of methane gas-water “ice” (“*clathrate*”) convert to 1,000 scf of natural methane gas under atmospheric (surface) conditions, clathrates have tremendous economic significance warranting resource quantification. Prior to resource estimates the seismic attribute data are studied, analyzed, and quality-controlled by comparison to the amplitude data (Figs. 43 – 51). Subsequently, meaningful attribute values are isolated, the edited extraction data are prepared for further statistical reduction, and resource estimates are tabulated (Table 4). In the ensuing discussion (Section 10), an additional table containing geological data and resource estimates from Hydrate Ridge is contrasted to previously presented resource quantifications from Milne Point, Alaska (Table 5).

### B. Quality Control Procedures

First, the integrated cumulative attribute (volume per area; [ $\text{m}^3/\text{m}^2$ ]) is investigated in section view to determine and quality control its behavior (Figures 43-46). It is then extracted onto the BSR map surface (Figure 47). This allows us to screen the overlying seismic section to identify contributions of cumulative hydrate attribute values from all localized levels. Since the CATT method relates amplitude strength to hydrate saturation via elevated impedance levels, geological, and therefore seismic scenarios may arise within the stratigraphic section that give rise to strong amplitude resonance from causes other than actual hydrate saturation (“false positives”). Examples include stark lithology contrast as offered by low-impedance shales overlying basalt or salt, etc. Within the 3-D survey area one such a high-impedance zone void of hydrate saturation is encountered in the vicinity of the 1252A well (Figures 45-47, right side of figures). In this area, the geomodel underlying the inversion incorporated high impedance values stemming from heavy mineral placer minerals dispersed in siltstone deposited as a debris flow. No hydrate saturation was recorded in cores drawn from this particular stratigraphic interval. These ramifications must therefore be viewed as false positives, effectively excluding 2.45 km<sup>2</sup> area from final analysis of resource estimates, an area amounting to about 5% of the

total 3D survey. Our method of removing this false positive from the resource estimates is described below.

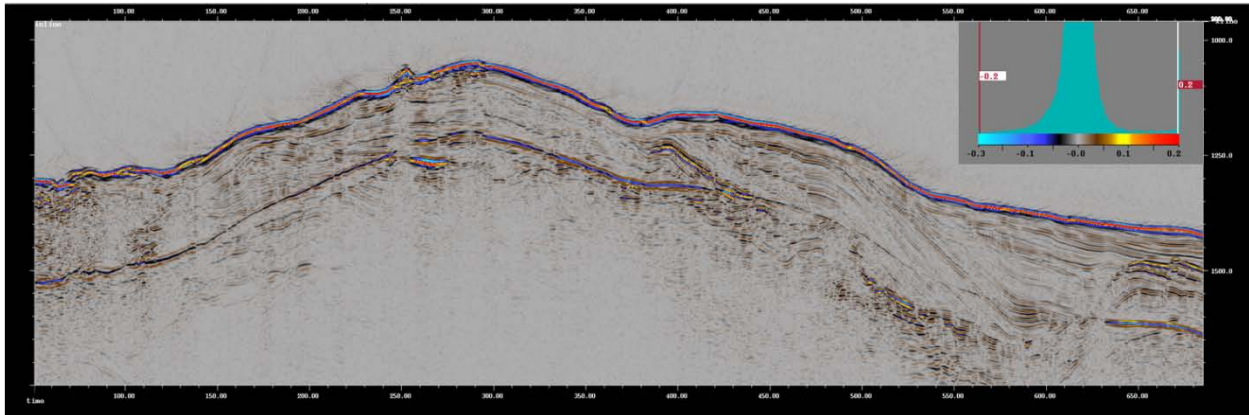


**Figure 43.** Seismic section through an arbitrary traverse trending from SW to NE through survey area. Location of traverse given in Figure 47.

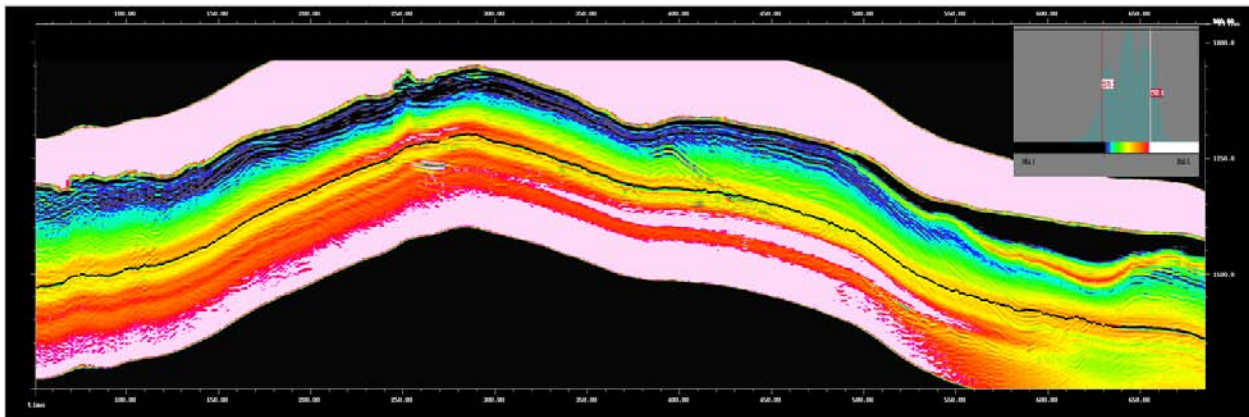


**Figure 44.** P-impedance section through an arbitrary traverse trending from SW to NE through survey area. Location of traverse given in Figure 47. Note that the seismic wedge representing a debris flow (at far right) resonates at higher impedance values than the overlying and underlying seismic section. Although this is geologically reasonable given that well 1252 penetrates this debris flow, the CATT method will predict higher gas hydrate saturations for these zones, even though hydrate saturation itself is absent in cores drawn from this stratigraphic interval and wireline logs from well 1252A. In other words, a false positive will result. The black horizon is the BSR.

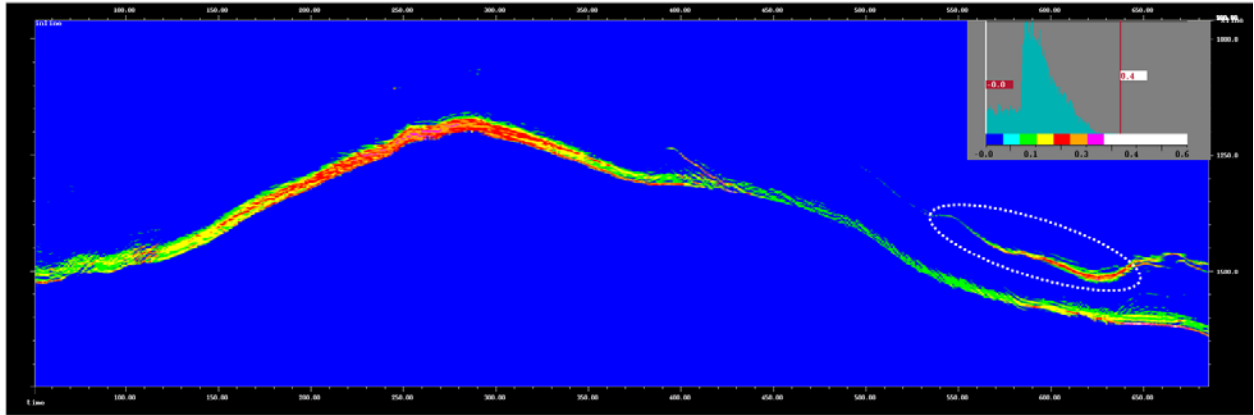


**Figure 45.** Saturation section through an arbitrary traverse trending from SW to NE through survey area. Location of traverse given in Figure 47. False positives from within the debris flow (dotted white ellipse) have been excluded from resource estimates.

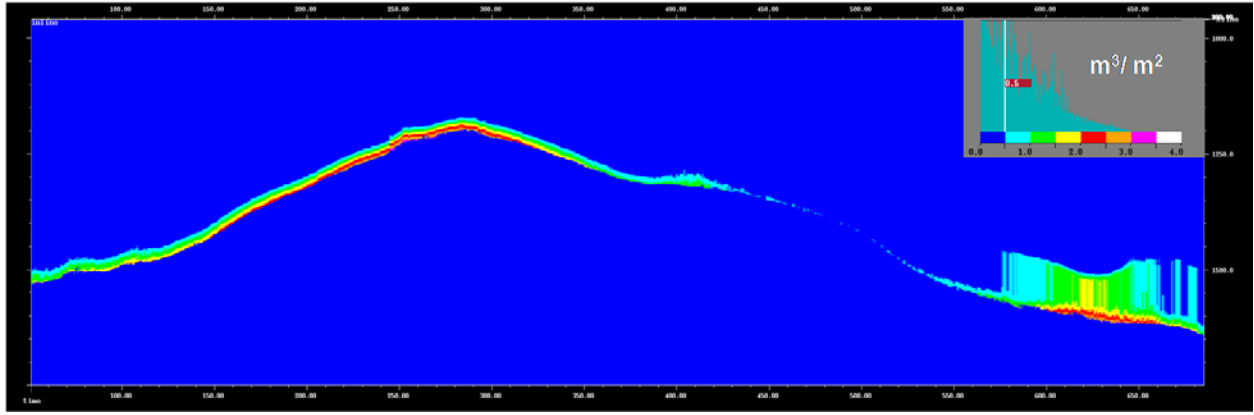


**Figure 46.** Accumulated hydrate section (volume per area [ $m^3/m^2$ ]) through an arbitrary traverse trending from SW to NE through survey area. Location of traverse given in Figure 47. Area beneath false positives coinciding with debris flow deposit has been excluded from resource estimates.

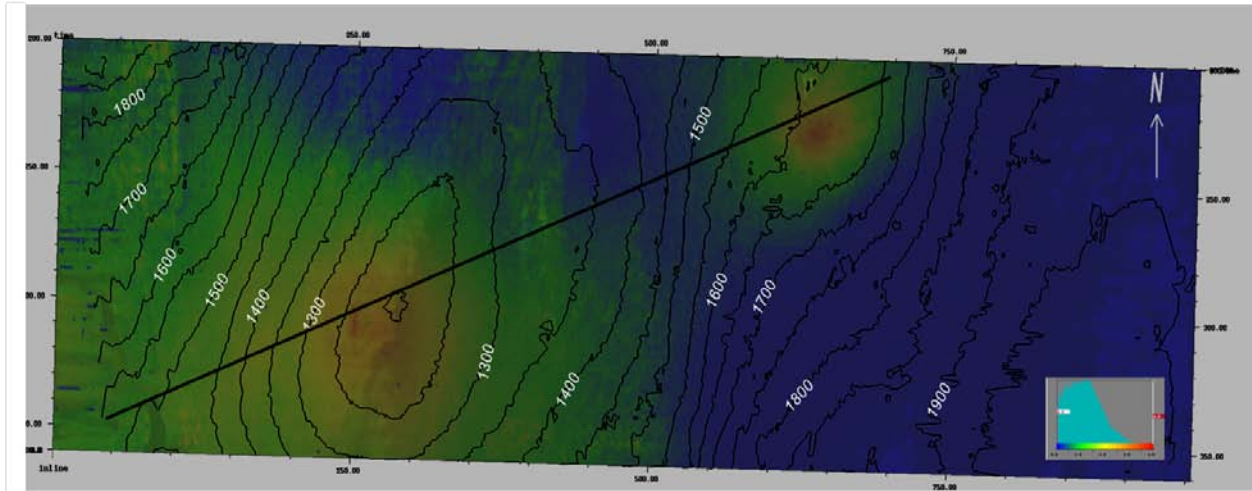


**Figure 47. Map view of accumulated hydrate volume (volume per area [ $m^3/m^2$ ]). Shown map level is set at 6 milliseconds above the BSR horizon. Black trend line is the arbitrary traverse shown in Figures 43 through 46. Approximately 60% of the area contains less than  $0.05 m^3/m^2$  gas hydrate saturation.**

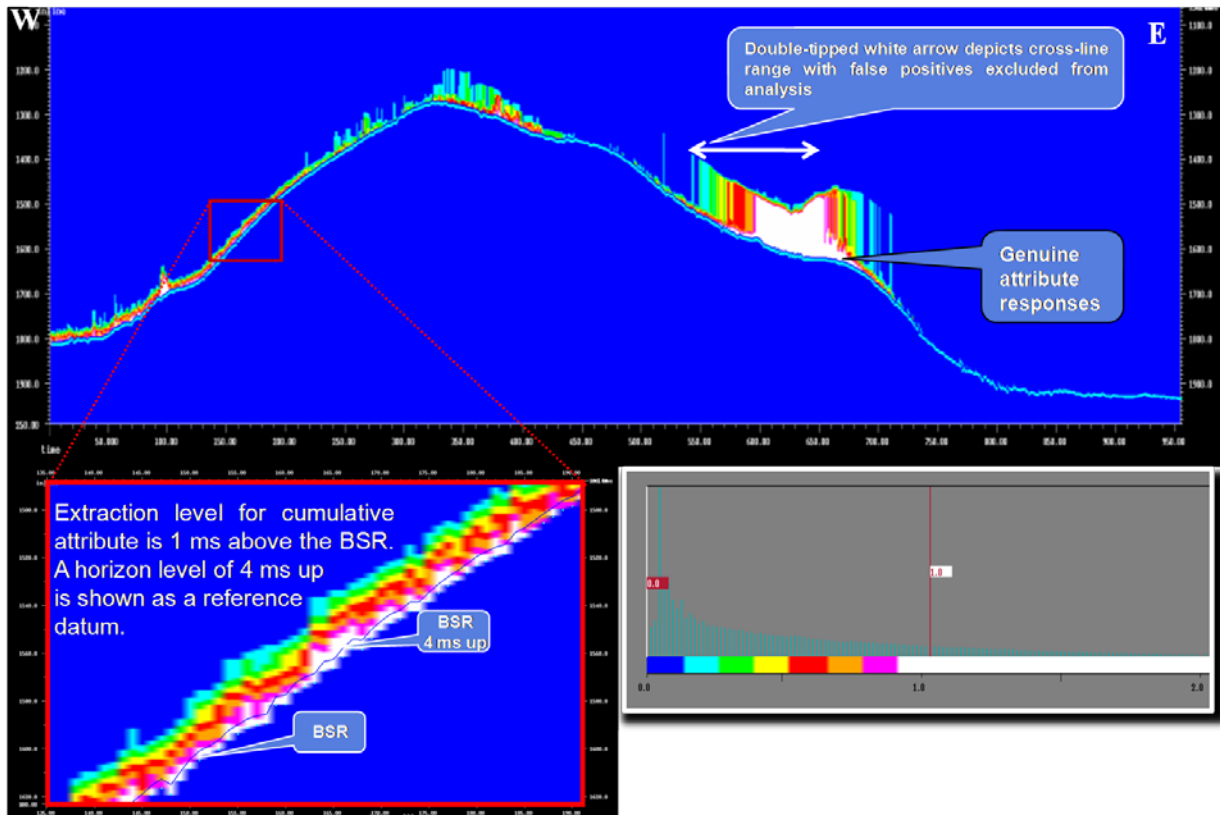


**Figure 48. Cumulative attribute section (volume per area [ $m^3/m^2$ ]) through arbitrary line. Exploded insert depicts detail of horizon extraction. Large anomaly on eastern flank of dome depicts false positives henceforth removed from analysis (cut-out polygonal area delineated by dashed line in Figure 49).**

To exclude false positives from contributing to final gas hydrate resource estimates (Figure 48) a polygon encompassing false positives within the area occupied by the debris flow was excluded from final analysis of resource estimates (~2.45 km<sup>2</sup>, an area amounting to 5% of the total 3-D survey [Figure 49]). Although this cut-out also removes a small amount of genuinely hydrated section below, it does not skew numerical results obtained from statistical analysis.

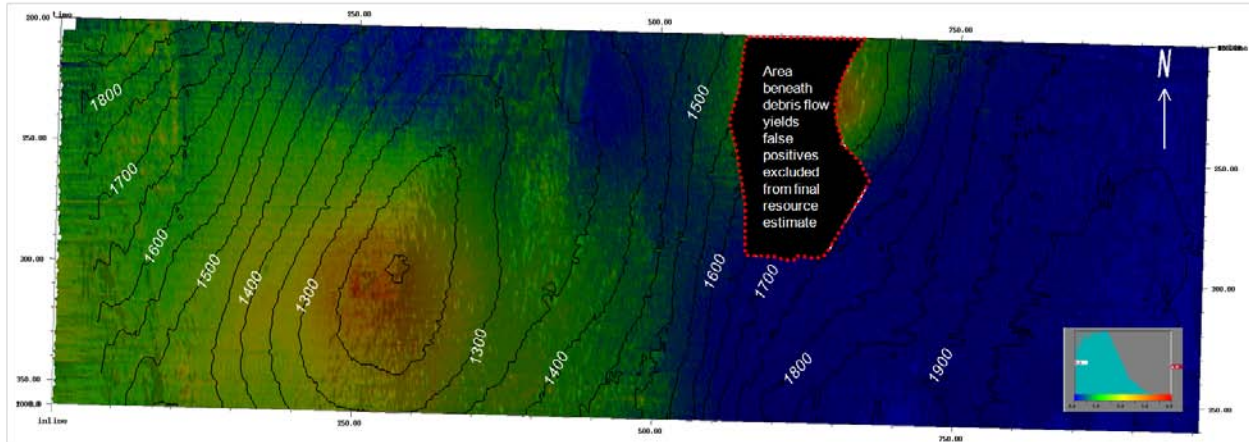


**Figure 49. Edited final integrated cumulative attribute, display level set at 6 ms above BSR. A region totaling less than 5% in area was excluded from final resource estimates.**

A concentric “ring” pattern of graduated hydrate intervals centered at wells 1250 and 1252 (in the summit area) is an imprint from the well kriging component of the low-frequency impedance background model used in the inversion (Figure 49). This observation is supported by the apparent mismatch of hydrate concentrations with respect to the ENE-trending structural grain (represented by contours in Figure 49).

Map views of the cumulative attribute at different stratigraphic levels showed that most of the hydrate saturation within the survey occurs within a narrow vertical window, less than 30 to 50 ms wide, above the BSR. As was pointed out above, this again demonstrates that stratigraphy within the GHSZ is not a primary control on hydrate saturation in this dataset. Instead, it suggests that stratigraphy below the GHSZ is the primary factor controlling hydrate saturation, as has been reported by other researchers (e.g. “Horizon A” of Tréhu et al., 2006).

Compressional velocities generally ramp up within the hydrated section (Figure 50). Hydrate saturation is highest in layers with low- $V_{CLAY}$  (30% to 40%), suggesting that a “modulating effect of lithology on gas hydrate distribution” can be recognized (Tréhu et al., 2006). Nonetheless,

hydrate saturation generally affects the entire section occupied by sands, silts, and shales that lie within a narrow window defined by the BSR to no more than 30 to 50 milliseconds above the BSR.

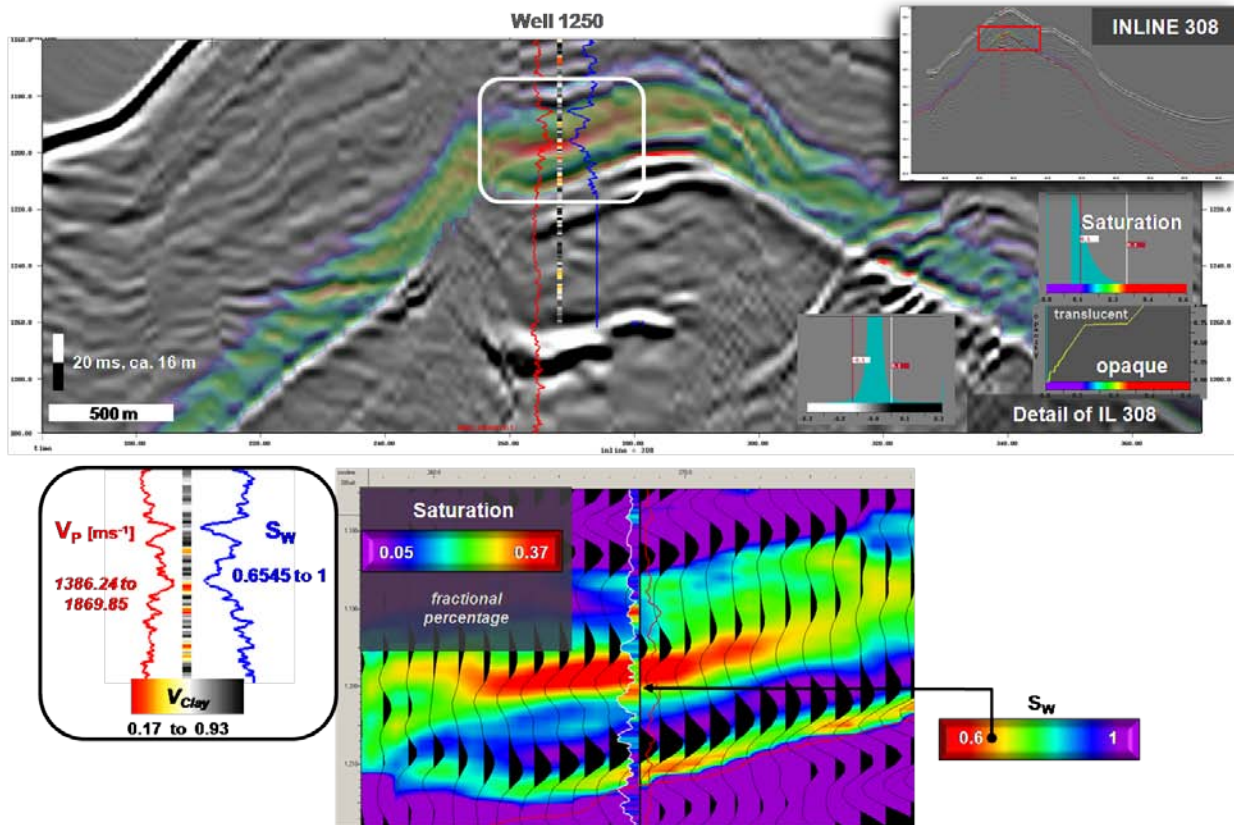


**Figure 50.** Methane gas hydrate saturation at well 1250B (IL 308). Log curves:  $V_p$  (left track, values increasing to right),  $V_{clay}$  ribbon (center track; high  $V_{clay}$  = black; low  $V_{clay}$  = red), and  $S_w$  curve (right track, values increasing to the right). Well tie with  $V_{clay}$  curve color-coded by water saturation shown in lower panel. Only low water saturations ( $S_{gh} > 20\%$ ) trigger a seismic response.

### C. Statistical Analysis of Resource Estimates

Edited attribute extraction data are converted to columnar format and then subjected to numerical analysis using trusted statistical parameters such as mean, sample standard deviation, minimum and maximum values, and count. Average returns the arithmetic mean. Sample standard deviation precludes underestimation of variance by using factor  $(n-1)$  instead of  $(n)$  used in calculation of the standard deviation population. For this analysis, we have

excluded all false positives from contributing to final hydrate resource estimates and statistics. The results are shown in Table 4.

<i>Total number of samples (traces)</i>	98,079
<i>Minimum attribute value</i>	0.03 m <sup>3</sup> /m <sup>2</sup>
<i>Maximum attribute value</i>	3.99 m <sup>3</sup> /m <sup>2</sup>
<b>Average</b>	<b>1.26 m<sup>3</sup>/m<sup>2</sup></b>
<i>Standard deviation</i>	0.72 m <sup>3</sup> /m <sup>2</sup>
TOTAL Gas Hydrate Volume within 3D SURVEY AREA	123,291 m <sup>3</sup>
Conversion from m <sup>3</sup> to scf (x 35.31)	4,353,405.21 scf
HYDRATE TO GAS EXPANSION FACTOR 166.7	7.26 x 10 <sup>8</sup> scf
<b>MINIMUM* TOTAL GAS</b>	<b>~ 730 BCF</b>

**Table 5. Final and corrected gas hydrate resource estimates (Reduced areal extent = 44.95 km<sup>2</sup>).**

## 10. Discussion

The Hydrate Ridge offshore 3-D survey falls within the geological setting of an accretionary prism draped by a deformed forearc basin (Chevallier et al., 2006). Sedimentary deposits are mostly of Pleistocene age with a secondary, thin Holocene cover (Chevallier et al., 2006). The base of the hydrated section is seismically demarcated by the BSR. BSR strength provides a reasonable proxy for the degree to which the overlying section has been hydrated. However, locally, BSR reflectivity may be skewed by constructive interference patterns (Figure 42) or be negatively impacted from mass wasting or highly localized temperature increases leading to total obliteration of BSR (Figure 30). In addition to the present-day BSR, seismic data contains

a paleo-BSR (Figures 32-24) suggesting either relative sea-fall or uplift after the earlier BSR had equilibrated or, alternatively, presence of a Structure II hydrate causing a second BSR reflection, as suggested by Claypool et al., 2006. The interpretation of the BSR as a relic structure implies that, in spite of the presence of the modern day sea-level high stand (Holocene), the BSR climbed upward because of regional uplift (decreasing water depth), the net vector of which must have therefore outpaced the global sea-level rise since the last ice age.

Well logs penetrating the hydrated section encounter dominantly shale with some silt and no major sands. In the seismic data, however, several hydrated sands can be discerned above the BSR, but these are volumetrically of only minor importance, since most of the hydrate saturation occurs within a small window, generally less than 30 ms wide (~26 m) above the BSR. Within this window hydrate saturation decreases from bottom toward the top.

Map and perspective views of the B Sand draping the eastern flank of the dome demonstrate that maximum hydrate occurrence occurs low on structure, at the base of a region characterized by en échelon normal fault escarpments (Figs 38-42, fig. 52). This observation supports a genetic link between faulting and hydrate accumulation as postulated by Tréhu et al., 2006. Since high gas saturations are not encountered toward the structural high of the sand, this deficit may indicate a past supply problem (“trickle-up” and self-sealing of this region), partially sealing faults, or a combination of both alternatives.

The window above the BSR looks similar in that gas “trickling” into the section capable of retaining hydrate soon decreased matrix permeability. This caused the BSR to increasingly act as a seal to future gas migration (as is seismically evidenced by multiple gas sands trapping against the BSR from below, Figures 33, 37). Thus, the formation of hydrates immediately counteracts the continued “trickle-in” of free gas from below. This is in stark contrast to Milne Point Alaska, where a seal provided by the top of the hydrated section was an Eocene unconformity and doubled as the permafrost base (Table 5). Hydrate occurrence there was confined to dominantly fluvial and delta sands whilst hydrates at Hydrate Ridge appear to inhabit any lithology as long as it is high on structure, although there is a clear preference toward silty or sand-dominated intervals (Table 5).

Statistical reduction of cumulative attribute values over an area approximating 45 km<sup>2</sup> produced the following results: the maximum hydrate concentration is less than 4 m<sup>3</sup>/m<sup>2</sup> (for comparison, results from Milne Point show that the maximum hydrate concentration is nearly 60% higher). At Milne Point this is because of the high concentrations of gas hydrates that accumulated within a classic trap configuration. This was provided by fault-bound Paleocene river sands that subsequently became subjected to an altered PT-regime, allowing hydrates to form. In contrast, the formation of a BSR at Hydrate Ridge tends to gradually counteracts continued additions of free gas to the rock column overlying the BSR because the entire hydrated section effectively develops sealing capacity. However, total calculated gas hydrate resources here compare favorably to those calculated for Milne Point, since the Milne Point accumulations are located within areally restricted sand-rich paleo-depositional environments, whereas hydrates at Hydrate Ridge generally are less dependent on lithology and are localized by broad local or global structural closures created during deformation of the accretionary prism. Nevertheless, within the GHSZ finer-grained sediments generally exhibit lower hydrate saturation levels than siltier sediment. For the hydrate-bearing area of the survey, an average of 1.26 m<sup>3</sup>/m<sup>2</sup> calculates to over 720 Bcf in total resources.

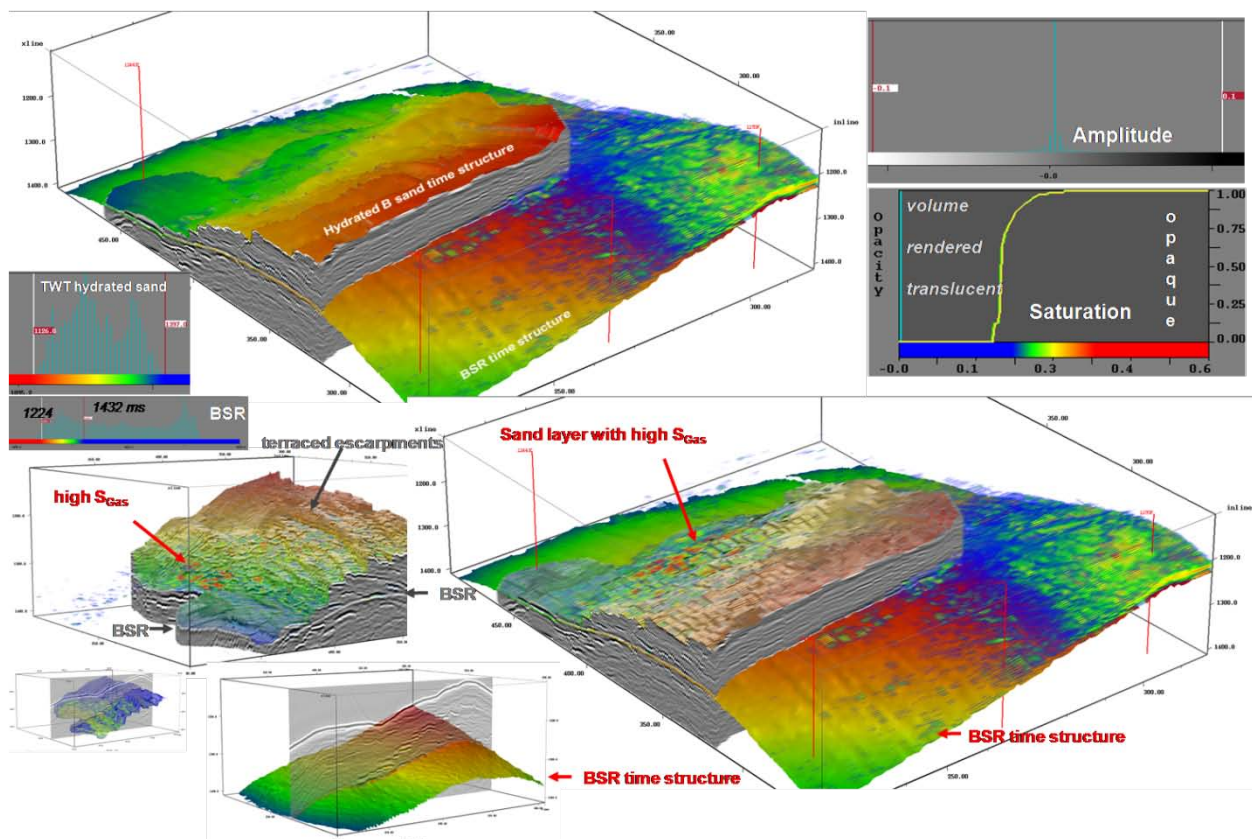


**Figure 52. Perspective views of saturation volume co-rendered with amplitude. Displays shows that, generally speaking, high gas hydrate saturations occur high on structure, but in the case of hydrated sand draping the eastern flank of the dome, high saturations are encountered at low structural elevations, at the foot of a region segmented by an echelon terraced normal fault escarpments.**

Item	Hydrate Ridge, OR	Milne Point, AK
3-D setting	offshore	Merged onshore/offshore
Geological setting	forearc basin accretionary wedge	Brooks Range foreland basin
Reservoir age	Pleistocene - Holocene	Paleocene
Reservoir lithology	All lithologies, although gas hydrate saturations are higher in lower $V_{CLAY}$ sediments	Fluvial channel & levee sands
Migration	Gas moves into structural flexures within a "live" PT-window capable of hydrate formation; trickle-in self-sealing occurs; hydrate formation occurs early	Classic migration into pre-existing traps provided mostly by Paleocene river deposits; hydrate formation occurs afterward
Trap	Time-transgressive, self-sealing, i.e., hydrate formation process itself decreases permeability; system "locks" when permeability goes to zero	Classic seal provided by Eocene unconformity that doubles as the base of the permafrost
Vertical resource distribution	hydrate saturation decreases away from the seal; i.e., upward in the section away from BSR; hydrated zone generally < 30 m thick	Hydrates increase toward the top seal, i.e. saturations increase upward toward the Eocene seal
Survey Area	44.95 km <sup>2</sup> (17.36 mi <sup>2</sup> )	33.375 km <sup>2</sup> (12.5 mi <sup>2</sup> )
Area ratio	1.35	1
Maximum cumulative hydrate accumulation	3.99 m <sup>3</sup> /m <sup>2</sup>	6.34 m <sup>3</sup> /m <sup>2</sup>
Average cumulative hydrate accumulation	1.26 m <sup>3</sup> /m <sup>2</sup>	1.51 m <sup>3</sup> /m <sup>2</sup>
Total reserves	726 Bcf	398 Bcf
Total reserve ratio	1.82	1

**Table 6. Qualitative & quantitative comparison of study results.**

## 11. Conclusions

Geophysical Well Log Analysis was performed in 6 wells drilled through the gas hydrate stability zone in Hydrate Ridge, offshore Oregon. The process included editing logs from shallow-looking tools, derivation of lithology, porosity calculation, fluid saturation calculation, generation of acoustic impedance logs, and Poisson's ratio logs. In order to calculate robust elastic logs (RHOB, P-, and S-wave velocities) forward modeling based on the "soft-sand" theoretical model of Dvorkin et al (1999, 2003) was applied to predict elastic properties of sediments with or without gas hydrates.

Rock physics analysis and modeling showed that P-wave impedance may provide discrimination between gas hydrate-bearing intervals in Hydrate Ridge and the surrounding sediments provided the gas hydrate saturation is higher than 20%.

Well-to-seismic ties had cross-correlations between 0.5-0.7 after rock physics modeling of the logs and conditioning of the seismic data. Well ties were reasonable but some events did not correlate, possibly due to rock property changes not accounted for in the rock physics models, borehole problems, or seismic imaging errors. Wavelet analysis showed that the seismic was close to zero phase after applying a rotation of 180 degrees during the data conditioning phase. The low frequency model used in the inversion consisted of extrapolated well logs only. It did not include seismic velocity control because none was available for our use. This is the primary limiting factor in the accuracy of our results.

In general, the inversion showed a good match with upscaled impedance logs and had low residuals, indicating that the inversion was of high reliability.

Rock physics transforms between P-wave impedance and gas hydrate saturation were developed for two seismic cumulative attributes (CATTs) using well data: saturation and cumulative volume. These transforms are case-specific and are valid only for Hydrate Ridge wells. We then calculated these two attributes on the inverted volume. The method successfully detected the primary hydrate intervals but missed smaller intervals that lack a seismic signature. Overall this method shows promise for quantifying gas hydrate volume in Hydrate Ridge provided the hydrates have a seismic signature and exist in sufficient saturation (>20%).

Analysis of the resulting hydrate saturation and cumulative hydrate volumes show that when present, hydrate accumulation is limited to a narrow window, 30 to 50 ms wide (~26 to 43 m) immediately above the BSR. Seismic and well log data support the hypothesis that hydrate accumulation in these unconsolidated sediments reduces permeability, ultimately causing self-sealing of the GHSZ, as evidenced by “free” gas trapped against BSR from below and reduced hydrate saturation upward in the GHSZ. Hydrate accumulation in the GHSZ is generally independent of lithology, although higher compressional velocities in low  $V_{CLAY}$  layers suggest that siltier layers become preferentially hydrated. Finally, concentric map patterns of increasing hydrate accumulation centered at wells 1250 and 1252 represent geophysical artifacts carried over from use of an overly simplistic low-frequency background model using only acoustic impedance well logs. In the absence of a velocity field, well kriging alone cannot possibly provide an adequate nor stable low-frequency model. For this reason, obtained resource estimates exceeding 720 Bcf for a 45 km<sup>2</sup> wide area must be viewed with caution.

## 12. References

- American Geological Institute, Glossary of Geology, 2005, 5<sup>th</sup> edition, 600 pp.
- Archie, G.E., 1942. The electrical resistivity log as an aid in determining some reservoir characteristics. *Trans. Am. Inst. Mech. Eng.*, vol. 146, pp. 54-62.
- Bangs, N.L.B., Musgrave, R.J., and Tréhu, A.M., 2005. Upward shifts in the southern Hydrate Ridge gas hydrate zone following postglacial warming, offshore Oregon. *J. Geophys. Res.*, 110(B3):B03102.
- Chevallier, J., Tréhu, A.M., Bangs, N.L., Johnson, J.E., and Meyer, H.J., 2006, Seismic Sequence Stratigraphy and Tectonic Evolution of Southern Hydrate Ridge. *In* Tréhu, A.M., Bohrmann, G., Rack, F. R., Torres, M.E., et al., 2003, Proceedings of the Ocean Drilling Program, Scientific Results, Volume 204: College Station, TX. [http://www-odp.tamu.edu/publications/204\\_SR/121/121.htm](http://www-odp.tamu.edu/publications/204_SR/121/121.htm).
- Claypool, G. E., Milkov, A. V., Lee, Y.-J., Torres, M. E., Borowski, W. S., and Tomaru, H., 2006, Microbial Methane Generation and Gas Transport in Shallow Sediments of an Accretionary Complex, Southern Hydrate Ridge (ODP Leg 204), Offshore Oregon, USA
- Collett, T.S., Lewis, R., Uchida, T., 2000, Growing Interest in Gas Hydrates, *Oilfield Review*, p. 42-57
- Dvorkin, J., Nur, A., Uden, R., and Taner, T., 2003, Rock physics of Gas Hydrate Reservoir, *The Leading Edge*, 22, 842-847.
- Dvorkin, J., Prasad, M., Sakai, A., and Lavoie, D., 1999, Elasticity of Marine Sediments, *GRL*, 26, 1781-1784.
- Guerin, G., Goldberg, D.S., and Collett, T.S., 2006, Sonic Velocities in an Active Gas Hydrate System, Hydrate Ridge. *In* Tréhu, A.M., Bohrmann, G., Rack, F. R., Torres, M.E., et al., 2003, Proceedings of the Ocean Drilling Program, Scientific Results, Volume 204: College Station, TX. [http://www-odp.tamu.edu/publications/204\\_SR/124/124.htm](http://www-odp.tamu.edu/publications/204_SR/124/124.htm).
- Helgerud, M., 2001, Wave Speeds in Gas Hydrate and Sediments Containing Gas Hydrate: A Laboratory and Modeling Study, Ph.D. thesis, Stanford University.

- Kumar, D, Sen K. and Bangs, L, 2006, Seismic Characteristics of gas hydrates at Hydrates Ridge, offshore Oregon, The Leading Edge, p610-614
- Lee, M. and Collet, T., 2006, Gas Hydrate and Free Gas Saturations Estimated from Velocity Logs on Hydrate Ridge, Offshore Oregon, USA. *In* Tréhu, A.M., Bohrmann, G., Rack, F. R., Torres, M.E., et al., 2003, Proceedings of the Ocean Drilling Program, Scientific Results, Volume 204: College Station, TX. [http://www-odp.tamu.edu/publications/204\\_SR/103/103.htm](http://www-odp.tamu.edu/publications/204_SR/103/103.htm).
- Mavko, G., Mukerji, T., and Dvorkin, J., 2009, The Rock Physics Handbook: Tools for Seismic Analysis in Porous Media: Cambridge Univ. Press.
- Sava, D. and Hardage, B., 2006. Rock Physics Characterization of Hydrate-Bearing Deepwater Sediments: The Leading Edge, 616 – 619.
- Taylor, M.H, Dillon W.P, Pecher, I.A., Trapping and Migration of methane associated with the gas hydrate stability zone at the Blake Ridge Diapir: new insights from seismic data, Marine Geology 164(2000), p79-89
- Tonellot, T., Mace, D., and Richard, V., 2001, Joint Stratigraphic Inversion of Angle-Limited Stacks, SEG Expanded Abstracts.
- Tonellot, T., Mace, D., and Richard, V., 2002, 3D Quantitative AVA: Joint Versus Sequential Stratigraphic Inversion of Angle-Limited Stacks, SEG Expanded Abstracts.
- Torres, M. E., Trehu, A. M., Wallmann, K., Bohrmann, G., Schultheis, P., Borowski, W., Tomaru, H., 2004, Evidence for Free Gas within the GHSZ on Hydrate Ridge, Oregon, and Implications for Rate of Gas Hydrate Formation, The American Association of Petroleum Geologists, Abstracts with Program
- Tréhu, A.M., Bohrmann, G., Rack, F. R., Torres, M.E., et al., 2003, Proceedings of the Ocean Drilling Program, Initial Reports, Volume 204: College Station, TX. [http://www-odp.tamu.edu/publications/204\\_IR/204TOC.HTM](http://www-odp.tamu.edu/publications/204_IR/204TOC.HTM).
- USGS Woods Hole Science Center; 2009, Gas hydrate what is it?  
<http://woodshole.er.usgs.gov/project-pages/hydrates/what.html>

Xiaoli Liu, Fleming, P, Passing gas through the hydrate stability zone at southern Hydrate Ridge, offshore Oregon, Earth and Planetary Science Letters 241, 2006 p211-226.

### 13. Cost Plan Status Report

Year 2 Start: May 12, 2008 thru May 11, 2009  
 extended to October 31,  
 2009

Baseline Reporting Quarter	Q1	Q2	Q3	Q4	Additional Q1	Additional Q2
<b>Baseline Cost Plan (from SF-424A)</b>						
Federal Share	71,969	81,342	75,732	69,992	-	-
Non-Federal Share	30,844	34,861	32,457	29,996	-	-
<b>Total Planned (Federal and non-Federal)</b>	102,813	116,202	108,189	99,988	-	-
<b>Cumulative Baseline Cost</b>	102,813	219,015	327,204	427,192	427,192	427,192
<b><u>Actual Incurred Costs</u></b>						
Federal Share	-	27,296	31,592	113,037	89,858	52,278
Non-Federal Share	-	11,698	13,540	48,444	38,511	22,405
<b>Total Incurred Costs - Quarterly (Federal and non-Federal)</b>	-	38,994	45,132	161,481	128,369	74,682
<b>Cumulative Incurred Costs</b>	-	38,994	84,126	245,607	373,976	448,659
<b><u>Variance</u></b>						
Federal Share	-	-				
Non-Federal Share	-	-				
<b>Total Variance-Quarterly (Federal and non-Federal)</b>	102,813	77,208	63,057	(61,493)	(128,369)	(74,682)
<b>Cumulative Variance</b>	102,813	25,605	88,663	27,170	(101,200)	(175,882)

## **National Energy Technology Laboratory**

626 Cochrans Mill Road  
P.O. Box 10940  
Pittsburgh, PA 15236-0940

3610 Collins Ferry Road  
P.O. Box 880  
Morgantown, WV 26507-0880

One West Third Street, Suite 1400  
Tulsa, OK 74103-3519

1450 Queen Avenue SW  
Albany, OR 97321-2198

539 Duckering Bldg./UAF Campus  
P.O. Box 750172  
Fairbanks, AK 99775-0172

Visit the NETL website at:  
[www.netl.doe.gov](http://www.netl.doe.gov)

Customer Service:  
1-800-553-7681

